Crystalline Assembly of Gold Nanoclusters Mediated by Complexation Reaction

A thesis submitted by

Srestha Basu

Roll No. 146122030

to

Indian Institute of Technology Guwahati

for the award of the degree of

Doctor of Philosophy

Department of Chemistry

Indian Institute of Technology Guwahati

Guwahati – 781039 India

July 2018

Statement

This thesis entitled “Crystalline Assembly of Gold Nanoclusters Mediated by Complexation Reactions” is a work of research and investigation carried out by me under the supervision of Dr. Anumita Paul, Professor, Department of Chemistry, Indian Institute of Technology Guwahati. This thesis has been submitted by me to the Department of Chemistry, Indian Institute of Technology Guwahati for the award of the degree of Doctor of Philosophy. I further declare that this work has not been submitted anywhere else for any degree, diploma, associateship or membership etc. of any Institute or University to the best of my knowledge.

Srestha Basu
Department of Chemistry,
IIT Guwahati,
Guwahati-781039, Assam, India
Date:
Place: Guwahati, Assam

Certificate

It is certified that the thesis entitled "Crystalline Assembly of Gold Nanoclusters Mediated by Complexation Reactions" being submitted to the Indian Institute of Technology Guwahati by Srestha Basu (Roll. No. 14612225) for the award of the degree of Doctor of Philosophy in Chemistry, is a bonafide record of research work carried out by her. The information and data reported by her are solely the results of her original findings. She has meticulously carried out the investigations and followed the guidelines of the laboratory. This work has not been submitted elsewhere for any degree or diploma.

Anumita Paul
Thesis Supervisor
Professor,
Department of Chemistry,
IIT Guwahati,
Guwahati-781039, Assam, India.
Date:
Place: Guwahati, Assam

Dedicated to

Mammam, Babin and Dibhai

Acknowledgements

It was my first day of MSc course at IIT Guwahati. Quantum chemistry has always fascinated me. So I was eager to attend the course. However, deep inside my heart, I had a grief embedded – the grief of leaving home, the grief of leaving my loved ones behind for the first time in life. That day I had no one to wake me up in the morning for "college". No one asked me when I would come back from class, no one served me breakfast. I did it all alone – for the first time. I felt lonely, uncared and not pampered to the usual extent. It was then, a beautiful lady wrapped in a black salwar entered the class. She inaugurated the course with "black body radiation". My friend sitting next to me asked "Her dress is matching with the topic". I couldn't pay much attention to my friend because her first glimpse seemed to wipe away from my buried heart, my aforementioned grieves. Suddenly I felt motivated and all geared up for my new journey at IIT Guwahati. I realized my new life has the best of things in store for me. Yes! She was my "then" course instructor and "now" supervisor – Anumita Ma'am. Though in pen and paper she is my supervisor, she has played the role of my mother and my best of friend more than a supervisor. I used to deliberately miss my attendance in her classes, just to ensure that she remembers my name. I used to stay up late night to finish her tutorials, just to ensure she recognizes me as the best. Later on, the day I was about to leave this place following completion of MSc, I realized that all these efforts were redundant as she had already allotted me a place in her divine heart. I couldn't join anywhere else for PhD. The warmth of her unconditional love and her tenderness, held me back. I consider this decision to be the best decision of my life. She has been, is and will continue to be the best thing in my life. I would not dare to thank her for her contributions in my life as for me she is beyond the realm of gratitude.

I would like to express my sincere gratitude to Prof. Arun Chattopadhyay for giving me more than what I deserve. He has been extremely tolerant towards my idiosyncrasies and mood swings. He calls me ***"Eklavya"***. However Sir (Prof. Chattopadhyay) has never asked anything from me as "gurudakshina". Instead he has tried his best to give me the best of opportunities to pursue research and lead a quality life dedicated to the well-being of society. However, in my opinion, the best thing he could give me is the title of ***"Eklavya".***

I am indebted to the central instruments facility (CIF), IIT Guwahati for providing me with infrastructural facilitates.

Words are not enough to convey my heartfelt gratitude to Dr. Rana Sen, Dr. Dinabandhu Kundu and Dr. Debjani Ghosh for their relentless encouragement and immense contribution in shaping my life.

Lastly, I am thankful to god (if there exists one) for blessing me with a wonderful family who has been a support system in my life.

Srestha

Table of contents

Chapter 1

Introduction

A persistent premise of concern with regard to synthesis of nanoparticles, is their polydispersity. However, the issue of polydispersity associated with synthesis of nanoparticles has been addressed to a large extent following introduction of newer synthetic strategies or improvisations based on existing synthetic methods. Notwithstanding the efforts employed in this regard, synthesizing atomically precise surface plasmon resonance (SPR) active nanoparticles, remains a challenge. This has propelled the urge for synthesis of atomically precise nanoscale particles akin to molecules, any two of such nanoscale particles are alike in terms of molecular formula.[1] This has led to the advent of atomic nanoclusters with sizes in the range of Fermi wavelength of electron, well-defined structures (guided by number of constituent atoms), size dependent optical and redox properties and intrinsic luminescence characteristics owing to discretization of energy levels (unlike their nanoparticle analogues where the electronic structures are semicontinuous in nature).[2-6] As a consequence of these unique properties, nanoclusters have been used for a myriad of applications like fabrication of electronic devices, as bio imaging agents, efficient catalysts in organic transformations, photosensitizers and nanomedicines.[7- 15]

1.1 Nanoclusters

1.1.1 The definition

Nanoclusters are collections of a few atoms and their sizes are typically in the range of Fermi wavelength of electron i.e., < 2 nm. These imbues the nanoclusters with molecule like features and thereby distinguishes them from their nanoparticle analogues whose characteristics are primarily “metal-like”.

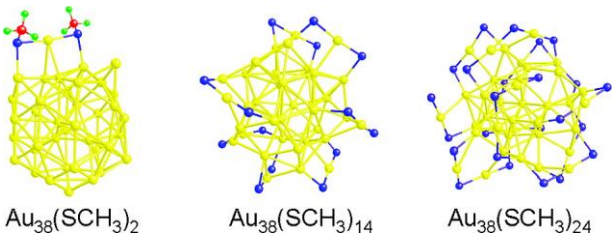

Fig.1.1 Theoretically optimized structures of thiolated Au NCs comprising of 38 Au atoms. Reprinted with permission from *J. Am. Chem. Soc*., 2008, **130**, 2777–2779.

1.1.2 Origin of luminescence in nanoclusters

Luminescence in nanoclusters is a consequence of their electronic structure. For example, if the numeric spacing of energy (HOMO- LUMO gap) levels in a nanoscale particle is considerably higher than the thermal energy (K_BT), the structure of the nanoscale particle is electronically stabilized and thermal energy is inadequate to excite the electrons to higher energy states. Under this condition, nanoscale particles exhibit molecule like characteristics and are highly luminescent. On the other hand, if the gap between the energy levels are smaller than the thermal energy, the electronic states are defined by thermal occupation of states. The relaxation involves inelastic electron scattering, as a consequence of which the radiation becomes weak and instead of luminescence, surface plasmon absorption dominates and nanoparticle like behavior is observed. The numerical relationship connecting the separation of energy levels (E), number of atoms constituting the clusters and Fermi energy (E_f) is given by:

$$E = E_f / N^{1/3} \quad (1)$$

As apparent from equation (1), the luminescence of NCs being solely governed by electronic transitions, the wavelength of emission is expected to be higher for NCs comprised of greater number of atoms and vice versa.[16] However, it has been reported that other factors like ligands stabilizing the NCs, owing to ligand to metal charge transfer, also affects the emission properties of NCs.[17]

1.1.3 Applications of nanoclusters

1.1.3.1 Sensing and bioimaging

The luminescence of noble metal nanoclusters has been extensively used for sensing of analytes including heavy metal ions, inorganic anions, proteins, biomolecules and disease markers [18-22] An inherent virtuosity of noble metal nanoclusters that has enabled their extensive application as biosensors and biomarkers, is their non-toxic (especially gold) nature. Noble metal nanoclusters (especially gold nanoclusters), unlike quantum dots, are generally known to be non-cytotoxic. Hence metal nanoclusters have been widely used for detection of analytes in living cells. For example, it has been recently demonstrated that mercaptundecanoic acid (MUA) stabilized Au NCs could detect phospholipase C in breast cancer cells.[23] Further, targeted imaging of cancer cells by using NCs conjugated with receptor molecules has emerged as an important method in biodiagnostics. For example, Au NCs stabilized with insulin have been used for targeting of cells overexpressed with insulin receptors.[24] In allied vein, transferrin stabilized Au NCs have been used for targeting of cells over expressed with transferrin receptors.[25]

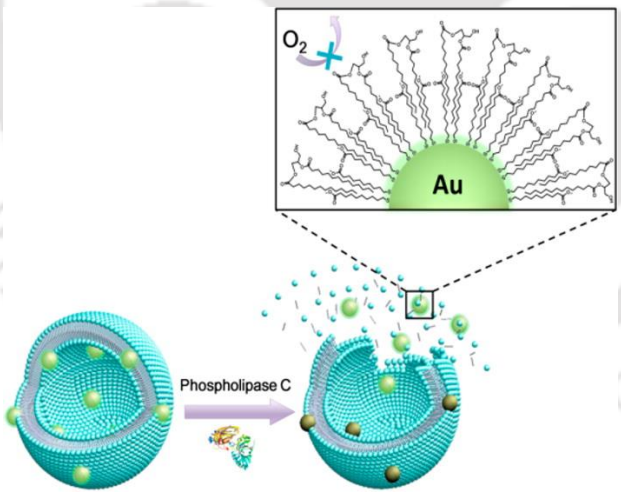

Fig. 1.2 Schematic illustration of detection of phospholipase in breast cancer cells using luminescent Au NCs. (Reprinted with permission from reference 23. Copyright Anal. Chem. 2013, American Chemical Society).

1.1.3.2 Catalysis

Atomically precise ultra-small NCs having well defined structures provide a unique opportunity to correlate the catalytic properties of the NCs with their atomic structure.[26] Thus recent surge of research reports the emergence of metal nanoclusters as an interesting class of catalysts in organic transformations. For example, thiol protected Au_{25} NCs have been used for oxidation of styrene to benzaldehyde in presence of oxygen.[27] Another important class of organic transformation is conversion of sulfides to sulfoxides as the latter is an important intermediate for synthesis of medicinal products. In this regard, Au_{25} NCs have been reported to oxidize sulfides to sulfoxides in presence of iodosylbenzene as an oxidant.[28] In addition to the aforementioned transformations, Au NCs have been used as catalysts in hydrogenation of aldehydes and ketones, hydrogenation of nitrophenols, hydrogenation of nitrobenzaldehyde derivatives, carbon-carbon bond coupling reactions and homocoupling reactions.[29-32]

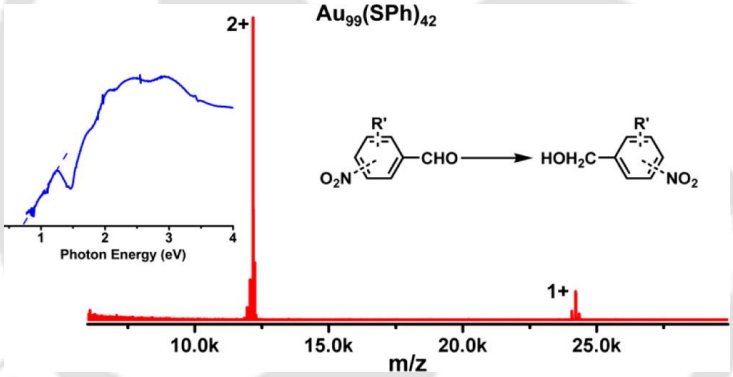

Fig. 1.3 Schematic illustration of hydrogenation of nitro benzaldehyde derivatives using Au NCs. (Reprinted with permission from reference 31. Copyright *J. Am. Chem. Soc.*, 2014, American Chemical Society).

1.1.3.3 Therapeutics and theranostics

Development of multifunctional nanocomposites, incorporated with nanoscale particles that operate in tandem, has been an important strategy for fabrication of effective theranostic agents. In this regard, nanocomposites comprising of luminescent NCs have been used for theranostic purposes.[33] For example, it has recently been demonstrated that Au NCs stabilized by chitosan polymer could be converted to nanoparticles and further be loaded with suicide genes for

inducing apoptosis in cervical cancer (HeLa) cells. Additionally, NCs being a functional component in the nanocomposite, could be used as an optical and flow cytometric (FACS) probe.[34] As per another report, multifunctional nanocomposites constituting of Au NCs could be loaded with doxorubicin and used for theranostic purposes. Additionally, the fabricated nanocomposite could be used for probing of cancer cells using one and two photon excitations.[35] On the other hand, copper nanoclusters have been demonstrated to generate reactive oxygen species (ROS). Thus when Cu NCs were administered to cancer cells, in combination with cisplatin (a known anticancer drug), they were found to enhance the therapeutic potential of the latter.[36]

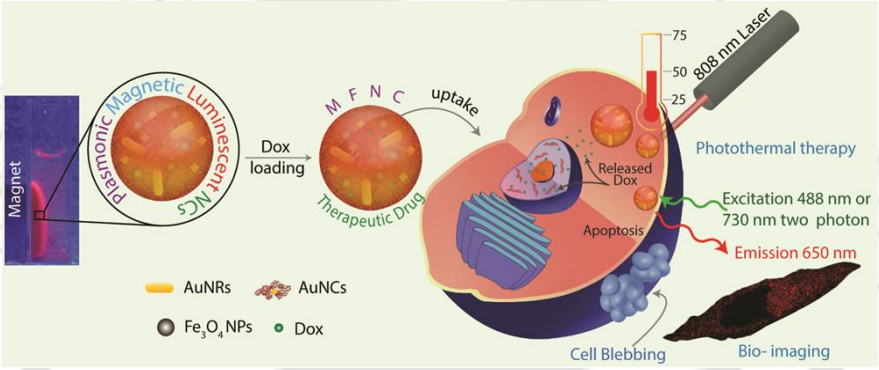

Fig. 1.4 Schematic illustration of drug delivery and photo thermal therapy using luminescent Au NCs based multifunctional nanocomposites. (Reprinted with permission from reference 33. Copyright *ACS Appl Mater and Interfaces,* 2016, American Chemical Society).

1.2 Assembly of Nanoclusters

The key challenge involving facile synthesis of noble metal NCs with appreciable luminescence quantum yield, high photo and chemical stabilities seems to have been addressed to a significant extent.[37-39] Further, exploring the versatile application potential of noble metal quantum clusters in the fields of optoelectronics, catalysis, theranostics and sensing have also been accomplished.[40-42] The next step towards further development in the field of NCs is envisioned to emerge from the idea of systematic organization of these NCs into higher order superstructures. This may lead to the advent of nanostructures with intriguing properties that are unattainable in the constituent building blocks (NCs). Further, the scope of harvesting the cumulative properties of the NCs confined in a superstructure, may confer the latter with superior application potential

in comparison to the constituents. In this regard, there are a few reports in the literature introducing important strategies for organizing NCs into higher order structures.

1.2.1 Ligand mediated assembly of NCs

Atomically precise NCs have been crystallized into various geometries based on interactions between the ligands stabilizing the NCs. For example, the total structure of $Au_{36}(SPh\text{-}tBu)_{24}$ have been deciphered following structural analysis using X –ray crystallography. It has been observed that the structure comprises of a FCC kernel constituting of 28 Au atoms, which are further protected by dimeric $Au_2(SR)_3$ motifs.[43] The observation of this FCC structured kernel of Au_{28} at a nanoscale was intriguing, as its parent analogue i.e., bulk gold is generally known to crystallize in FCC structures. In an allied vein, Liu and co-workers have reported the observation of body centered cubic (BCC) structured $Au_{38}S_2(S\text{-}Adm)_{20}$ NCs.[44] Further, Teo and co-workers have reported phosphine protected Au_{39} NCs into hexagonal close packed (hcp) structure.[45]

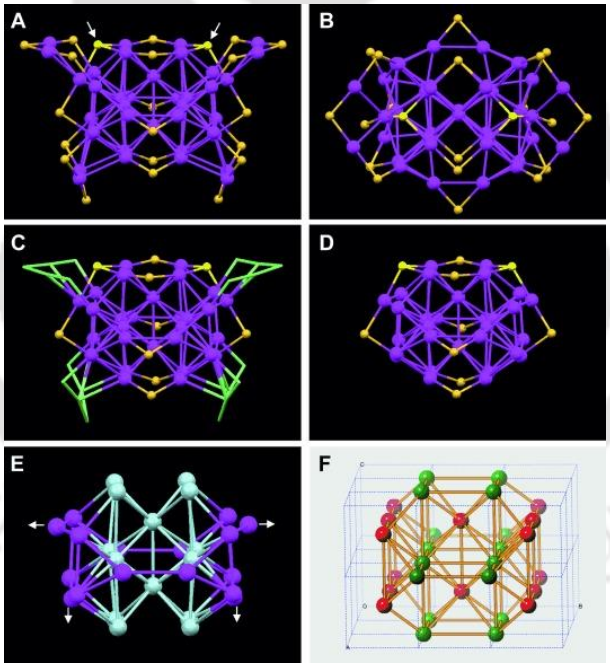

Fig. 1.5 Crystal structures of Au_{38} NCs arranged in a body centered cubic structure. (Reprinted with permission from reference 44. Copyright *Angew. Chem., Int. Ed. 2015*, John Wiley and Sons).

1.2.2 Self-assembly of NCs

In addition to ligand mediated assemblies, self-assembly of NCs has been an important strategy for hierarchical organizing atomic NCs.[46,47] For example, self-assembly of Au_{15} NCs into multilayered sheets has been a pursued based on supramolecular interaction among the NCs. One dimensional dipolar attraction is predominant in nanosized particles. The surface ligands protecting the Au_{15} NCs get redistributed following this 1D attachment, which eventually generates van der Waals interaction, finally leading to 2 dimensional assemblies of the NCs.[48] On a similar note, hydrogen bonding directed self-assembly of Ag NCs has been pursued. The assembled NCs led to the formation of octahedral nanocrystals. Further, gold nanorods (Au NRs) were encapsulated in the self-assembled Ag NCs.[49] In another study, solvent mediated self-assembly of Ag NCs into multi layered vesicles has been reported. Further, it has been demonstrated that upon switching from an aprotic to a protic solvent, the vesicles could be transformed to nanowire like structures. The critical role of hydrogen bonding in self-assembly formation and transformation from a particular morphology to another has been highlighted in this study.

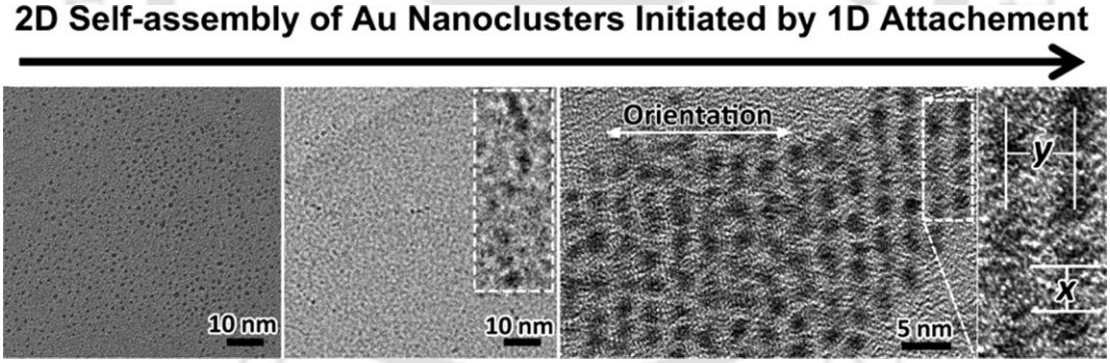

Fig. 1.6 TEM images showing the formation of two dimensional assembly of Au NCs initiated by one dimensional assembly. (Reprinted with permission from reference 48. Copyright *ACS Nano*, 2015, American Chemical Society).

1.3 Working for "A step ahead" in assembly of NCs

The aforementioned methods for systematic organization of NCs have been effective in formation of "Assembly of NCs". The studies discussed above have provided detailed insights in to the atomic structure of NCs. Also, understanding the critical role of ligands in the formation of

assembly of NCs has been possible by virtue of these reports. Notwithstanding the advantages of these methods in facile formation of "assembly of NCs", a vital concern that continues to beg solution is whether any method could be introduced for formation of "assembly of NCs" which could render the assembled NCs superior in terms of chemical and optical properties vis-à-vis the constituting NCs.

1.4 Context of the current thesis work

Herein we have introduced a "complexation reaction" based approach for formation of crystalline assembly of Au NCs using principles of inorganic chemistry. We have used zinc ions for chelation with the terminal groups of the ligands stabilizing Au NCs. This has led to the formation of crystalline assemblies of Au NCs with superior luminescence and application potential vis-à-vis the constituent Au NCs.

The current thesis is divided into seven chapters. The thesis work covers most aspects of NCs including synthesis and application of NCs, formation of crystalline assemblies of NCs and their superior application potential in comparison to the constituents NCs. Briefly,

Chapter 1 comprises of introduction and literature review. This chapter provides a concise idea about NCs and their assembly.

Chapter 2 describes the synthesis and application of luminescent Au NCs in detection of thumb imprint based diagnosis of hyperbilirubinemia.

Chapter 3 describes the formation of zinc assisted assembly of Au NCs for reversible storage and sensing of hydrogen at amenable conditions.

Chapter 4 describes the formation of zinc assisted assembly of Au NCs for chiral recognition and separation

Chapter 5 describes the formation of zinc assisted assembly of Au NCs for mitochondria targeted cancer theranostics

Chapter 6 describes the formation of zinc assisted assembly of Au NCs for storage and sensing of carbon dioxide via modulation of photoluminescence intermittency.

Chapter 7 consists of an overview of the thesis and future prospects.

Chapter 2

Thumb Imprint Based Detection of Hyperbilirubinemia Using Luminescent Gold Nanoclusters

Early and easy detection of diseases, using point-of-care and inexpensive devices, not only provides option for early treatment but also reduces the risk of propagation. Herein we report the fabrication of a robust film based luminescence indicator of bilirubin, which can indicate hyperbilirubinemia through the thumb imprint of the patient. The UV-light induced luminescence intensity of the film, made out of chitosan stabilised gold (Au) nanoclusters, which was effectively quenched in the presence of Cu^{2+} ions, recovered in the presence of bilirubin from skin or blood serum. Moreover, the sensitivity of detection of bilirubin was tuneable with the amount of Cu^{2+} added, thereby facilitating the detection of the desired concentration range of bilirubin.

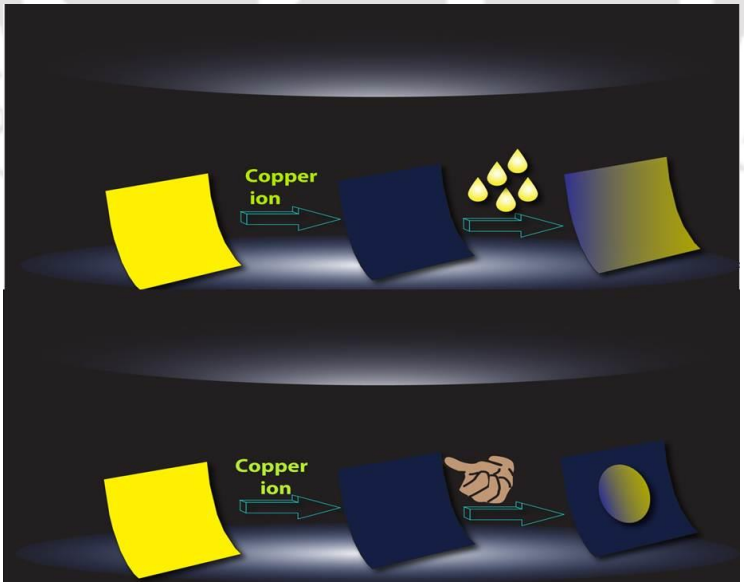

Basu et al. *Sci rep*. 2016, **6**, 39005.

2.1 Experimental Section:

2.1.1. Materials:

Chitosan (Sigma Aldrich), tetra chloro auric acid ($HAuCl_4$, Sigma Aldrich) mercaptopropionic acid (MPA, Sigma Aldrich), copper sulphate (Merck), bilirubin (BR, Alfa Aesar), glycine, sodium chloride and HCl were used as received. Milli-Q grade water was used for all experiments.

2.1.2. Synthesis of luminescent Au nanoclusters:

Au nanoclusters were prepared by adding 1.2 mL of aqueous solution of $HAuCl_4$ (10 mM) to 20 mL of 0.5 % (w/v) chitosan (which was solubilized using 0.1 % glacial acetic acid) under stirring condition. This was followed by addition of 0.8 mL mercaptopropionic acid (MPA; 0.11 M). Stirring was continued for 30 min and the pH of the resulting medium was kept at or below 2.5 using 0.01 M HCl.

2.1.3. Preparation of glycine buffer:

58.0 mg of sodium chloride was added with 75.0 mg glycine in 10.0 mL water. The pH of the resulting medium was kept at 2.5 using 0.01 M HCl.

2.1.4. Preparation of Au nanocluster dispersion for luminescence experiment:

To 0.1 mL of Au nanocluster dispersion prepared using the above mentioned protocol, 0.7 mL of glycine buffer was added. This was deemed essential to keep the absorbance value of the Au nanocluster dispersion below 0.1 in order to avoid self-absorption. Also, the pH of the medium was checked to ensure a value below 2.5. To this medium, required amount of copper sulphate and bilirubin solutions were added for further experiments.

2.1.5. Preparation of bilirubin solution:

Required amount of bilirubin was dissolved in appropriate amount of water and added with 1 µL of 1M NaOH.

2.1.6. Preparation of Au nanocluster containing film:

The medium (30 mL) containing as-synthesized Au nanoclusters was poured onto a petri dish (Tarsons, disposable sterile petridish) and was then allowed to dry overnight in an oven at 55 ºC. A film was formed with the approximate dimension of 3 × 3 cm^2. The intrinsic

luminescent properties of Au nanoclusters remained intact after the formation of the film. The film had yellow-orange luminescence upon excitation with 254 nm UV light.

In a similar way, the as-prepared Au nanocluster dispersion (1.0 mL) was drop-cast on an approximately 3 × 3 cm^2 polyvinylidene difluoride (PVDF) membrane and the coated membrane –following drying - was used for further experiments. Since the films have been subjected to evaporation following drop casting of gold nanoclusters, the intensity of luminescence of gold nanoclusters (upon exposure to UV light) on the periphery of the film showed higher intensity owing possibly due to "coffee-ring effect".

2.1.7. Treatment of the Au nanocluster containing film with copper sulphate:

The Au nanoclusters coated polyvinylidene difluoride (PVDF) membrane (as above) was treated with 0.2 mL $CuSO_4$ (12.5 mg/mL) solution. The film was then dried in air for 30 min and was observed under UV light. The luminescence intensity of the film got substantially reduced (upon exposure to 254 nm UV light) following addition of the copper salt.

2.1.8. Interaction of bilirubin solution with copper sulphate added Au nanocluster containing film:

0.2 mL aqueous solution of bilirubin (1.1×10^{-2} mg/mL) was added to Au nanocluster containing film, which was previously treated with 0.2 mL of $CuSO_4$ (12.5 mg/mL) solution. The film was then dried for 30 min and then was viewed using UV light. Recovery of the yellow-orange luminescence of the film was observed.

2.1.9. Interaction of copper salt with luminescent Au nanoclusters in liquid phase:

To the above prepared dispersion of Au nanoclusters (experimental section E), varying concentration of copper sulphate solution was added sequentially for various experiments. The concentration for each of the solutions of copper sulphate is mentioned in the respective figure legends.

2.1.10 Interaction of bilirubin with copper salt added luminescent Au nanoclusters in liquid phase:

To Au nanocluster dispersion added with different amounts of copper salt, varying amount of bilirubin (both laboratory chemical and present in the blood serum) was added for various experiments, the concentration for each of which is mentioned in the figure legends.

2.1.11. Control experiments:

Control experiments including addition of water of equal amount as that of bilirubin solution to copper sulphate added Au nanoclusters, addition of bilirubin to pristine Au nanoclusters, addition of a mixture of copper-bilirubin mixture to Au nanoclusters, effect of thumb imprint of a volunteer with bilirubin concentration in normal range on copper salt treated film of Au nanoclusters, effect of thumb imprint of a jaundice afflicted patient on a film (copper treated Au nanoclusters) immediately following imprint on a similar film were performed.

2.1.12. Collection of serum and thumb imprint of patients affected with hyperbilirubinemia

Serum and thumb imprints of jaundice patients were collected from hospital affiliated to Indian Institute of Technology Guwahati, India with full consent of the volunteers, following institutional protocol. Additional imprints were obtained from Guwahati Neurological Research Centre (GNRC) hospital, North Guwahati, Guwahati following appropriate procedure.

Results and discussions

Experimentally, luminescent Au nanoclusters in chitosan were synthesized by modifying a protocol established in the laboratory[34] (Fig.2.1).

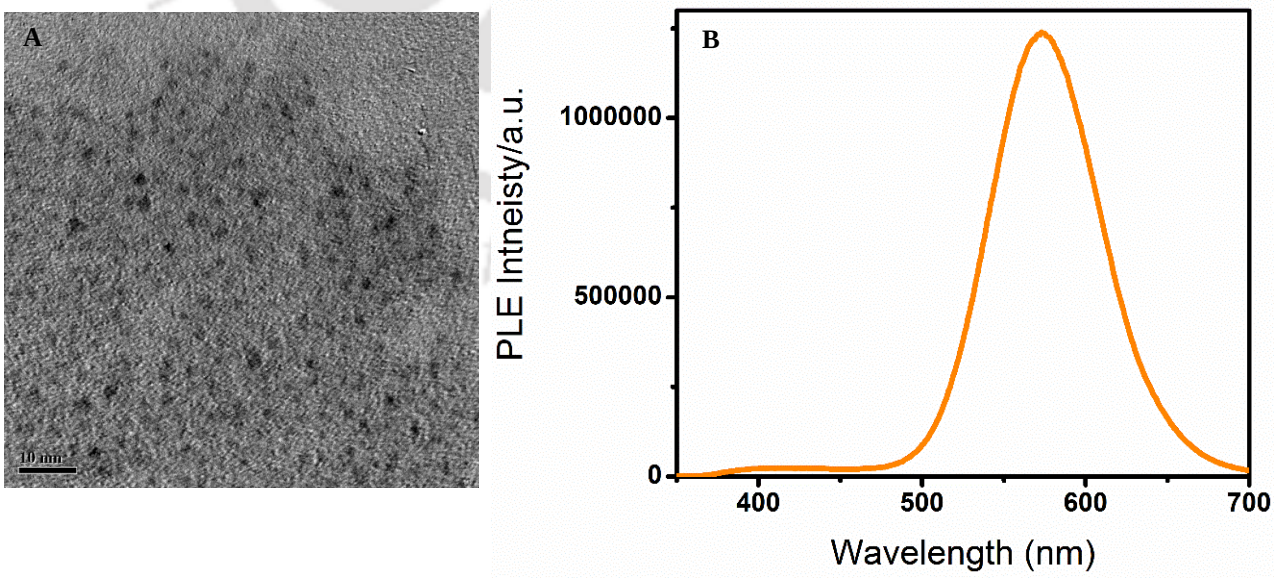

Fig. 2.1 (A**)** TEM image of as-synthesized Au nanoclusters. (B) Luminescence emission spectrum of as-synthesized Au nanoclusters. The excitation wavelength was set at 300 nm.

Gradual addition of copper sulphate solution (12.5 mg/mL) to the 0.8 mL aqueous dispersion of the clusters (0.1 mL Au nanoclusters dispersion and 0.7 mL glycine buffer) led to lowering of intensity of luminescence[41] (Fig. 2.2 A). The pH of the medium was maintained at 2.5 using glycine buffer, which was required for subsequent experiment as bilirubin is known to quench the luminescence of Au nanoclusters at above pH 2.59. Corresponding Stern-Volmer constant was calculated to be $(1.65 \pm 0.21) \times 10^{-3}$ M^{-1} (Fig. 2.2 B). It was further observed that addition of bilirubin to a system comprising of Cu^{2+} added Au nanoclusters (the luminescence of which was quenched due to the presence of Cu^{2+} ions) led to the recovery of the luminescence. Thus when a solution containing 1.38 mg/mL of copper ions in 0.8 mL Au nanocluster dispersion was subsequently treated with increasing amount of bilirubin, the intensity of luminescence increased systematically up to full recovery (Fig. 2.2 C).

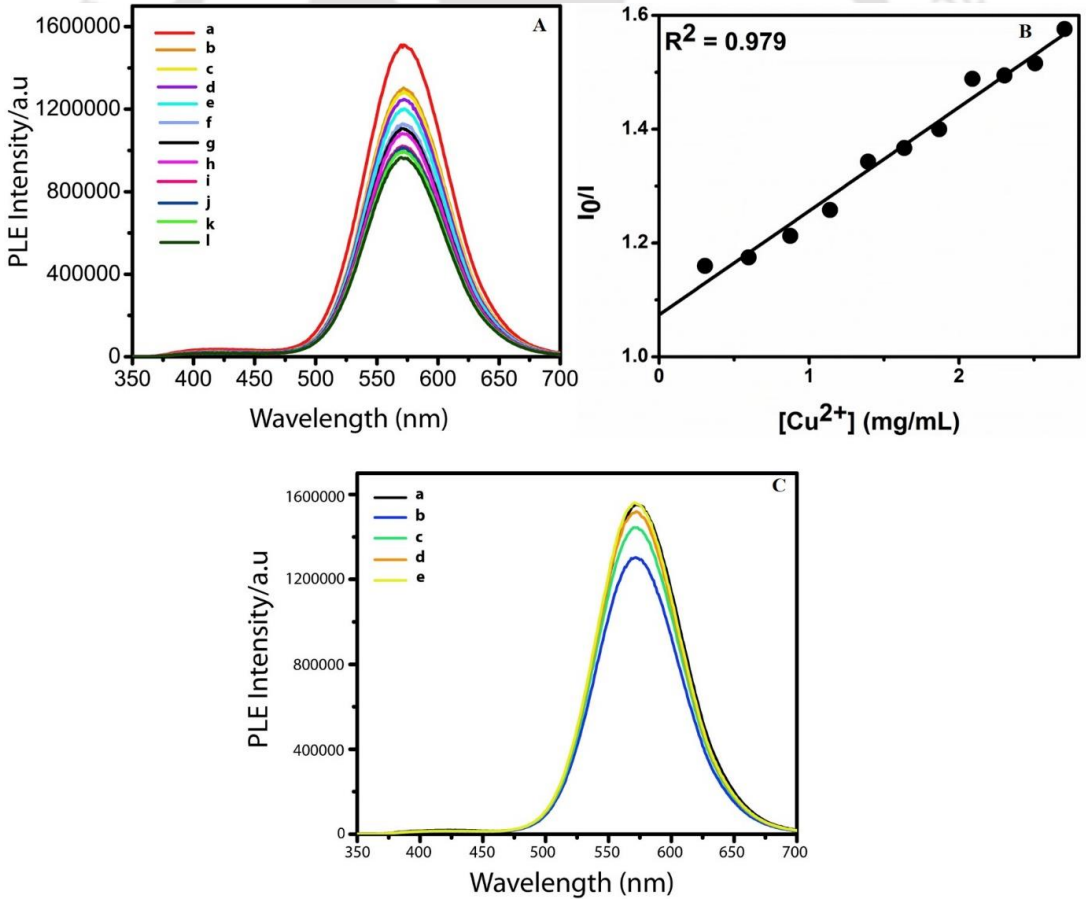

Fig. 2.2. (A) Gradual quenching of luminescence intensity of Au nanoclusters upon gradual addition of Cu^{2+}. Photoluminescence emission (PLE) spectrum of (a) Au nanoclusters and of that following addition of (b) 3.058×10^{-1} mg/mL, (c) 5.971×10^{-1} mg/mL, (d) 8.748×10^{-1}

mg/mL, (e) 1.14 mg/mL, (f) 1.393 mg/mL, (g) 1.635 mg/mL, (h) 1.867 mg/mL, (i) 2.090 mg/mL, (j) 2.303 mg/mL, (k) 2.505 mg/mL and (l) 2.704 mg/mL Cu^{2+} salt solution. (B) Corresponding Stern-Volmer plot. I_0 is the luminescence intensity of as-synthesized Au nanoclusters and I is the reduced luminescence intensity of the same on subsequent addition of Cu^{2+} ions. (C) The figure shows luminescence intensity quenching of Au nanoclusters upon addition of Cu^{2+} and recovery of the same on addition of BR (bilirubin). PLE spectrum of (a) Au nanoclusters and of that following addition of (b) 1.38 mg/mL Cu^{2+} and then (c) 5.8 × 10^{-4} mg/mL BR, (d) 1.1 × 10^{-3} mg/mL BR and (e) 1.5 × 10^{-3} mg/mL BR, respectively. BR means bilirubin.

Control experiment involving addition of water (instead of bilirubin solution) did not lead to significant change in the luminescence intensity (Fig. 2.3).

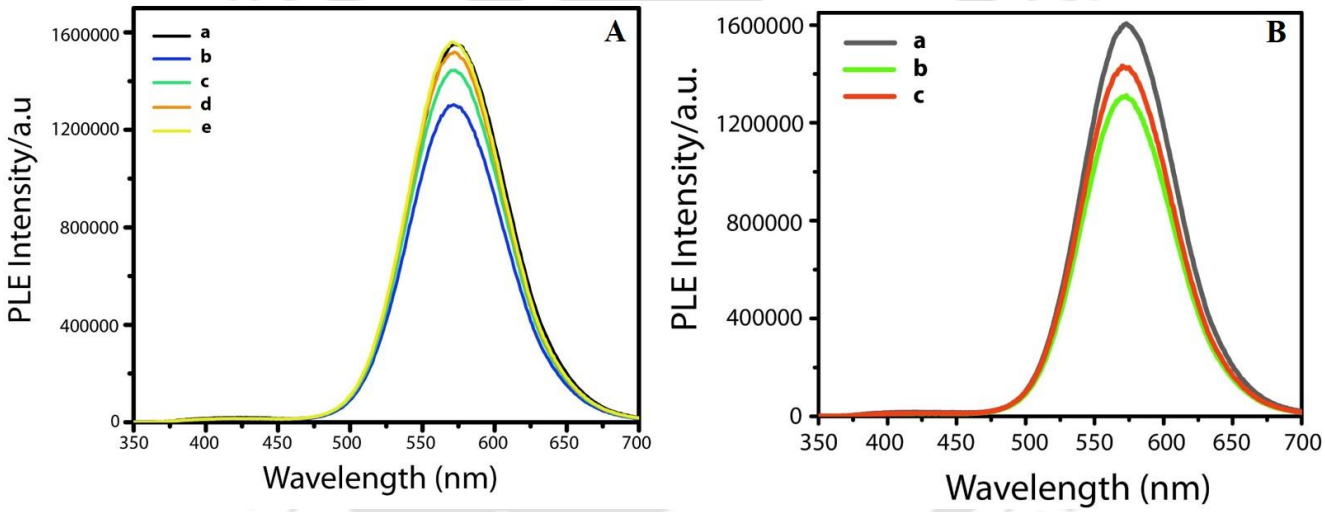

Fig. 2.3 Effect of the same amount (volume) of (A) bilirubin (in water); PLE spectra of (a) Au nanoclusters following addition of (b) 1.38 mg/mL Cu^{2+}, (c) 5.8 × 10^{-4} mg/mL BR, (d) 1.1 × 10^{-3} mg/mL BR and (e) 1.5 × 10^{-3} mg/mL BR and (B) water addition on the luminescence intensity of copper added Au nanoclusters (Au NCs) dispersion; PLE spectra of (a) Au nanoclusters following addition of (b) 1.38 mg/mL Cu^{2+} and (c) 150 µL of water (the same volume of BR showing full recovery of luminescence intensity as shown in (A)). BR means bilirubin.

Further bilirubin did not seem to have any effect on luminescence intensity of the clusters in the absence of Cu^{2+} ions (Fig. 2.4 A-B). Also, a mixture of Cu^{2+} (12.10 mg/mL) and bilirubin (5 × 10^{-4} mg/mL), when added to Au nanocluster dispersion, did not lead to significant change in luminescence intensity when compared to the effect of sequential

addition of copper ions and then bilirubin (Fig. 2.5). The results suggested important role of bilirubin in the restoration of Au nanocluster luminescence even in the presence of Cu^{2+} ions.

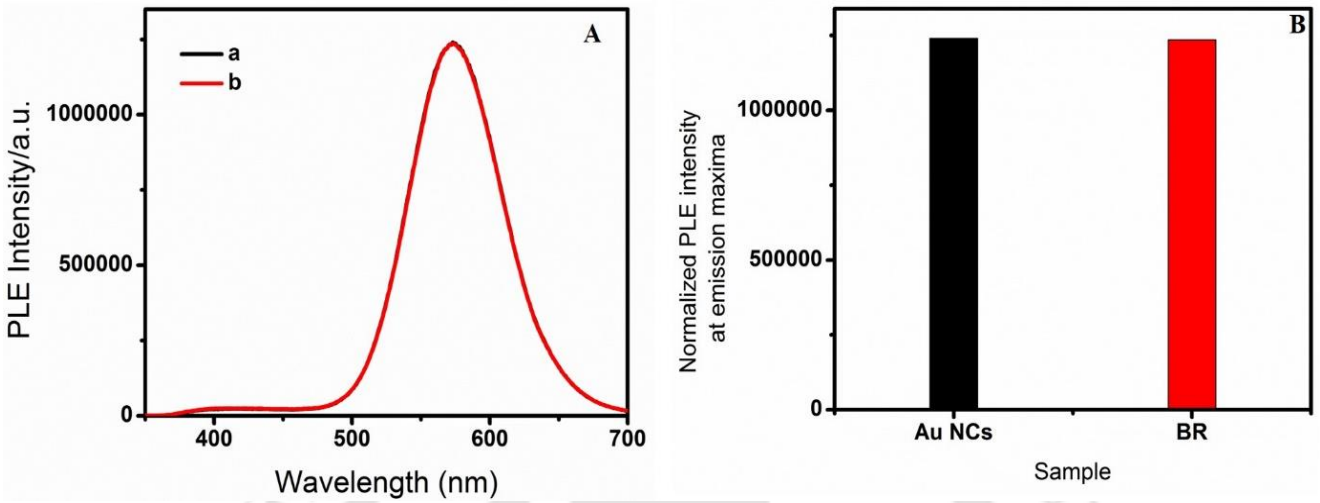

Fig. 2.4 A- B. Effect of bilirubin (BR) on luminescence intensity of as-synthesized Au nanocluster (Au NC) dispersion. (A) Photoluminescence emission (PLE) spectrum of Au nanoclusters (a) before and (b) after addition of bilirubin. (B) Normalized PLE intensity of Au nanoclusters before and after addition of bilirubin at emission maxima.

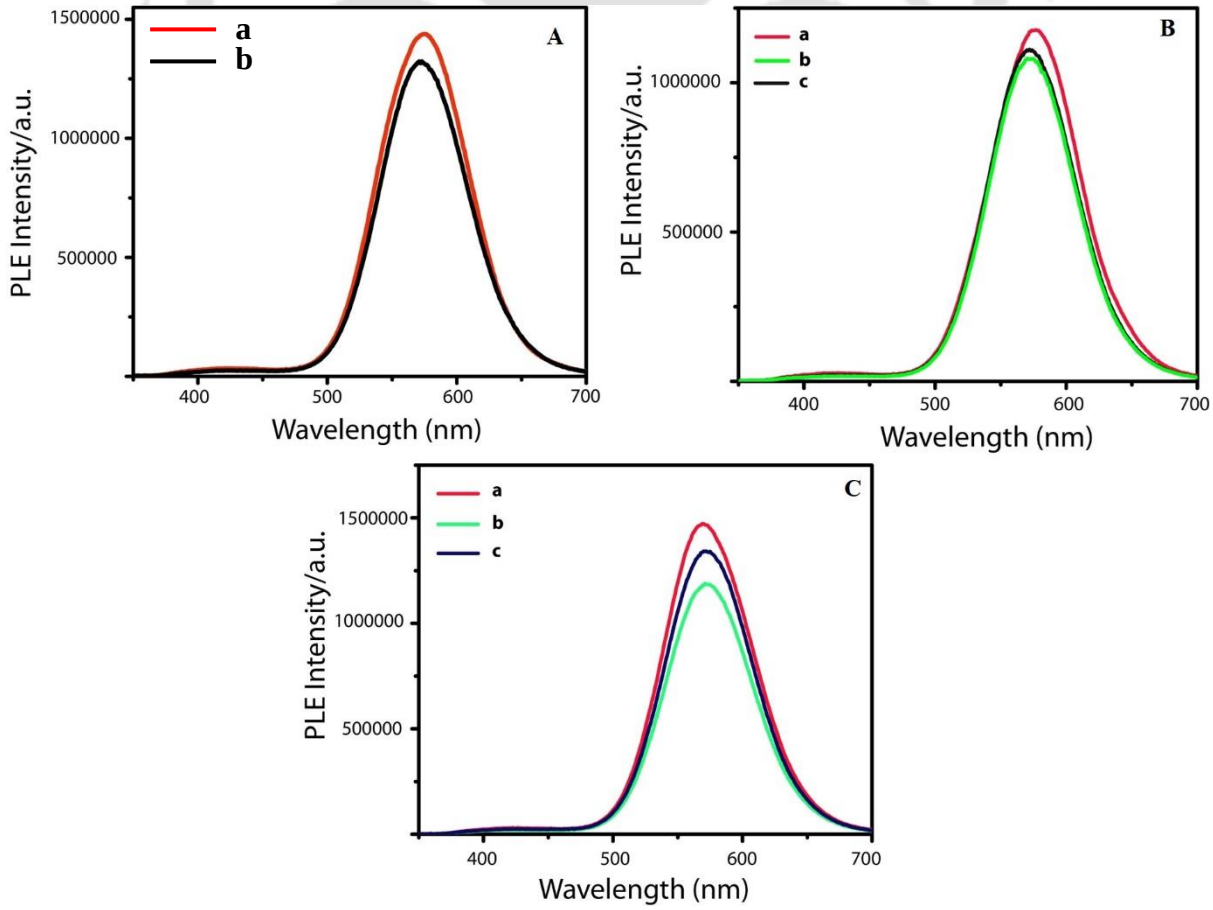

Fig. 2.5 A – C. Effects of addition of (A) Cu^{2+} ions and bilirubin mixture (Cu-BR); PLE spectra of (a) Au nanoclusters and Au nanoclusters treated with (c) Cu-BR, (B) water; PLE spectra of (a) Au nanoclusters, (b) Cu^{2+} and (b) Au nanoclusters treated with water and (C) Cu^{2+} ions followed by bilirubin (BR) on the luminescence of Au nanoclusters (Au NCs) dispersions; PLE spectra of (a) Au nanoclusters, Au nanoclusters treated with (b) Cu^{2+} and then (c) BR. BR means bilirubin.

Similar experiments were performed with different concentrations of copper ions and bilirubin (Fig. 2.6 A). Corresponding plots of recovery of luminescence versus concentrations of adducts (akin to Stern-Volmer plot) were obtained (Fig. 2.6 B). The purpose of the experiments was to find the lowest concentration of bilirubin, which would ensure the observation of change of luminescence with the highest sensitivity. It was found that bilirubin concentration as low as 8.4×10^{-3} mg/mL could provide detectable change in the luminescence intensity of Au nanoclusters (through recovery) in the presence of Cu^{2+} ions, the concentration of which could be as high as that of 4.77 mg/mL. On a similar note, blood serum of a jaundice patient with bilirubin concentration of 6.4×10^{-2} mg/mL was diluted a thousand times and added to Au nanoclusters dispersion with lower Cu^{2+} concentration (1.38×10^{-2} mg/mL). This also resulted in significant luminescence recovery. Thus, it was possible to detect varying amount of bilirubin just by tuning the amount of Cu^{2+} ions (table 2.1). The recovery of luminescence intensity of the nanoclusters by bilirubin in the presence of 4.77 mg/mL Cu^{2+} ions could be fitted with single exponential function. The results showed that use of higher concentration of Cu^{2+} ions in the medium helped detect higher amounts of bilirubin.

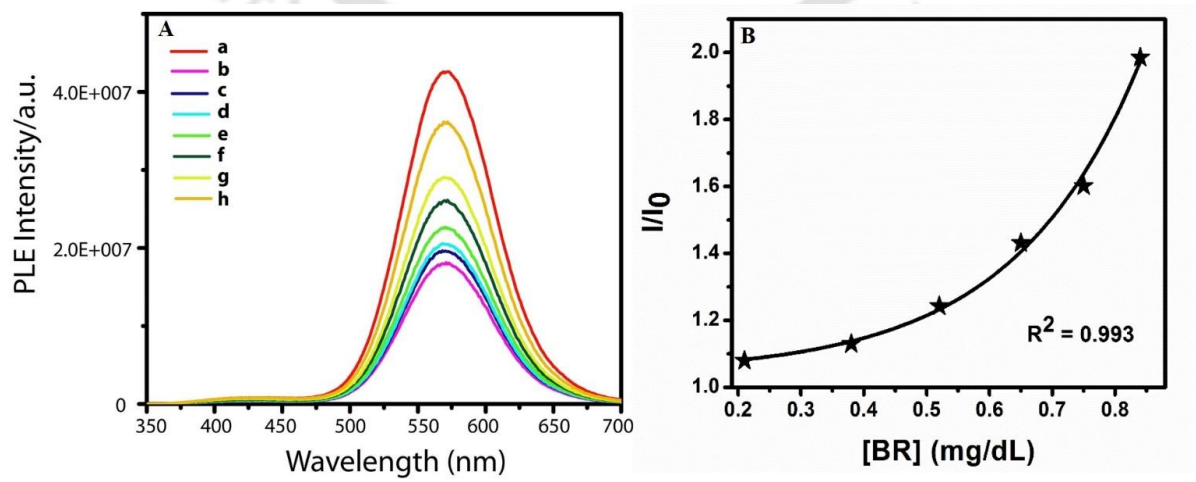

Fig. 2.6 (A) Graphs showing gradual luminescence intensity recovery of Au nanoclusters otherwise quenched in the presence of Cu^{2+} ions. PLE spectrum of (a) Au nanocluster dispersion and of that following addition of (b) 4.77 mg/mL Cu^{2+}, (c) 2.1×10^{-3} mg/mL BR, (d) 3.8×10^{-3} mg/mL, (e) 5.2×10^{-3} mg/mL BR, (f) 6.5×10^{-3} mg/mL BR, (g) 7.5×10^{-3} mg/mL BR and (h) 8.4×10^{-3} mg/mL BR, respectively. (B) Gradual increase of normalized luminescence intensity of the Cu^{2+} quenched Au nanocluster dispersion after addition of bilirubin. I_0 is the reduced luminescence intensity of the nanoclusters in the presence of copper ions. I is the recovered luminescence intensity on subsequent addition of BR. BR means bilirubin.

Table 2.1 The Variation in amount of bilirubin detected by tuning the concentration of Cu^{2+} ions.

Serial No.	Copper ion concentration	Bilirubin concentration
1.	**5.006×10^{-1} mg/mL**	**8.3×10^{-6} mg/mL**
2.	**1.38×10^{-2} mg/mL**	**6.4×10^{-5} mg/mL**
3.	**1.34 mg/mL**	**5×10^{-5}mg/mL**
4.	**1.38 mg/mL**	**5.8×10^{-4} mg/mL**
5.	**4.77 mg/mL**	**2.1×10^{-3} mg/mL**

Time-resolved photoluminescence measurements indicated average luminescence lifetime of as-synthesized Au nanoclusters to be 1.56 µs, which decreased to 1.29 µs upon addition of 0.2 mL of Cu^{2+} (5×10^{-4} M) and subsequently was restored to 1.53 µs upon further addition of bilirubin (from blood serum with bilirubin concentration of 6.4×10^{-5} mg/mL) (Fig. 2.7). The quenching of luminescence of Au nanoclusters by Cu^{2+} ions is likely to be dynamic in nature. This is apparent from the fact that in addition to the linear nature of the Stern-Volmer plot for quenching of luminescence of Au nanoclusters by Cu^{2+} ions, significant changes in the luminescence lifetime of the nanoclusters in the presence of Cu^{2+} was observed.

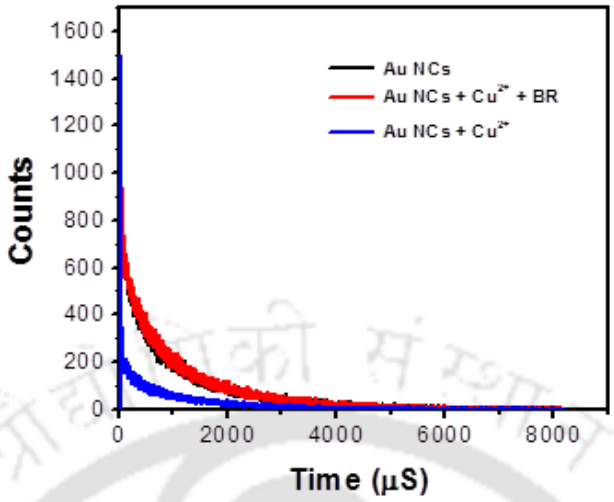

Fig. 2.7 Time-resolved luminescence spectra of Au nanocluster (Au NC) dispersion, Cu^{2+} ion treated nanocluster dispersion and that of Cu^{2+} ion treated nanocluster dispersion following treatment with bilirubin (BR).

Interestingly, UV-vis spectrum indicated the appearance of a peak at 350 nm owing to the Cu-bilirubin complex [51,52], which was neither present in the sample containing Au nanoclusters nor in Cu^{2+} ion added Au nanoclusters (Fig. 2.8). Thus, overall, while Cu^{2+} addition led to quenching of luminescence due to Au nanoclusters, addition of bilirubin led to recovery of the same, possibly owing to the formation of Cu-bilirubin complex [51, 52].

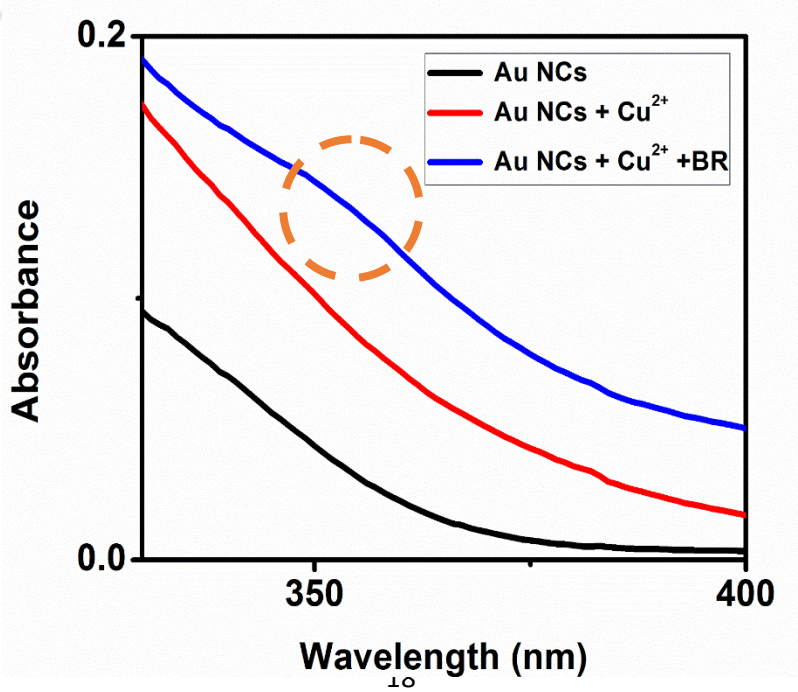

Fig. 2.8 UV-Vis spectra of as-synthesized Au nanocluster (Au NC) dispersion, Cu^{2+} ion treated nanocluster dispersion and that of Cu^{2+} ion treated nanocluster dispersion following treatment with bilirubin (BR).

Since the luminescence of the Au nanoclusters (embedded in chitosan) was responsive to the presence of Cu^{2+} ions and subsequently to bilirubin an opportunity was apparent with respect to making a device for the detection of bilirubin with high sensitivity. Also since bilirubin is known to form complex with Cu^{2+} having known stoichiometry[51], the detection could have the advantage of being quantitative. Further, common techniques which involve loss or lowering of luminescence in the presence of an analyte may not necessarily lead to detection with high sensitivity. On the other hand, recovery of luminescence in the presence of an analyte may offer unique opportunity of sensing with enhanced sensitivity. This – in principle – could provide an eminent opportunity for making a solid-state device for the above purpose.

In order to pursue the above objective, the as-prepared Au nanoclusters were drop-cast on a PVDF membrane (which was cut in the form of a film of ~ 2.8 ×2.8 cm^2 size) in which the bright yellow-orange luminescence of the clusters in the presence of UV light (254 nm) could easily be observed (Fig. 2.9 A). Further, when the film was treated with $CuSO_4$ (0.2 mL of 12.5 mg/mL) solution the luminescence disappeared nearly completely in the area where the liquid was dropped (Fig. 2.9 B). On the other hand, when the same film was further treated with 0.2 mL of 1.1×10^{-2} mg/mL bilirubin the luminescence recovered with great clarity (Fig. 2.9 C).

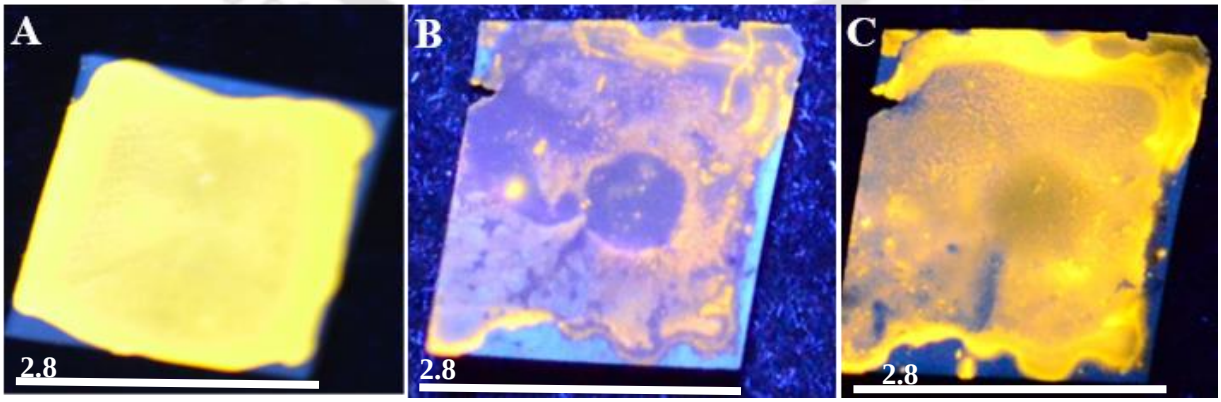

Fig. 2.9. Photograph of (A) Au nanocluster coated polyvinylidene difluoride (PVDF) membrane (with dimension of the films being 2.8 × 2.8 cm^2) as visualized under UV lamp with excitation at 254 nm. (B) Au nanocluster coated PVDF membrane as observed using

254 nm UV light, following addition of copper sulphate solution. The luminescence can be observed to have been reduced substantially. (C) BR (bilirubin) treated film as viewed using 254 nm UV light. The restoration of the intense yellow-orange color indicated recovery of luminescence of the film.

Control experiment, involving addition of water to the copper treated (and Au nanoclusters coated) PVDF membrane did not show restoration of luminescence intensity, thus clearly indicating the role of bilirubin in the recovery (Fig. 2.10). It is plausible that Cu^{2+} ions when present in the film (following addition of an aqueous solution of $CuSO_4$) acted as the quencher of luminescence. However, when bilirubin solution was added to the film, Cu-bilirubin complex formation might have taken place. The complex might not have quenched the luminescence and thus the recovery of luminescence was achieved. The above results indicated the potency of a new device in the form of solid film for the detection of bilirubin present in the aqueous medium.

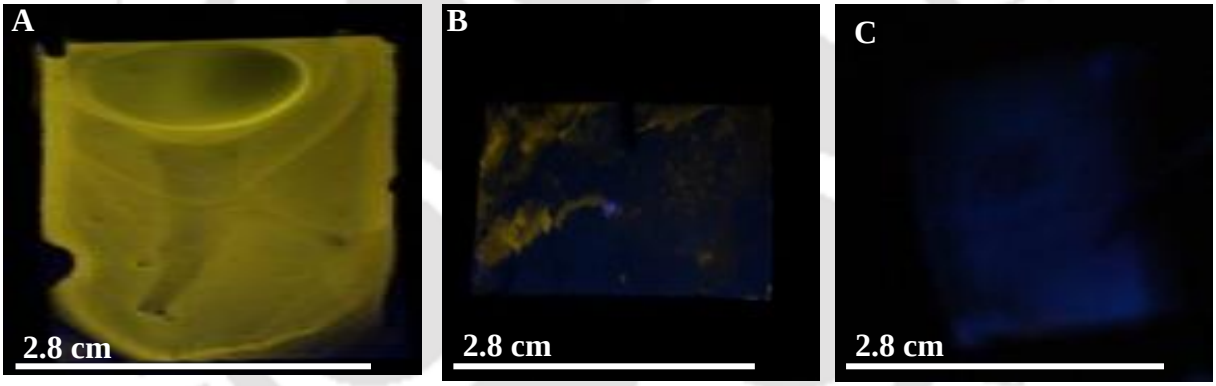

Fig. 2.10 (A) Photograph of the PVDF membrane coated with Au nanoclusters, (B) the same membrane after addition of copper salt showing quenching of luminescence, (C) the film in (B) after addition of water showing no recovery of luminescence intensity. All the photographs were recorded using 254 nm UV light excitation. Dimension of the films was ~ 2.8×2.6 cm^2.

As discussed above, bilirubin is known to be present in the skin of a person affected with hyperbilirubinemia. The fact that deposition of bilirubin occurs on skin of a jaundice afflicted patient, has been widely used as a tool to correlate serum bilirubin concentration. In this regard, various studies, including detailed theoretical study, involving mechanism of transfer of bilirubin from plasma to skin have been reported [53-55]. Thus, probing the molecular signature of a disease – for example hyperbilirubinemia in the present

study- through chemical reaction with another species, thereby leading to prominent optical changes, could emerge as a new avenue for disease diagnosis. Hence it was deemed feasible to test the efficacy of the device in detecting the presence of excess bilirubin through the thumb imprint of an affected patient. In order to test this a film (as above) was fabricated consisting of Au nanoclusters (embedded in chitosan) in PDVF membrane. The luminescence of the film was recorded using UV light as the excitation source (Fig. 2.11 A). The film was then treated with 0.02 mL of 12.5 mg/mL $CuSO_4$ solution upon which the luminescence disappeared (Fig. 2.11 B). Interestingly, when the thumb of a patient afflicted with hyperbilirubinemia was pressed against the copper-treated film for 5 min, the recovery of luminescence of the film could be observed (Fig. 2.11 C). Pathological test in the laboratory indicated the concentration of bilirubin in the patient's blood sample to be 3.1×10^{-2} mg/mL, which was well above the limit of concentration of a healthy adult. This experiment has been performed thrice to support the repeatability of the results.

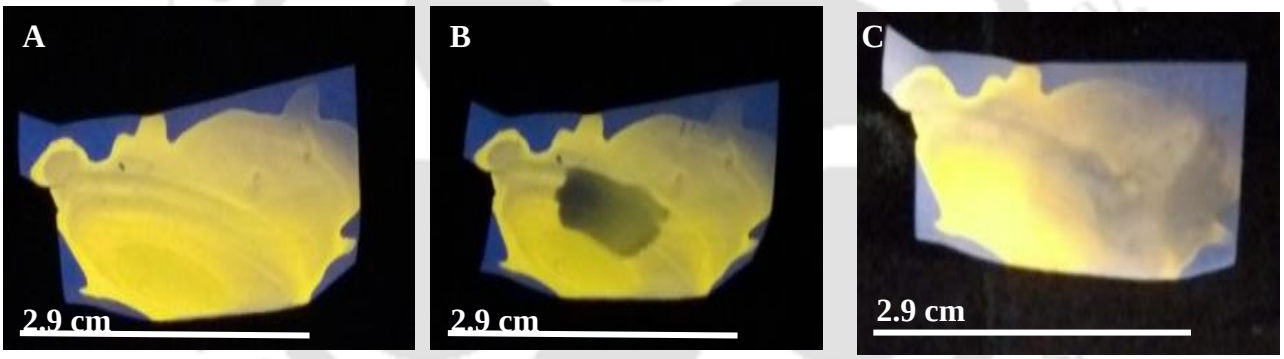

Fig. 2.11 (A) Digital photograph of Au nanoclusters containing PVDF membrane (dimension of the films was 2.9×2.1 cm^2). (B) Copper salt (20 µL 12.4 mg/mL) treated Au nanoclusters containing PVDF membrane. The low luminescence region is due to quenching by Cu^{2+} ions added to the membrane. (C) The same film after thumb impression of a jaundice afflicted patient. The photographs were recorded following illumination with UV light (254 nm).

In an analogous set of experiment, involving thumb imprint of a jaundice afflicted patient with bilirubin level recorded as 4.1×10^{-2} mg/mL, the quenched luminescence intensity of copper treated Au nanocluster film showed restoration of luminescence intensity when thumb imprint of the said patient was acquired on the film (Fig. 2.12).

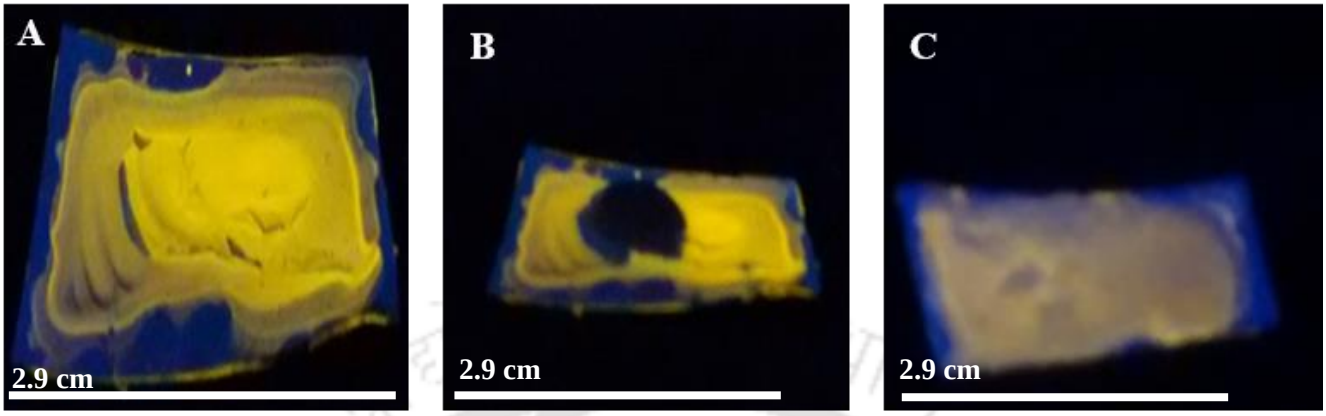

Fig. 2.12 (A) Photograph of Au nanocluster containing PVDF membrane (with the dimension of the films being 2.9 × 1.9 cm^2). (B) Copper salt treated Au nanocluster containing PVDF membrane. The low luminescence region is due to quenching by Cu^{2+} ions added to the membrane. (C) The same film after thumb impression of a jaundice patient. The photographs were recorded following illumination with UV light (254 nm).

On the other hand, when the same patient, immediately following the first impression, pressed the same thumb on another (similar) film of Au nanoclusters added with Cu^{2+} ions, no significant fluorescence recovery was obtained (Fig. 2.13 A-C). This could be due to insufficient bilirubin deposition on the patient's skin following the first impression.

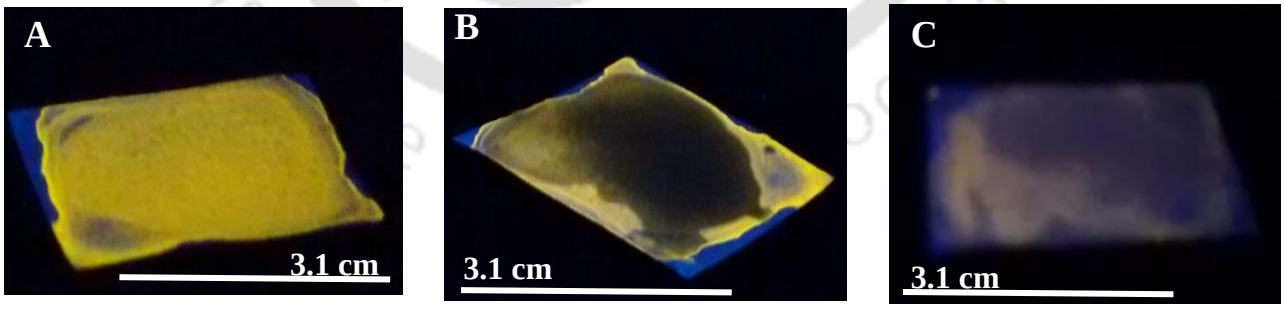

Fig. 2.13 (A) Photograph of Au nanocluster coated PVDF membrane. (B) Copper salt treated Au nanocluster containing film. The low luminescence region is due to quenching by Cu^{2+} ions added to the membrane. (C) The film (shown in (B)) after thumb impression of the same jaundice patient as in fig. 2.12, immediately following thumb imprint on film shown in figure

2.12. The photographs were recorded following illumination with UV light (254 nm). Dimension of the films was 3.1×2.2 cm^2.

Control experiment with healthy volunteer did not lead to any recovery of the luminescence of the copper-treated film (Fig. 2.14).

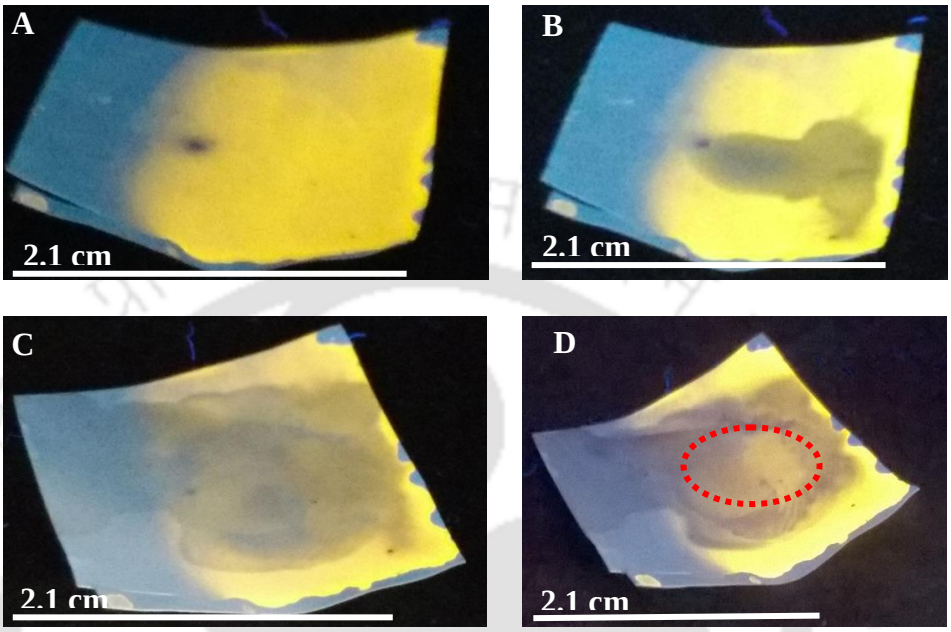

Fig. 2.14 (A) Digital photograph of PVDF membrane coated with gold nanoclusters. (B) Photograph of Cu^{2+} ion treated Au nanoclusters containing PVDF membrane. (C) The same film after thumb impression of a volunteer not affected with hyperbilirubinemia. (D) The film in (C) after addition of bilirubin (1.4×10^{-2} mg/mL). All the photographs were recorded following illumination with UV light (254 nm). Dimension of the films was 2.1×2.5 cm^2.

In an allied vein, detection of bilirubin in blood serum of a jaundice patient (total bilirubin count of 6.4×10^{-2} mg/mL) was also possible using the liquid phase method (Fig. 2.15).

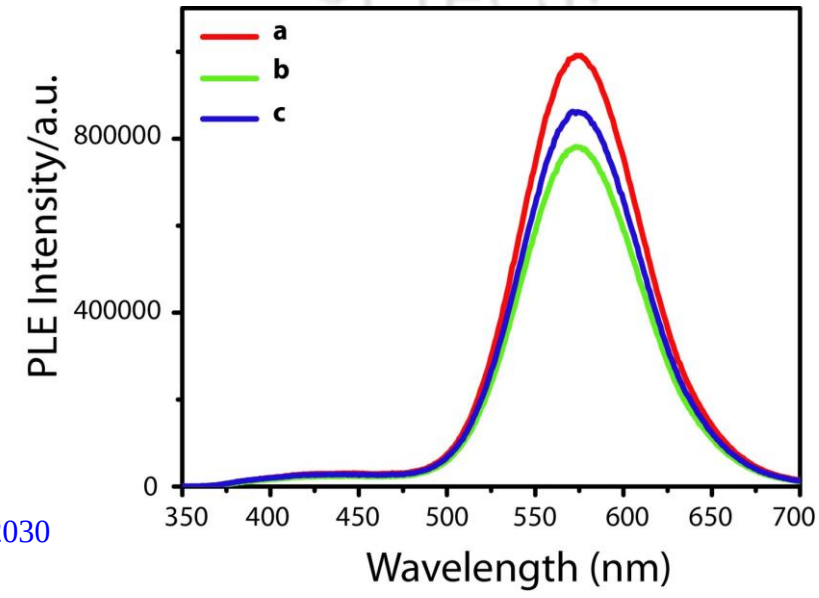

Fig. 2.15 Quenching of luminescence intensity due to Au nanoclusters (Au NCs) in the presence of Cu^{2+} ions followed by recovery of the same upon addition of blood serum containing bilirubin (BR) exceeding normal range. PLE spectra of (a) Au nanoclusters, and following treatment with (b) Cu^{2+} and (c) serum BR exceeding normal range.

Conclusions

In essence, we have developed a new nanotechnology-based fast and easy method of identifying hyperbilirubinemia in patient afflicted with jaundice. The method invented provided an option to circumvent the need of blood test for fast analysis and used thumb impression instead for testing of hyperbilirubinemia. The method (and the device) could be considered cost-effective and versatile, as the analysis could be performed, in minutes, without the need of a typical pathological laboratory setup. The method involved the use of luminescent Au nanocluster film, the intensity of which was effectively quenched in the presence of copper salt. The detection method relied on the recovery of luminescence intensity in the presence of bilirubin. The change in intensity was equally effective in liquid medium as well as in the solid phase, thus providing a detection with high sensitivity. The facile detection of bilirubin was possible using blood serum as well as through thumb impression of the patient. The best sensitivity of detection of BR in the liquid phase was 6.4×10^{-5} mg/mL and that in the solid phase was achieved with the concentration of blood bilirubin in serum of the affected patient being ~ 3.1×10^{-2} mg/mL. The bilirubin detection technique developed herein is based on complexation reaction between bilirubin and copper ions and thus offers superiority in terms of selectivity over other conventional luminescence quenching based methods. However, disease markers capable of forming stronger complex with copper ions as compared to bilirubin might interfere in detection method developed herein. Also, significant alteration in pH of the system (beyond the buffer capacity of glycine buffer used herein) might lead to complexity in detection of hyperbilirubinemia by the said method as the luminescence of chitosan stabilized nanoclusters used here is itself sensitive to pH. However, for the solid device such an effect may not arise. In a nutshell, the solid device thus designed is superior to the commonly practiced method as it enabled prompt, easy and precise detection of jaundice and could be used as a point-of-care device especially by common mass in a resource-limited region.

Chapter 3

Zinc Mediated Crystalline Assembly of Gold Nanocluster for Expedient Hydrogen Storage and Sensing

Programmed assembly of "few atom" quantum clusters portend to offer superior physicochemical properties of the new material in comparison to the constituents. We report the formation of luminescent crystalline inorganic complex, consisting of Zn^{2+} ions and L-histidine plus mercaptopropionic acid stabilized Au_{14} nanoclusters, with a complexation constant of $(9.7 \pm 6.6) \times 10^6$ M^{-1}. Analytical investigations, supported by computational modelling, indicated hexagonal structure of the crystal. The crystalline complex exhibited superior luminescence in comparison to ligand stabilized gold nanoclusters. Importantly, the complex stored hydrogen reversibly at room temperature, accompanied by change in the luminescence playing the role of sensing. The hydrogen adsorption capacity of the complex was determined to be 0.244 mM per gram of the complex at 20 °C and 20 bar.

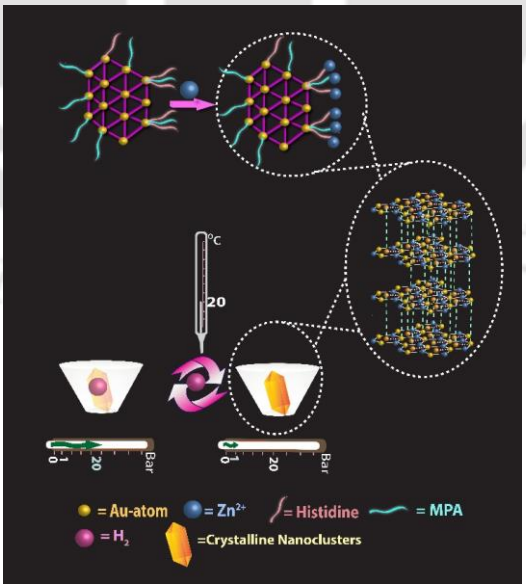

Basu et al. *J. Mater. Chem. A*, 2016,**4**, 1218-1223. Reproduced following the rules of royal society of chemistry. Copyright belongs to *J. Mater. Chem. A*, Royal society of chemistry.

3.1 Experimental Section

3.1.1 Materials

Tetrachloro auric acid ($HAuCl_4$, Sigma Aldrich), mercaptopropionic acid (MPA, Sigma Aldrich, 99%), histidine (His, Fluka), zinc acetate dihydrate (Merck, 99%), Rhodamine 6G (Sigma, 98%), quinine sulphate (Sigma Aldrich), sulphuric acid (Merck), potassium bromide (Sigma Aldrich) were used as procured without further purification. Water of Milli-Q grade has been used for experimental purpose.

3.1.2 Instruments

(a) Optical Measurements. Fluorescence and UV-Visible study of as synthesized and zinc added gold nanoclusters was done using HORIBA Jobin Yvon FluoroMax-4 spectrofluorimeter and Perkin Elmer, Lambda 750 UV-visible spectrophotometer respectively.

(b) Transmission electron microscopy (TEM) and selected area electron diffraction (SAED) analysis. TEM and SAED analysis of ligand stabilized gold nanoclusters and their product on reaction with zinc acetate was done using JEOL JEM 2100, at maximum accelerating voltage of 200 kV. TEM samples were prepared by depoisiton of aqueous dispersion of the samples on carbon coated copper grids.

(c) Powder X-Ray diffraction (PXRD) study. PXRD analysis of crystalline complex of ligand stabilized gold nanoclusters with zinc ions was done using X-Ray diffractometer TTRAX III 18kW; Rigaku Corporation, Tokyo, Japan, CuKα (λ = 1.5406 Å). Samples for PXRD analysis were prepared by evaporation of water followed by subsequent dispersion of the sample in methanol or water and evaporation of methanol.

(d) Fourier transform infrared (FTIR) spectroscopy. FTIR analysis of Au_{14} nanoclusters and zinc added nanoclusters was done using FTIR spectrophotometer Thermo Scientific instrument. Samples for FTIR were obtained by lyophilization of the aqueous dispersions of the samples.

(e) Time resolved photoluminescence (TRPL) study. Life-Spec-II spectrofluorimeter (Edinburgh Instrument) was used to perform TRPL analysis of as synthesized gold nanoclusters and zinc added gold nanoclusters. TRPL study was performed in continuous stirring conditon to prevent settlement of the samples.

(f) Matrix assisted laser desorption ionization –time of flight (MALDI-TOF) mass spectrometry. MALDI analysis was performed using Applied Bio systems 4800 Plus MALDI TOF/TOF analyzer. Sinnapinic acid was used as the matrix for MALDI analysis.

(g) Small angle X-Ray scattering (SAXS) experiment. SAXSpace instrument, Anton Paar, X-Ray generator ID3003 - Cu Kα (α = 0.1542 nm) was used for SAXS analysis.

(h) Thermogravimetric analysis (TGA). Perkin Elmer 4000 was used to record the TGA spectrum of crystalline complex of gold nanoclusters. Samples for TGA were prepared in a manner analogous to PXRD.

(i) Gas adsorption analysis. Sorption of hydrogen gas within crystalline complex of gold nanoclusters was performed using High pressure gas sorption analyser, Quantachrome instruments isorb HP1. For hydrogen sorption analysis, synthesis of crystalline complex of gold nanoclusters was performed following protocol discussed below using methanol or water as solvent. The obtained precipitate was dried by evaporating the solvent to dryness and purified by subsequent washing with methanol.

(j) Gas chromatography. Evolution of hydrogen from the crystalline complex upon reduction of pressure was verified from gas chromatography analysis using Agilent 7890A Network Gas Chromatograph system. The vial containing hydrogen purged dispersion of crystalline complex of gold nanoclusters was exposed to atmosphere and the solution was purged with argon to ensure removal of dissolved gases from the atmosphere. The vapour evolved from the dispersion was collected therein with a Hamilton syringe and the experiment was performed.

(k) Fluorimetric sensing of hydrogen adsorption and desorption: 2 mg of crystalline complex of gold nanoclusters was dispersed in 3 mL of hexane. The dispersion was purged with hydrogen was purged using a hydrogen balloon.

(l) Computational analysis. Structural modelling of the crystalline complex was done using Avogadro software.

(m) Simulation of ESI- MS spectra: The ESI-MS spectrum of $Au_{14}MPA_7His_5$ has been simulated using mMass – mass spectrometry tool. The simulated ESI-MS spectrum has been superimposed with the experimental spectrum.

3.1.3 Synthetic Methods

(a) Synthesis of gold nanoclusters. 10 mM $HAuCl_4$ was added to 10 mL of water followed by addition of 0.35 mL mercaptopropionic acid (0.11 M) under constant stirring at room temperature. To the resulting solution, 30 mg of histidine was added, which resulted in the formation of yellow luminescent gold nanoclusters.

(b) Formation of crystalline gold nanoclusters. To the solution of as synthesized gold nanoclusters, 150 mg of zinc acetate was added, which resulted in gradual settlement of colourless crystalline compound. The crystalline compound thus formed was brightly luminescent upon UV irradiation at 300 nm.

3.2 Results and discussions

Yellow luminescent Au nanoclusters, with quantum yield of 1.2 % and emission maximum of the major peak at 579 nm, were synthesized following sequential addition of MPA and His to an aqueous solution of $HAuCl_4$ at room temperature. Transmission electron microscopy (TEM) indicated formation of less than 2 nm particles, which seemed to have aggregated upon evaporation on the grid (Fig. 3.1). Selected area electron diffraction (SAED) pattern of the particles showed lack of crystallinity (Fig. 3.2). Matrix-assisted laser desorption ionization time-of-flight (MALDI-TOF) mass spectrometry of the sample indicated formation of Au_{14} nanoclusters ligated by MPA and His with the molecular formula $Au_{14}MPA_7His_5$ (m/z equal to 4261) (Fig. 3.3). The results were further substantiated by electrospray ionization mass spectrometry (ESI-MS). The parent peak (m/z = 1086) observed in ESI-MS is assigned to the presence of Au_{14} nanoclusters, which in ionized form appeared as $[Au_{14}MPA_7His_5 + 4\ Na]^{4+}$ (Fig. 3.4). On the other hand, the mixture of MPA and His - under similar conditions - did not show any prominent peak in ESI-MS analysis (Fig. 3.4 B, ESI†). Literature reports suggest planer structure of the Au_{14} cluster with hexagonal arrangement of Au atoms as the most stable form.[24] Additionally, a computed ESI-MS spectrum (Fig. 3.4) with the proposed structure is consistent with the experimental spectrum.

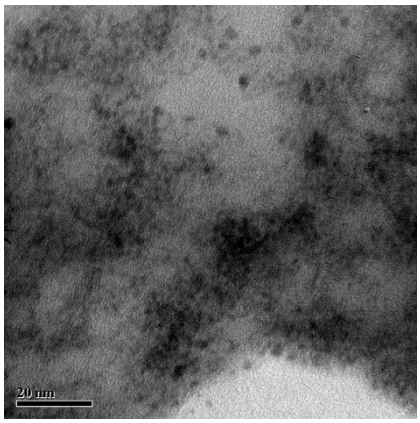

Fig. 3.1 Transmission electron microscopic **(**TEM) image of as-synthesised Au_{14} nanoclusters**.** The image shows formation of particles of diameter less than 2 nm, which had undergone aggregation, following evaporation of the dispersion on the TEM grid.

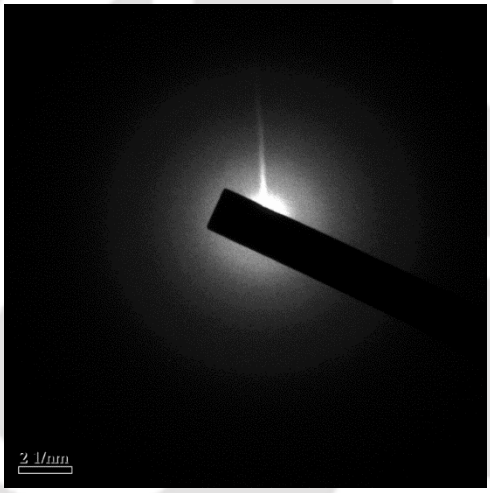

Fig. 3.2 Selected area electron diffraction (SAED) pattern of the sample containing the as-synthesised Au_{14} nanoclusters**.** As is evident from the image, the as-synthesized Au_{14} nanoclusters were devoid of distinct electron diffraction pattern

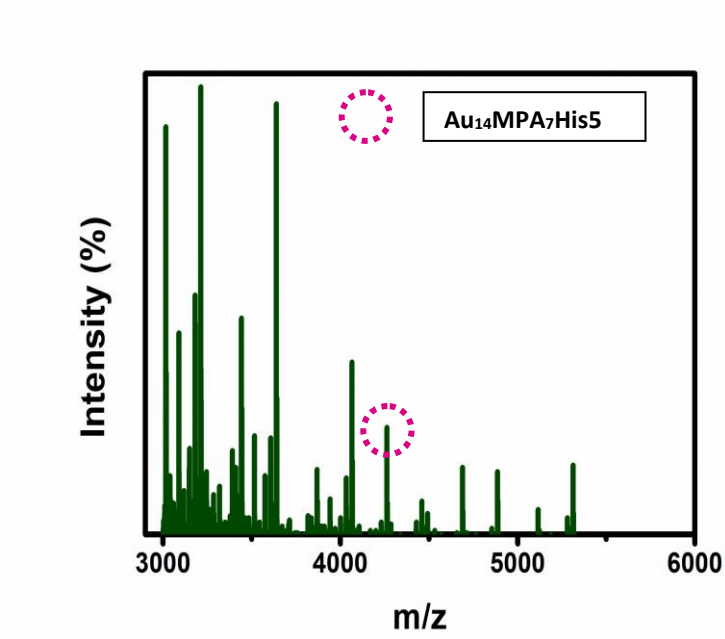

Fig. 3.3 Matrix assisted laser desorption ionization - time of flight (MALDI -TOF) mass spectrum of as synthesised Au_{14} nanoclusters. The spectrum was collected in reflector negative mode. The m/z value corresponding to Au nanocluster (encircled in dots) is m/z 4261, which substantiates the molecular formula of the cluster to be [$Au_{14}MPA_7His_5$].

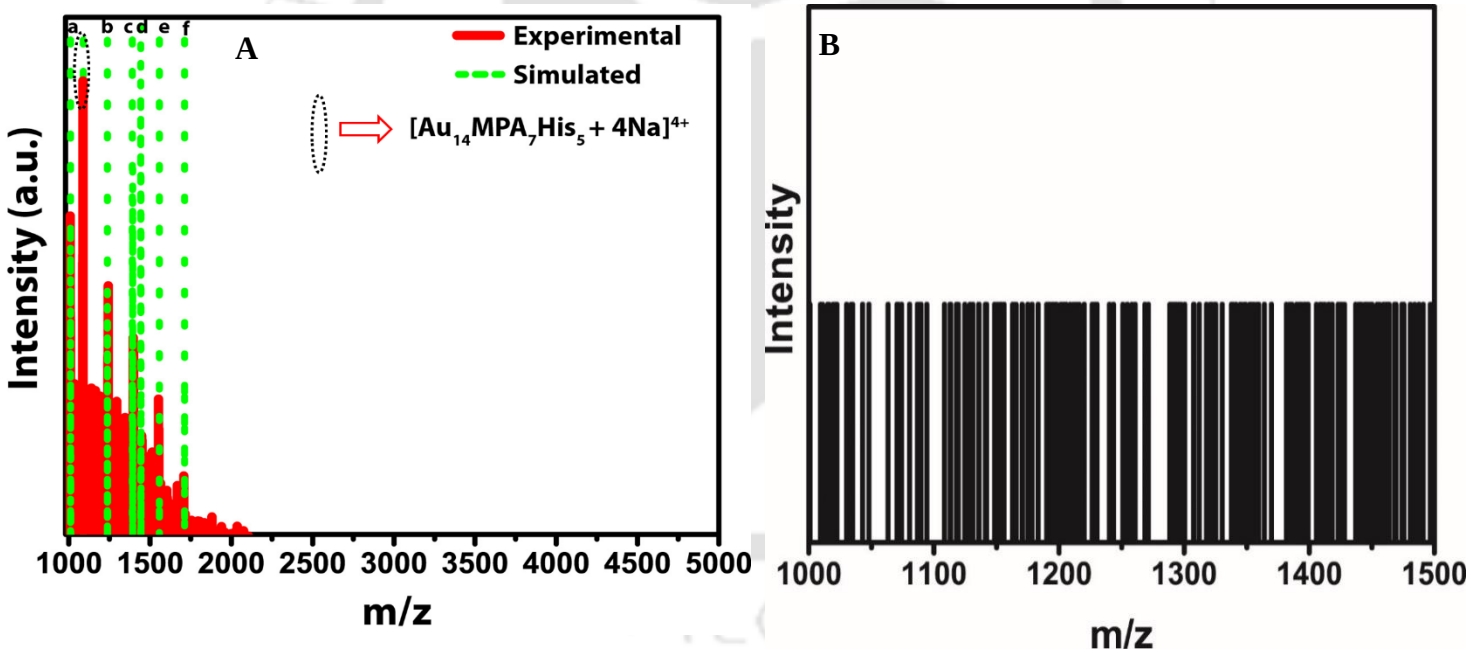

Fig. 3.4 Electrospray ionization mass spectra (ESI-MS) of **(A)** $Au_{14}MPA_7His_5$. The fragments in addition to the parent peak (assigned in the figure legend) are as follows: a: $[Au_{14}MPA_7His_3 +4\ Na]^{4+}$; b: $[Au_{14}MPA_7His_1 +3\ Na]^{3+}$; c: $[Au_{14}MPA_7His_4 +3\ Na]^{3+}$; d: $[Au_{14}His_2 +2\ Na]^{2+}$; e: $[Au_{14}His_4 +2\ Na]^{2+}$ and **(B)** a mixture of histidine and MPA. The simulated ESI-MS spectrum (serrated lines) has been superimposed with the experimental spectrum (solid lines).

Addition of zinc acetate to the as-prepared Au_{14} nanocluster dispersion led to stronger yellow emission. The enhancement of luminescence intensity was accompanied by a 13 nm red-shift of the emission maximum of the major peak with no significant change in the weaker peak (Fig. 3.5 A). The luminescence life time of the nanoclusters increased significantly upon complexation with zinc ions (Fig. 3.5 B –C). The lifetime of the longest emitting component of the nanoclusters was recorded to be 50.74 ns, whereas upon complexation with zinc ions the same was observed to be 1.26 μs (Table 3.1). The prominent change in lifetime could be attributed to the structural confinement imposed on the nanoclusters following complexation with zinc ions.[56] It has been reported that when Zn^{2+} ions are added to peptide-stabilized anionic Au nanoclusters assembly formation occurs, leading to the enhancement of photoluminescence intensity.[57] Also, complexation reaction between Zn^{2+} and MPA or His is known to be facile. Thus the shift of emission maximum, enhancement of intensity as well as increment in luminescence lifetime of ligand stabilised nanoclusters in here may well be due to (complexation) reaction between the ligand stabilized Au_{14} nanoclusters and Zn^{2+} ions. Moreover, the complexation constant associated with the reaction between nanoclusters and zinc ions, as defined by equation 1, is calculated to be $(9.7 \pm 6.6) \times 10^6$ M^{-1} (Fig. 3.5 D-E). This was achieved by pursuing reaction of the as-synthesized nanoclusters with different concentrations of Zn^{2+}. The reaction as well as formation of product was followed by the change in photoluminescence intensity for the peak at 576 nm.

$$AuNC + Zn^{2+} \rightarrow ZnAuNC \qquad (1)$$

MALDI-TOF mass spectrometry analysis of the product indicated the presence of a mass fragment m/z 4326, in addition to fragments corresponding to ligand-stabilized Au_{14} clusters (Fig. 3.5 F). This was assigned to the presence of a zinc complex with the formula $Au_{14}MPA_7His_5Zn$. It may be mentioned here that when zinc acetate was added to the ligand-stabilized cluster medium, precipitation could be observed to occur within seconds, which was allowed to settle for 2 min. The precipitate could not be separated by centrifugation; however, the top liquid part could be decanted and the remainder was used for analysis.

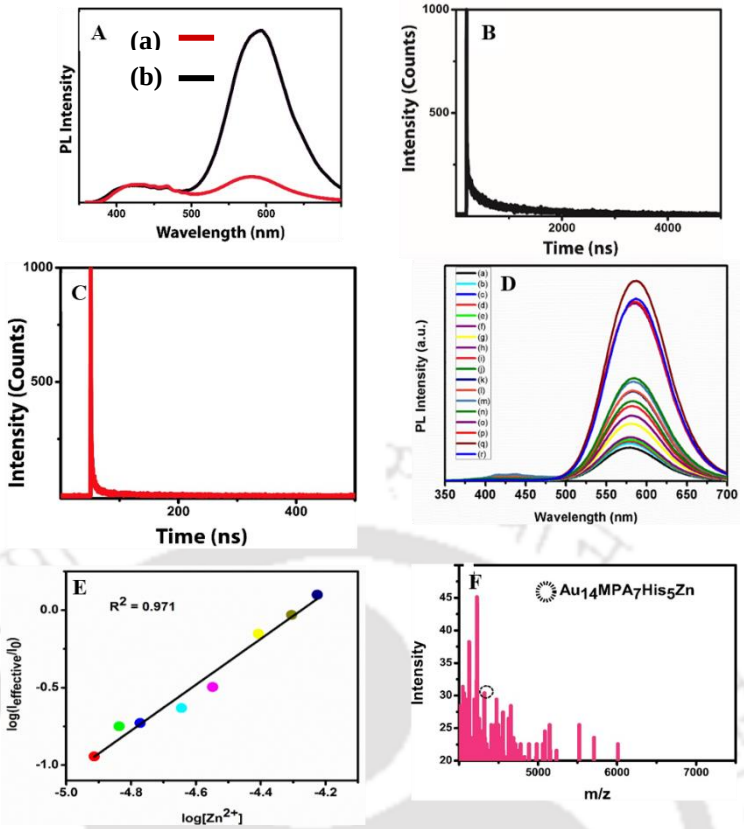

Fig. 3.5 (A) Photoluminescence spectra of (a) as synthesized Au_{14} nanoclusters and (b) Zn^{2+} salt added Au_{14} nanoclusters. The excitation wavelength was set at 300 nm. Time-resolved photoluminescence spectra of (B) the product of reaction of Au_{14} with zinc acetate and (C) ligand stabilized Au nanoclusters. (D) Photoluminescence spectra of the Au_{14} nanoclusters upon sequential addition of Zn^{2+} salt solution showing gradual enhancement of intensity. Spectra of (a) Au_{14} nanoclusters, (b) 10 µL, (c) 12 µL, (d) 14 µL (e) 19 µL, (f) 24 µL, (g) 34 µL, (h) 44 µL, (i) 54 µL, (j) 64 µL, (k) 74 µL, (l) 84 µL, (m) 94 µL, (n) 104 µL of 0.5 mM Zn^{2+} salt and following this after addition of (o) 10 µL, (p) 20 µL, (q) 30 µL (r) 40 µL of 10 mM Zn^{2+} salt. (E) Corresponding plot of Log($I_{effective}$/ I_0) versus Log [Zn^{2+}] based on the graphs in (D). (F) Matrix assisted laser desorption ionization - time of flight (MALDI -TOF) mass spectrum (acquired in reflector negative mode) of Zn^{2+} salt added Au_{14} nanoclusters.

Table 3.1 Decay Parameters of ligand stabilised Au_{14} nanoclusters and the product of their reaction with zinc acetate. The analysis was performed using laser of 375 nm. The data were fitted using tri exponential fitting parameters.

Sample	A_1 (%)	r_1 (ns)	A_2 (%)	r_2 (ns)	A_3 (%)	r_3 (ns)	χ^2
Ligand stabilised Au nanoclusters	22.01	0.527	37.01	5.130	40.98	50.739	0.97
Zinc added Au nanoclusters	5.128	7.575	19.99	144.100	74.88	1263	1.08

Further evidences of complexation between Zn^{2+} and ligand-stabilized Au_{14} nanoclusters came from TEM measurement of the product. The TEM image (Fig. 3.6 A) showed no additional feature except for the formation of larger agglomerated particles (in comparison to as-synthesized nanoclusters). On the other hand, selected area electron diffraction (SAED) of the particles clearly evidenced the presence of crystalline structure with hexagonal arrangements of the constituent elements (Fig. 3.6 B). On the other hand, as is evident from Fig. 3.6 C and high resolution TEM (HRTEM) analysis (obtained following inverse fast Fourier transformation, IFFT) (Fig. 3.6 D), the distance between two hexagons of adjacent planes was observed to be 5.0 Å. The structure of the crystalline complex, as obtained from the electron diffraction and other analyses, was further substantiated by computational modelling using Avogadro [58] (Fig. 3.7 A). A general three dimensional structure representing the crystalline complex is depicted in Fig. 3.7 B.

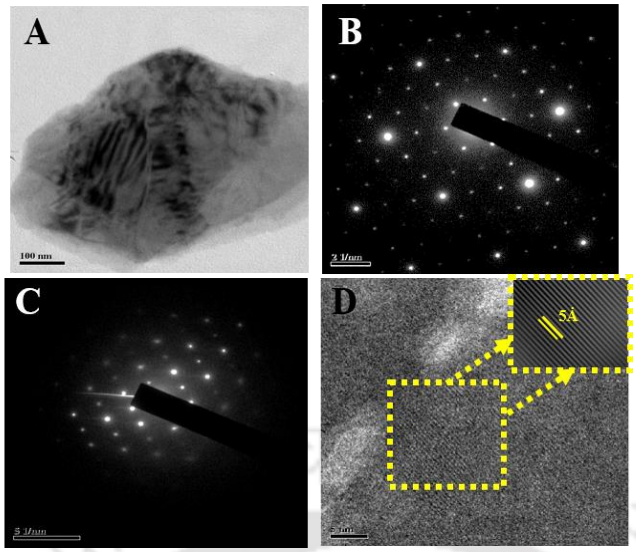

Fig. 3.6 (A) Transmission electron microscopy (TEM) image of the crystalline precipitate obtained following addition of Zn^{2+} salt to Au_{14} nanoclusters in the liquid medium. (B) Corresponding selected area electron diffraction (SAED) pattern. (C) SAED pattern of the crystalline precipitate along different zone axis highlighting the interplanar distance in the crystal. (D) High resolution TEM (scale bar is 5 nm) and corresponding inverse fast Fourier transform (IFFT, in the inset) images of the crystal.

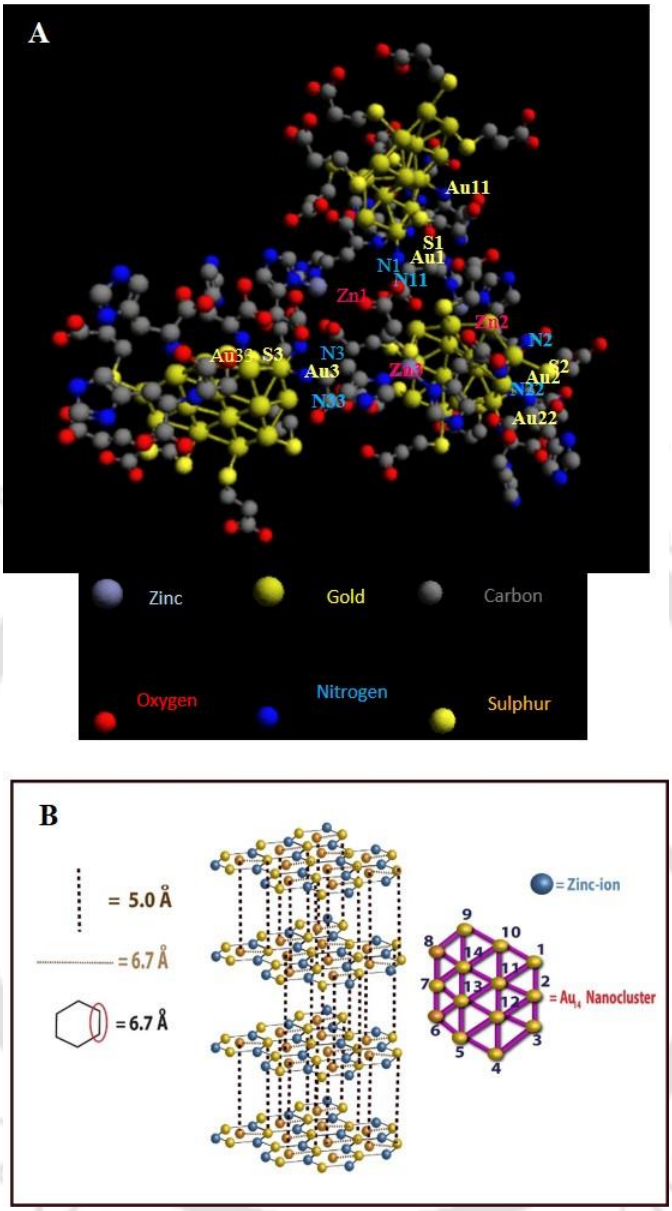

Fig. 3.7 (A) Computationally optimized structure of $Au_{14}MPA_7His_5Zn$ obtained using Avogadro software. Hydrogen atoms have not been included for simplicity. (B) A model structure, representative of crystalline $Au_{14}MPA_7His_5Zn$.

Additionally, scanning transmission electron microscopy-energy dispersive X-ray (STEM-EDX) spectroscopy measurements showed the presence of zinc and gold atoms (Fig. 3.8 A) in the region of the crystal, which was subjected to SAED (Fig. 3.8 B) and STEM (bright field (Fig. 3.8 C) and dark field (Fig. 3.8 D) analyses. The

analysis was further extended to elemental mapping, which showed simultaneous presence of zinc and gold atoms on the area of the crystal under observation (Fig. 3.9). Thus the results clearly indicated the formation of crystalline particles with luminescent $Au_{14}MPA_7His_5Zn$ as the constituent. Precisely, the SAED pattern indicated that the crystal comprised of unit cells organized in regular hexagonal pattern. The average edge length of each side of the hexagon was computed to be 6.70 ± 0.15 Å. Interestingly, periodic presence of spots of relatively higher intensity with distance of separation 2.20 ± 0.03 Å could also be observed. This may be attributed to the presence of the planar Au_{14} clusters aligned perpendicular to the regular hexagon and pointing towards the center of the hexagon as explained later.

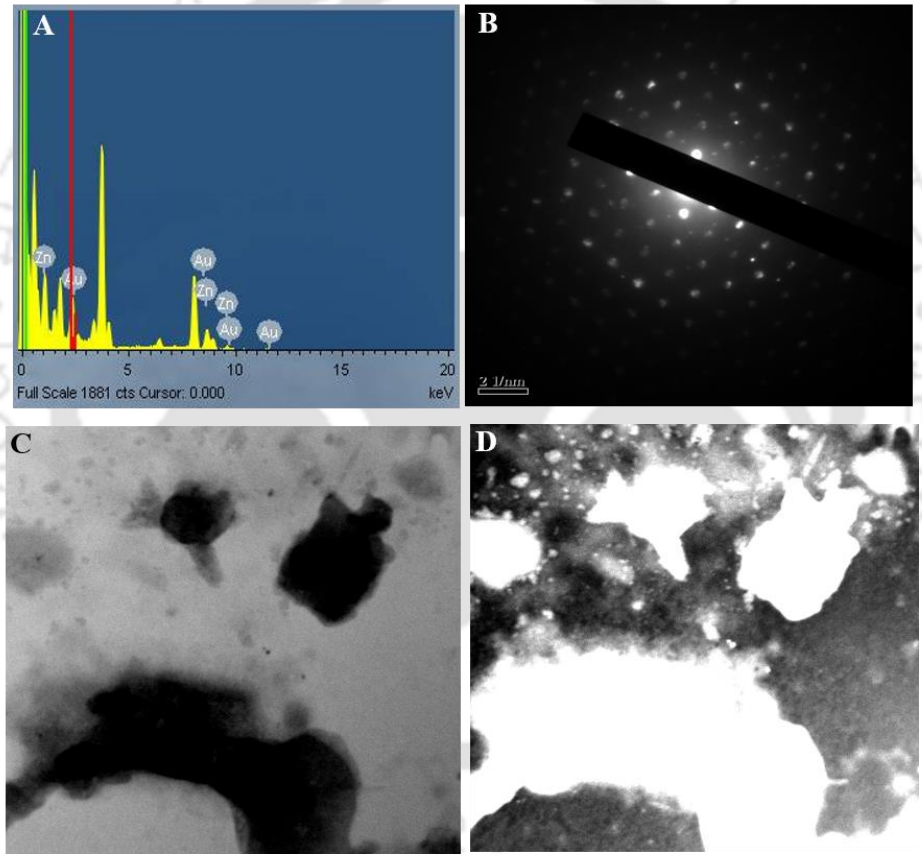

Fig. 3.8 (**A**) STEM-EDX analysis of $Au_{14}MPA_7His_5Zn$. **(B)** Selected area electron diffraction (SAED) of crystalline complex of $Au_{14}MPA_7His_5Zn$. **(C)** Bright field scanning transmission electron microscopic (STEM) image of $Au_{14}MPA_7His_5Zn$. **(D)** Dark field STEM image of $Au_{14}MPA_7His_5Zn$.

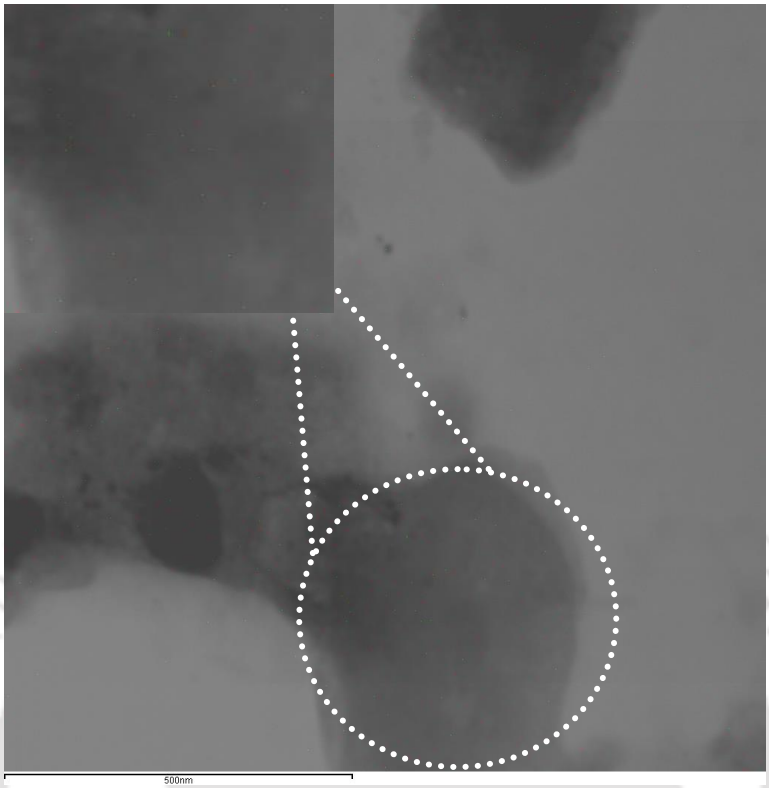

Fig. 3.9 Elemental mapping analysis of $Au_{14}MPA_7His_5Zn$. Au is represented by green spot and zinc by red spot.

Additional evidences of complexation between Au_{14} nanoclusters and zinc ion were revealed from FTIR (Fig. 3.10 A-B) and thermo-gravimetric (TG) analyses (Fig. 3.11). FTIR spectroscopic analysis revealed that the binding of zinc ion to His might have occurred through imidazole nitrogen. The weight losses of various components of the product of reaction between Au_{14} nanoclusters and zinc ion as obtained from TGA study, were in well accordance with proposed chemical formula of the complex to be $Au_{14}MPA_7His_5Zn$. Interestingly, the inter-planar dimensions obtained from SAED analysis did agree well with powder X-ray diffraction pattern (Fig. 3.12), assuming first order Bragg's diffraction). Even more intriguingly, the particle size of 5.2 nm, as calculated by employing Scherrer equation to the peak at 22°, was in agreement with that obtained from small angle X-ray scattering (SAXS) analysis (5.5 nm) (Fig. 3.13).

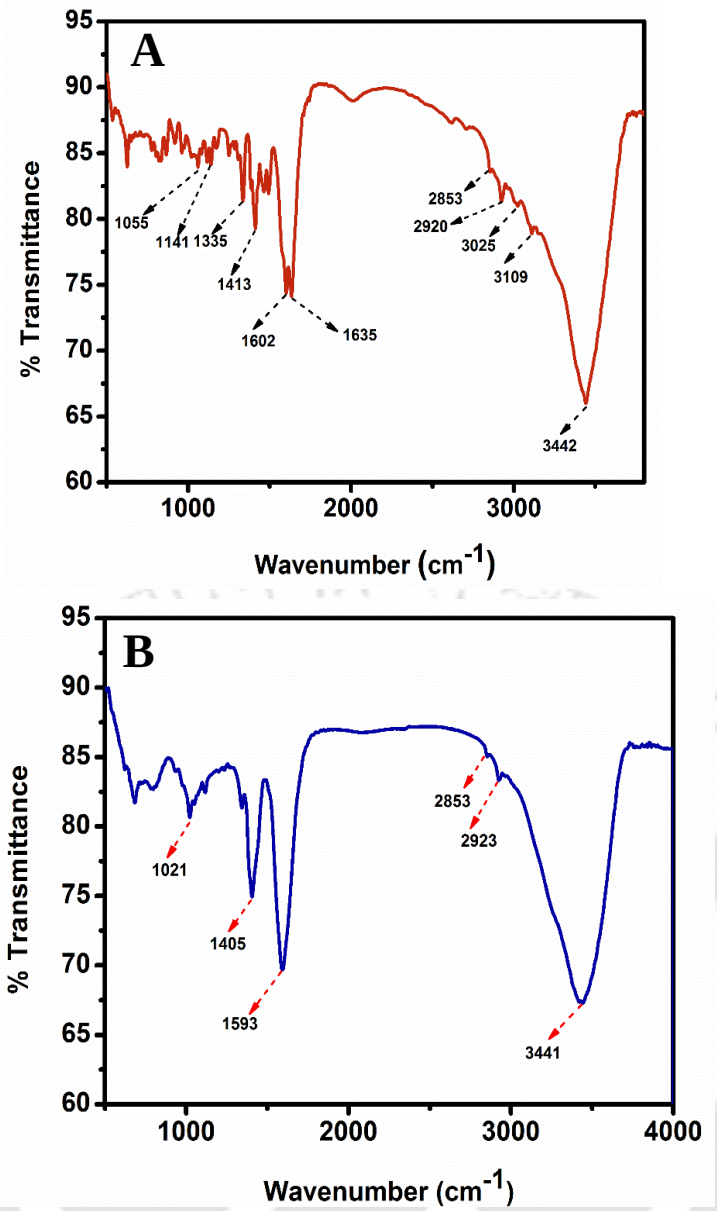

Fig. 3.10 FTIR spectra of (**A**) ligand-stabilized Au_{14} nanoclusters and (**B**) the product of their reaction with zinc acetate ($Au_{14}MPA_7His_5Zn$).

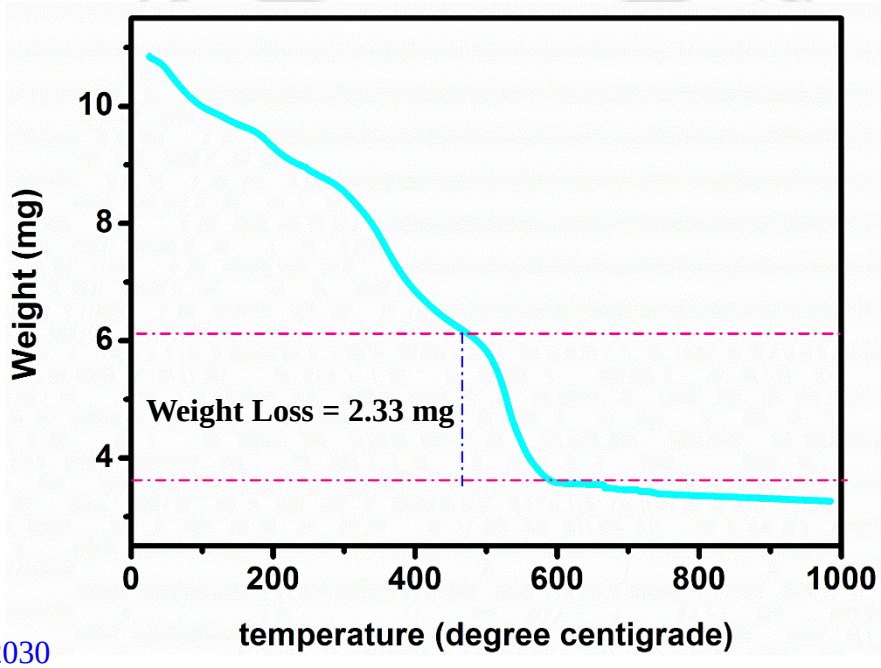

Fig. 3.11 Thermo-gravimetric analysis of the complex ($Au_{14}MPA_7His_5Zn$) produced from the reaction of ligand-stabilized Au_{14} nanoclusters and zinc acetate.

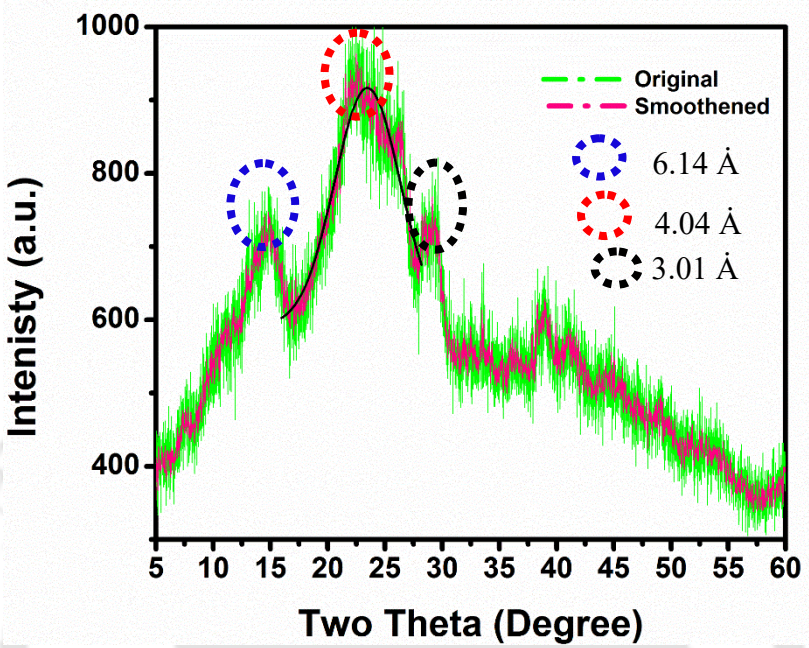

Fig. 3.12 Powder X-ray diffraction pattern of complex ($Au_{14}MPA_7His_5Zn$) produced from the reaction of ligand-stabilized Au_{14} nanoclusters and zinc acetate.

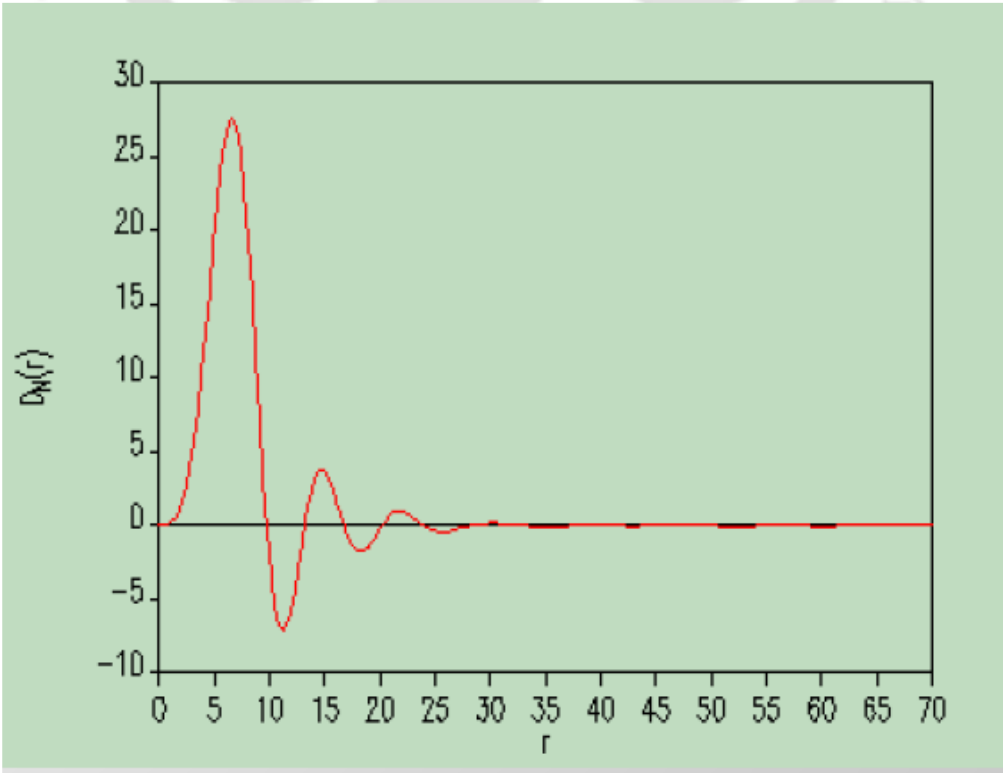

Fig. 3.13 Small angle X-ray scattering of the complex ($Au_{14}MPA_7His_5Zn$) produced from the reaction of ligand-stabilized Au nanoclusters and zinc acetate. Particle size distribution calculated from small angle X-ray scattering of complex ($Au_{14}MPA_7His_5Zn$) produced from reaction of ligand-stabilized Au_{14} nanoclusters and zinc acetate.

The structural analysis of $Au_{14}MPA_7His_5Zn$ based on aforementioned experimental results is as follows:

(a) FTIR:

FTIR spectroscopic analysis revealed that the binding of zinc ion to His might have been through imidazole nitrogen. This is based on the observation that the characteristic peak due to C-N stretching at 1635 cm^{-1} - although present in ligand-stabilized Au_{14} nanoclusters (Fig. 3.10 A) - was absent in $Au_{14}MPA_7His_5Zn$ (Fig. 3.10 B). The stretching frequency (C=C) due to the aromatic ring at 1602 cm^{-1} in the Au nanoclusters was shifted to 1593 cm^{-1} in the case of the complex, possibly due to complexation of the zinc ion with C=N of the same ring. Interestingly, the stretching frequencies corresponding to alkane C-H at 2920 cm^{-1} and 2853 cm^{-1} for ligand stabilized Au_{14} nanoclusters remained nearly unaltered even after complexation. The said observations clearly indicated that the complexation of zinc with His occurred through the imine nitrogen.

(b) TGA:

Thermo-gravimetric analysis (TGA) of the complex (Fig. 3.11) revealed no significant weight loss up to 250 °C. The total content of histidine in the mixture of MPA-His is 50.33% (as evident from MALDI-MS analysis). The decomposition temperature of histidine is reported to be 282 °C. As per the TGA graph (Fig. 3.12), a continuous weight loss occurs from 280 °C (initiated at 264 °C). This loss in mass is assigned to the loss of histidine from the composite mixture of MPA-His. As is evident from the TGA graph, the weight loss is about 55% of the total weight loss (barring the weight loss due to $ZnHis_5MPA_7$). This weight loss, thus, is in close agreement with the composition of histidine in the composite mixture of MPA-His determined from MALDI –TOF analysis. On the other hand, a significant weight

loss (about 38.5 % of the weight present at 480 °C) occurred at a temperature of 529 °C. This may be attributed to loss of $ZnHis_5MPA_7$, which constitutes 36.2 % of the total weight of $Au_{14}MPA_7His_5Zn$. Also, 61.5 % of the amount of sample remained nearly intact up to a temperature of 1000 °C. This mass percentage is in concordance with the mass of Au_{14} out of total mass of $Au_{14}MPA_7His_5Zn$ that is 63 %.

(c) Computational analysis:

The structure of the crystalline complex, as obtained from the electron diffraction and other analyses, was further substantiated by computational modelling using Avogadro. Briefly, in the energy optimized structure (Fig. 3.7 A), the Au_{14} clusters were considered planar with five peripheral Au atoms bonded to five MPA (each MPA being coordinated to a single Au atom). In addition, two peripheral Au atoms were bonded to four His ligands and two MPA ligands (i.e. two His ligands and one MPA ligand being coordinated to each Au atom). One peripheral Au atom was bonded to one His ligand, while two Au atoms remained non-coordinated. Coordination of MPA to constituent Au of gold nanoclusters was likely to be through sulphur atom, owing to the aurophilicity of the latter. Likewise, His was considered to stabilize the clusters through nitrogen atom of the main chain amino group, while nitrogen atom of the side chain imidazole group was involved in ligating the zinc ion. The peripheral Au atom of the nanoclusters constituting the hexagonal unit cell of the crystal structure was bonded to two histidine and one MPA ligands (marked as Au1 and Au3 in Fig. 3.7 B and as in scheme 1 shown below). Each zinc ion was ligated to one of the two His ligands being coordinated to single Au atom and likewise with a His ligand and MPA ligand of other two Au atoms of two different clusters to afford the formation of two connected hexagons, ultimately leading to tri-coordination of both zinc ion and gold atom in the plane.

Interestingly, the distance between zinc ions and nearest (peripheral) Au atom in a trigonal geometry was calculated to be 6.7 Å. This is consistent with the observed electron diffraction pattern (Table 3.2). As a matter of fact, the constituent atoms of Au clusters and zinc ions were positioned in alternate vertices of connected hexagons (in two dimensions) with distances between zinc and a peripheral Au atom in closest proximity, corroborating the electron diffraction data. However, while coordination of zinc ion to three Au atoms (each being a part of individual Au_{14} clusters) defines a trigonal plane (with bond distance of 6.7 Å), extension of crystal structure through the axial dimension was achieved via Au-Au

(marked as Au1 and Au3) moiety of Au_{14} clusters, with His and MPA ligated Au atoms connecting two layers of hexagon and a non-ligated Au atom in between. In this dimension, the interlayer distance of separation was theoretically computed to be 5.0 Å, which is in good agreement with the experimentally obtained value of 4.8 Å (Fig. 3.6 C) from SAED pattern and 5.0 Å from HRTEM analysis (Fig. 3.6 D). Substantial degree of concordance between theoretically computed value and experimentally observed value was achieved (Table 3.3). Moreover, as the two peripheral Au atoms of Au_{14} clusters were involved in forming the edges of hexagon and interconnecting two such layers, the remaining constituents of clusters were positioned perpendicular to the hexagon. One such Au constituent of the clusters (marked 8 in Fig. 3.7 B), at a distance of 6.7 Å from the Au atom defining the edge of each hexagon (marked 1 in Fig. 3B) was situated at the center of the hexagon. This is apparent from SAED pattern (Fig. 3.6 B) which shows that each hexagon possesses a center corresponding to the distance from the edge being equivalent to 6.7 Å. Thus, the distance of 6.7 Å obtained from theoretical optimization matched closely with that of the distance of center to edge of a hexagon in diffraction pattern, thereby justifying the positioning of Au atom of cluster at the center of hexagon in theoretical model (Fig. 3.7 B). Also, as observed from SAED, diffraction spots at every separation of 4.5 $Å^{-1}$ (in reciprocal space, and corresponding to 2.3 Å in real space) are brighter in intensity. The enhanced brightness of such group of spots over others could be explained by the proposition that separation of 4.5 $Å^{-1}$ corresponding to Au – Au distance of 2.5 Å in computationally optimized structure, superimposed with that due to Au – Zn distance of 6.7 Å at an interval of two diffraction spots. Besides, as mentioned above, the Au atom forming the edge of hexagon was coordinated to two His ligands and one MPA ligand. In this regard, the distance between Au and sulphur atom (of MPA) was theoretically calculated to be 2.3 Å; in addition, Au-nitrogen (of His) distance was computed to be 2.0 Å. Thus, diffraction due to Au- sulphur as well as Au – nitrogen appeared symmetrically at every 4.5 $Å^{-1}$ (in reciprocal space and 2.2 Å when converted to distance in real space), along the six-fold axes in the plane constituting the hexagons. This also leads to appearance of diffraction spots with increased intensity at an interval of two diffraction spots with comparatively lower intensity. The corroboration of the experimentally observed distances with that of computationally obtained distances along with the error percentages have been tabulated in Tables 3.2 and 3.3. Additionally, the clusters interlinked the hexagonal layers in alternate fashion thereby maintaining the symmetry of the

structure. In other words, the two hexagonal planes are connected by Au_{14} clusters –which themselves are in a plane perpendicular to the hexagonal planes – and as shown in Fig. 3.7 B

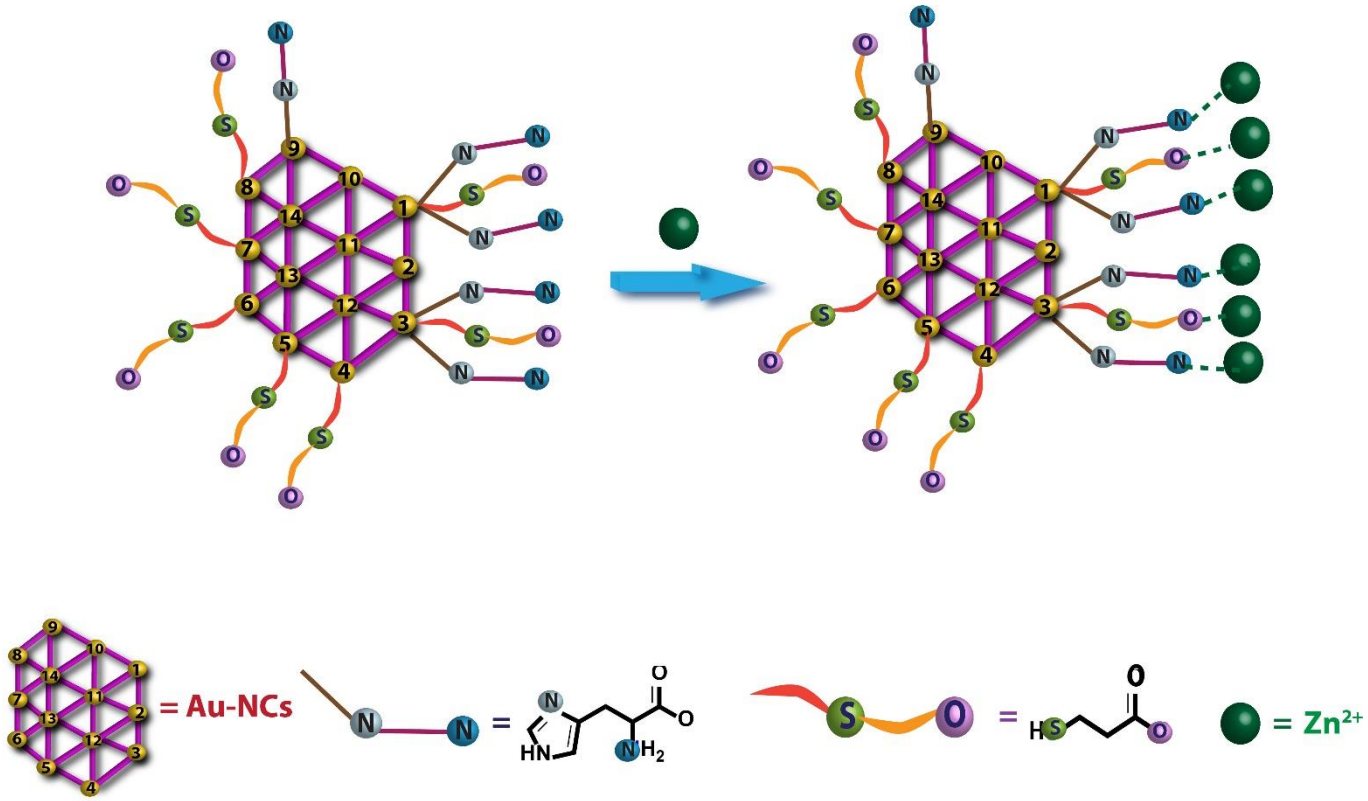

Scheme 1. Schematic representation of complexation reaction between ligand stabilized (MPA and His) gold nanoclusters and zinc ions. Each zinc ion in the complex is a part of a hexagon.

Table 3.2 Highlights of the distances between the mentioned co-ordinates (1-6 are the vertices of the first hexagon from the centre while 7-12 are the vertices of the third hexagon form the centre) of the electron diffraction pattern (Fig. 3.6 B) and in the theoretical model (Fig. 3.7 A) corroborating the electron diffraction pattern. *Rounded off to appropriate significant figures. The error percentage between observed and calculated distance is 3.5%. The average distance among coordinates of 7 – 12 forming a hexagon is 2.2 Å. whereas, the

distances between the coordinates between Au1 – N1, N11, S1; Au2 – N2, N22, S2 and Au3-N3, N33 and S3 is 2.1 Å. The error percentage between observed and computed distance is 4.5 %.

Co - ordinates	Optimised Distances (Å)*	Co - ordinates	Observed Distances (Å)*
Au1 – Zn1	6.6	1-2	6.3
Zn1 - Au3	6.3	2-3	6.2
Au3 – Zn3	7.7	3-4	7.3
Zn3 – Au 2	6.9	4-5	6.9
Au2 – Zn2	6.5	5-6	6.8
Zn2 – Au 1	6.6	6-1	6.9
Au1 – N1	2.0	7 - 8	2.2
Au1 – N11	1.95	8 - 9	2.2
Au1 – S1	2.3	9 - 10	2.2
Au2 – S2	2.35	10 - 11	2.2
Au2 – N2	2.0	11 - 12	2.2
Au2 – N22	2.0	12 - 7	2.2
Au3 – N3	2.0		
Au3 – N33	2.0		
Au3 – S3	2.35		

Table 3.3 Highlights of the distances between the mentioned co-ordinates in the electron diffraction pattern (1 and 2 refers to the vertical distance between two diffraction spots) and in the theoretical model (Fig. 3.7 A) corroborating the electron diffraction pattern. The error percentage in this dimension is 4 %.

Co - ordinates	Optimised Distances (Å)	Co - ordinates	Observed Distances (Å)
Au2 – Au22	5.0	1 - 2	4.8

Further, considering the reactivity of the peripheral atoms of gold clusters, the newly made complex was tested for its capacity for hydrogen storage. The hydrogen adsorption capacity of the complex was determined to be 0.244 mM per gram at 20 bar pressure and 20 ˚C (Fig. 3.14 A). Interestingly, hydrogen adsorption within the complex was accompanied with quenching of luminescence of the constituent clusters, which eventually was restored upon desorption of hydrogen (Fig. 3.14 B). The cluster complex was observed to be devoid of well-defined pores (as suggested from surface area and pore size analyses, Table 3.2), thereby indicating that interaction of hydrogen molecule occurred possibly through the constituent Au atoms of the clusters within the complex. As per theoretical investigation, the edge atoms of gold clusters support facile hydrogen dissociation.[59] In the computational structure of the complex suggested above, two of the peripheral Au atoms remained non-ligated (marked as 2 and 4 in Fig. 3.7 B) among which Au atom marked 4 is the site potent of accommodating the dissociation of hydrogen, while Au atom marked 2 may not favour such reaction owing to steric hindrance. The proposed reaction and hydrogenated structure is concurrent with the observation that 1:1 stoichiometric reaction occurred between each cluster and hydrogen molecule. Thus 0.231 mM clusters in the crystalline complex (concentration of the clusters in the solid) reacted with 0.244 mM H_2 at 20 °C and 20 bar. The desorption of hydrogen from the crystalline complex was also confirmed from gas chromatography measurement, which consisted of a sharp characteristic signal of hydrogen (Fig. 3.14C). The release of hydrogen from gas

chromatography has been correlated with desorption isotherm (Fig. 3.14A). As per gas chromatography results, the amount of hydrogen release has been quantified to be 0.035 mM/g, which demonstrates a fair degree of concordance with the quantity of hydrogen released (0.054 mM/g) as measured from the desorption isotherm.

In a typical experiment, 75 mg of crystalline compound was placed in a conical flask (65 mL). The opening of the conical flask was covered with parafilm and a balloon containing hydrogen was inserted into the flask using a syringe needle. The pressure thus was approximately 1 atmosphere. After 1 h, the conical flask was deaerated by purging nitrogen for 5 min and the opening of the flask was sealed again. After 5 min, the gas within the flask was collected by a syringe. The collected gas was injected into the gas chromatograph. A sharp signal due to hydrogen was obtained. The amount of hydrogen gas was quantified in terms of volume percent normalized to the standard hydrogen gas using the gas chromatograph.

Volume % of hydrogen obtained = 0.101%

Volume of conical flask = 65 mL

Thus volume of hydrogen gas injected = 0.065 mL

Assuming ideal behavior of hydrogen gas and employing ideal gas equation to find the number of moles of hydrogen gas injected = 0.0026866 mmol

Amount of crystalline complex subjected to hydrogen adsorption = 75 mg

Thus, amount of hydrogen gas evolved per gram of complex = 0.035 mmol/g

From the adsorption-desorption isotherm, the amount of hydrogen gas released at 1 atmosphere pressure (i.e 1.013 bar) = 0.054 mmol/g

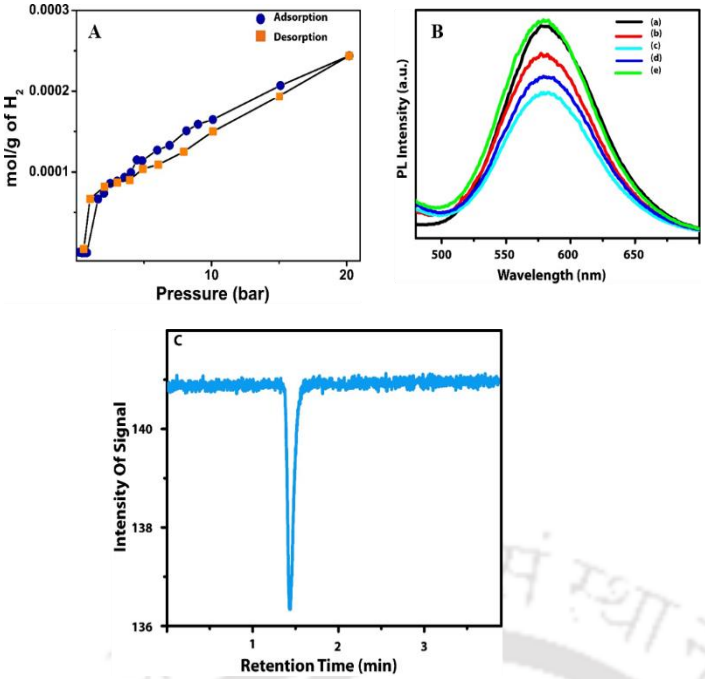

Fig. 3.14 (**A**) (a) Adsorption and (b) desorption isotherms of hydrogen on zinc added Au_{14} nanoclusters. (**B**) Photoluminescence spectra of (a) zinc added Au_{14} nanoclusters, (b)-(c) hydrogen purged crystalline complex, (d) - (e) of the hydrogenated complex upon reduction of hydrogen pressure within the cuvette containing the complex. The measurements were made using dispersion of the crystalline complex in hexane. (C) Signal due to release of gaseous hydrogen from the crystalline complex as measured using gas chromatography. The measurement was done using dispersion of crystalline complex in water.

3.3 Conclusion

In brief, the formation of a crystalline inorganic complex involving Zn^{2+} ions and ligand-stabilized Au_{14} nanoclusters has been reported for the first time, based on a complexation reaction in aqueous medium. The structure of the crystal thus formed was established by analytical investigations, which was corroborated by the structure of the complex obtained from computational analysis. A three-dimensional structure positioning alternate gold atoms (belonging to the Au_{14} cluster moiety) and zinc ions in the vertices of a regular hexagon has been proposed. The complex so formed exhibited superior optical property in comparison to the component nanoclusters. Additionally, the new material was not only able to store hydrogen to a limit of 0.244 mM per gram of the complex at room temperature but also served as a self-indicator for the process of hydrogen adsorption and desorption, by virtue of the intrinsic photoluminescence property of nanoclusters. The observation of facile room

temperature hydrogen storage and recovery by the inorganic complex made of Au nanoclusters calls for further investigations to increase the capacity and versatility of storage and recovery of other gases for numerous practical applications. Also, it is important to note that our findings led to a new concept of nanocluster crystallization via assembly following complexation reaction, employing metal ions and the ligands on nanoclusters, which may spawn the emergence of rich chemistry involving the noble metal nanoclusters.

Chapter 4

Zinc Coordinated Hierarchical Organization of Ligand Stabilized Gold Nanoclusters for Chiral Recognition Supplemented with Separation

Three dimensional organization of D or L tryptophan and mercaptopropionic acid stabilized gold nanoclusters has been achieved by complexation reaction involving the ligands stabilizing gold nanoclusters and zinc ions. Powder X ray diffraction and transmission electron microscopy analyses substantiated the crystalline nature of the assembly of atomic nanoclusters. The hierarchical arrangement of the nanoclusters exhibited superior optical properties (namely, enhanced photoluminescence and excited state lifetime) as compared to the non-assembled nanoclusters. Further, photoluminescence of the crystalline assembly of nanoclusters served as a visual marker for chiral recognition of D and L enantiomers of tryptophan with concurrent separation of the corresponding enantiomer. A theoretical structure based on various experimental observations has also been proposed herein. The mechanistic aspect of chiral recognition supplemented separation has been proposed to have occurred through attachment of D and L tryptophan to the coordinatively unsaturated zinc ions thus forming super complexes, the degree of stabilization of the super complex being dictated by "three-point versus two-point interaction" between the enantiomers and the chiral selector.

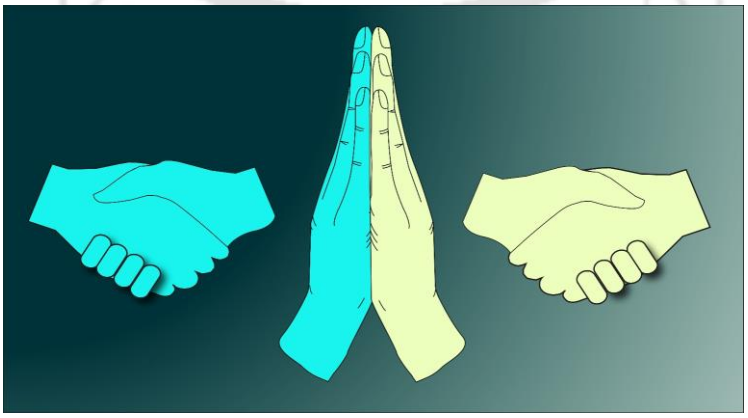

4.1 Experimental Section

Synthesis of gold nanoclusters (Au NCs):

1 mL of $HAuCl_4$ was added to 10 mL methanol followed by 0.4 mL MPA. The solution was stirred till the yellowish tinge of $HAuCl_4$ disappeared. The resultant mixture was added with ~10.0 mg D tryptophan (Aldrich) and stirred for 10 min. The dispersion thus formed was centrifuged at a speed of 10,000 rpm for 10 min. The pellet was thereafter re-dispersed in 1 mL water. Similar protocol was followed for synthesis of L tryptophan stabilized Au NCs by adding analogous amount of L tryptophan as discussed in case of D tryptophan.

Synthesis of gold nanocluster complex (Zn-Au-NCs):

The pellet obtained following centrifugation of D (or L) tryptophan stabilized Au NCs was dispersed in 1 mL water. The dispersion was added with ~50 mg of zinc acetate dihydrate. This led formation of a dispersion with higher photoluminescnece intensity. The dispersion was centrifuged at a speed of 10,000 rpm for 10 min. The pellet was then redispersed in 1 mL water and used for further experiments.

Experimental details of photoluminescence based chiral sensing of D and L tryptophan:

500 μL of Zn-Au-NCs (prepared by the protocol discussed above) was diluted with 2.0 mL water (total volume equal to 2.5 mL). To this solution sequential amount of D and L tryptophan were added sequentially (as mentioned in figure legends).

4.2 Results and discusssions

Firstly, photoluminescent Au nanoclusters, exhibiting emission maximum at 595 nm, were synthesized in methanol, using mercaptopropionic acid (MPA) and D tryptophan as the stabilizers (Fig. 4.1 and 4.2). The observed molecular ion peak in electrospray ionization mass spectrometry (ESI-MS) has been attributed to the formation of $Au_{14}MPA_6Trp_4$, the ionized form of which was observed as $[Au_{14}MPA_6Trp_4 + 3Na+]^{3+}$(Fig. 4.3). Further, a computed mass spectrum, in accordance with the proposed formula, has been found to be in concordance with the experimental observation.

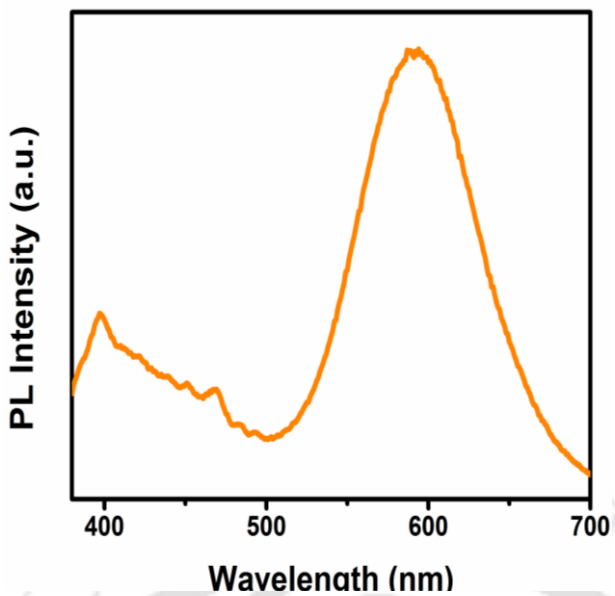

Fig. 4.1 Photoluminescence emission spectrum of ligand stabilized Au nanoclusters. The excitation wavelength was set at 350 nm.

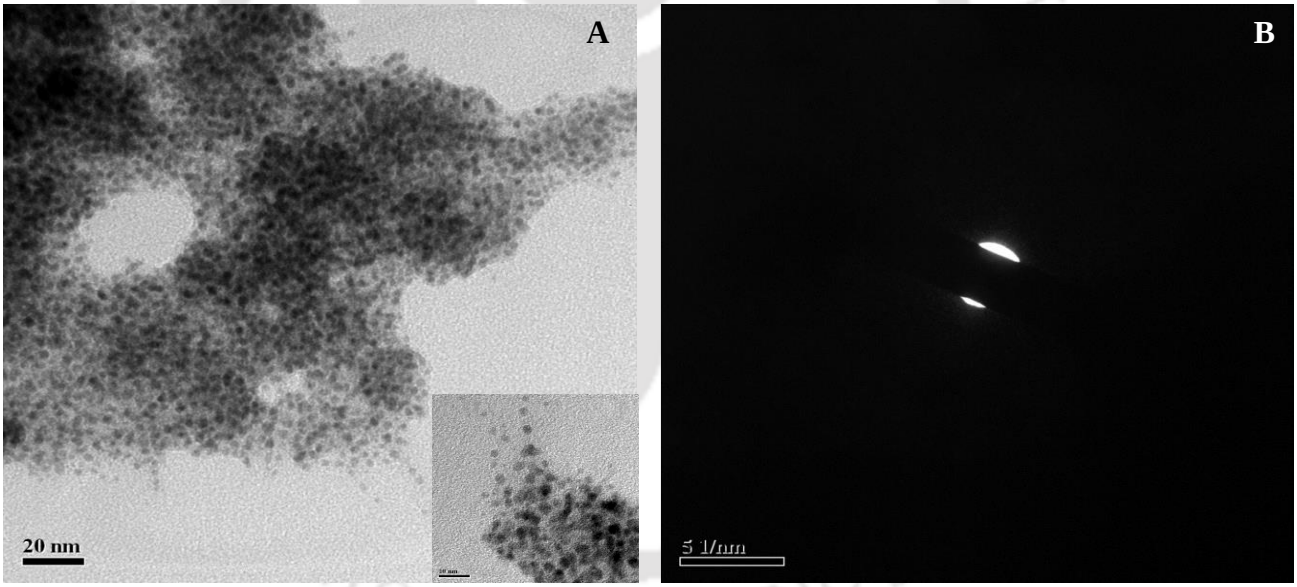

Fig. 4.2 (A) Transmission electron microscopy (TEM) image of D tryptophan stabilized Au nanoclusters revealing aggregation induced by methanol upon evaporation. The inset shows the presence of D tryptophan stabilized Au nanoclusters in the scale range of 10 nm. (B) Selected area electron diffraction (SAED) of the particle shown in (A).

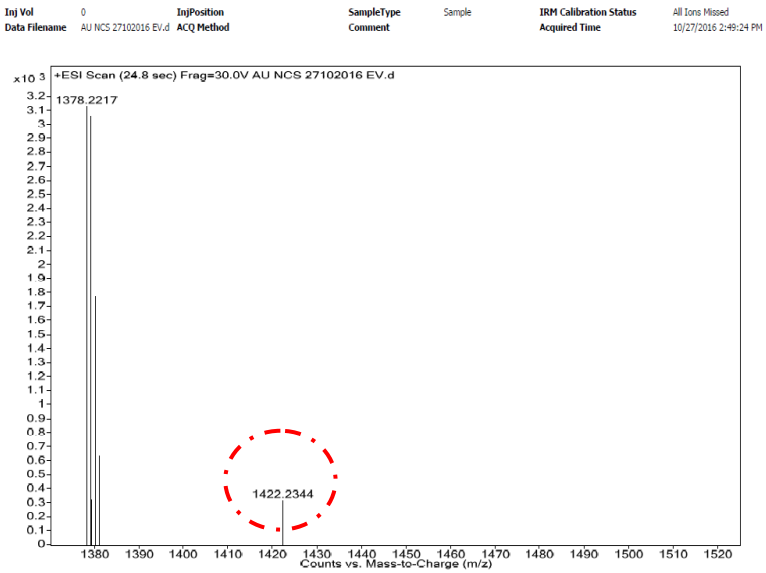

Fig. 4.3 Electrospray ionization (ESI) mass spectrum of D tryptophan stabilized Au nanoclusters. The theoretical mass, as simulated, has been observed to be 1422.9446, which is consistent with the observed value of 1422.2344.

Complexation reaction between D tryptophan and MPA stabilized Au nanoclusters and Zn^{2+} ion was pursued following addition of zinc acetate to the nanocluster dispersion at room temperature. The photoluminescence intensity due to Au nanoclusters was significantly enhanced following addition of the zinc ions (Fig. 4.4 A). The enhancement in photoluminescence of the clusters is attributed to the structural rigidity imposed upon the ligand-stabilized nanoclusters following complexation with zinc ions. This restricts the non-radiative decay channel and in turn facilitates decay through radiative channel, owing to restricted intramolecular motion (RIM). The attainment of rigidity in the overall structure leads to consequential enhancement in emission quantum yield of the complex in comparison with ligand-stabilized nanoclusters. The complexation constant associated with the reaction was calculated to be $(1.32 \pm 0.32) \times 10^5$ M^{-1} (Figure 4.4 B-C). Moreover, the photoluminescence lifetime of the clusters showed significant enhancement following addition of zinc ions. Time-resolved photoluminescence analysis revealed that the lifetime of the major component changed from 248 ns to 1.37 μs following addition of Zn^{2+} ions to the clusters (Figure 4.4 D-E). Thus, the results from the photoluminescence studies clearly indicated significant alteration of the emission characteristics of the Au nanoclusters in the presence of Zn^{2+} ions.

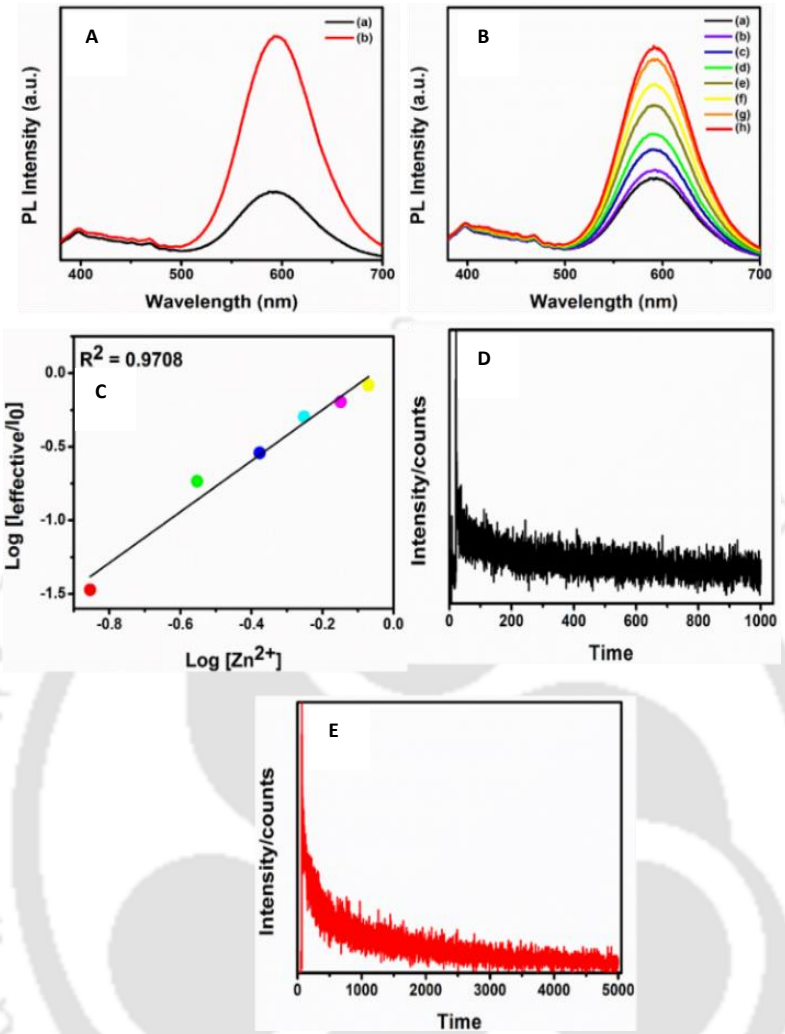

Fig. 4.4 (A) Photoluminescence emission spectra of (a) ligand stabilized Au nanoclusters and (b) zinc salt added to Au nanoclusters upon excitation at 350 nm. (B) Photoluminescence emission spectra of (a) Au nanoclusters following addition of (b) 2 µL, (c) 4 µL, (d) 6 µL, (e) 8 µL, (f) 10 µL, (g) 12 µL and (h) 14 µL of 228 mM zinc salt. (C) Plot of Log [$I_{effective}/I_0$] as a function of Log [Zn^{2+}] based on the spectra shown in (B). Time resolved photoluminescence spectra of (D) ligand stabilized Au nanoclusters and (E) zinc added Au nanoclusters.

X-ray diffraction (XRD) pattern of the powder sample of the precipitate obtained after centrifugation marked the presence of major peaks at 2θ = 12.56˚, 25.06˚, 28.36˚ and 50.53˚. XRD patterns of the control samples, which included ligand stabilized Au nanoclusters and mixture of D tryptophan, MPA and Zn-acetate, did not exhibit any discernible peak (Figure 4.5 A), thus discounting direct contributions of the components in the observed XRD pattern.

Further, in order to solve the crystal structure of the product, "Divcol/Treor crystal structure solution" was employed using Full Prof Suite, which revealed that the product had crystallized in tetragonal geometry with lattice parameters of a = b = 7.847957 Å, c= 7.10318 Å and α = β = γ = 90˚. The lattice parameters obtained from the aforementioned 'structure solution' was associated with the highest figure of merit. Moreover, the XRD pattern has been fitted, using the lattice parameters and space group obtained from 'Treor solution', by employing "Le-Bail profile fitting" (Figure 4.5 B). The product crystallized with a space group of P4/mmm corresponding to point group of D_4h. Thus the results indicated that the 'reaction' between $Au_{14}MPA_6Trp_4$ and Zn^{2+} resulted in the formation of crystalline assembly of the constituents, possibly without affecting the basic structure of the ligand-stabilized cluster.

The structure of the crystalline product was further corroborated from high resolution transmission electron microscopy (HRTEM) and selected area electron diffraction (SAED) analyses. HRTEM study revealed the lattice spacing in the crystalline product to be 5.6 Å, which corresponds to interplanar distance between zinc ion and Au nanocluster, as per three dimensional structure designed according to the lattice parameters and space group obtained from XRD study (Figure 4.5 C-D). SAED analysis on such a crystalline particle showed rectangular arrangement of the constituents of the crystalline product complex (in consonance with the geometry obtained from XRD analysis) with distances between the plane of diffracting centres as ~5.6 Å and ~10.1 Å (Figure 4.5 E). This distance of 10.1 Å closely matches with the separation of the planes (passing through the face diagonal) containing the clusters positioned within the body of the tetragon (~11 Å) being constructed with lattice parameters - obtained from XRD study - as sides of the tetragon.

Computational modelling, based on 'Avogadro', further corroborated the experimentally obtained structure of the crystalline assembly. The results shown in (Fig. 4.5 F) indicated coordinate bonding of Zn^{2+} with tryptophan and MPA via the carboxylate groups. Literature reports suggest that one of the stable forms of Au_{14} clusters could correspond to a "cage-like structure", which possesses a D_4h symmetry.[60] A representative image is shown in scheme 1. Based on the symmetry of the assembly obtained from XRD analysis, the said structure of Au_{14} clusters has been adopted for further analysis. Tryptophan and MPA were positioned symmetrically onto the Au atoms of the cage-like Au_{14} clusters (scheme 1). Interestingly, the distances corresponding to the unit cell lattice parameters, as

obtained from the computational analysis, were in close agreement with those observed in XRD analysis. Distances between zinc ions along X and Y axes (each being ligated to gold atoms by MPA and tryptophan separately) of the unit cell has been observed to 13.7 Å and 12.7 Å (for a particular conformation of the ligands). The values are close to the dimension of the body diagonal of a tetragon formed with zinc ions positioned at the corners and the clusters positioned approximately at the centre of the tetragon with lattice parameters obtained from XRD pattern of Zn-Au-NCs. The lattice parameter corresponding to 7.1 Å has been proposed to be achieved through periodic placing of MPA at the central gold atoms of the conjoint rectangular faces of the gold clusters. A representative structure of the crystalline assembly based on experimental and computational evidences is depicted in Figure 4.5 G.

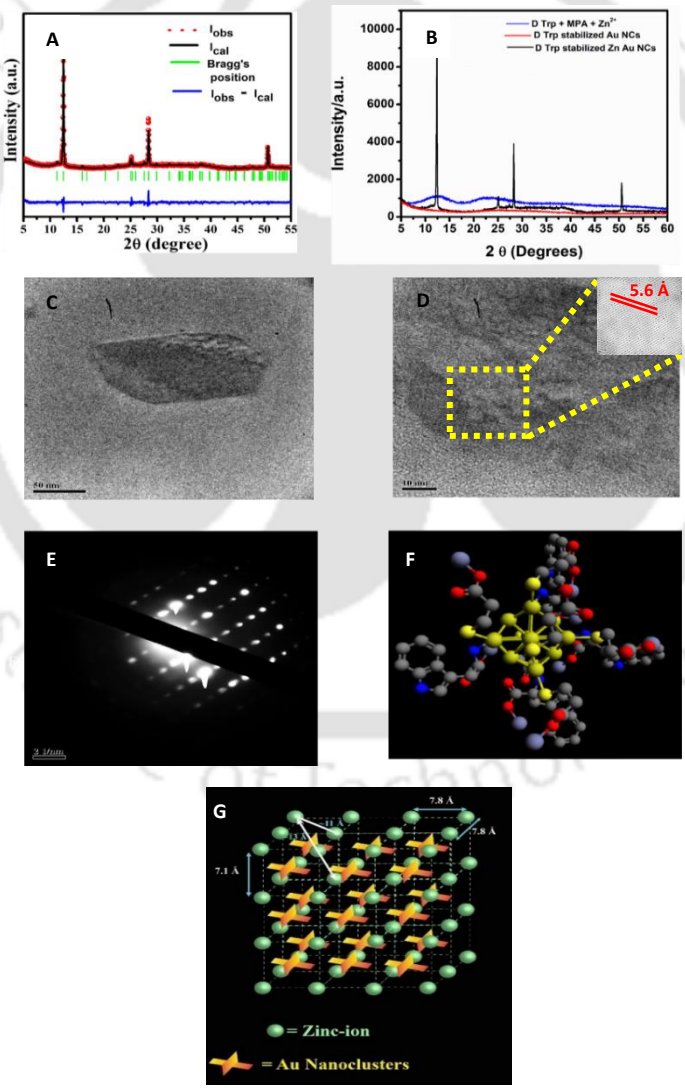

Fig. 4.5 (A) X-Ray diffraction (XRD) pattern of crystalline complex of zinc added Au nanoclusters, only ligand stabilized Au nanoclusters and a mixture of zinc added to tryptophan and MPA. (B) Rietveld refinement of XRD pattern of the product of reaction between Au nanoclusters and zinc ions. (C) TEM image of the crystalline complex of zinc added Au nanoclusters. (D) High resolution TEM image of crystalline complex shown in (C). (E) Typical selected area electron diffraction (SAED) pattern of the crystalline complex. (F) Computationally optimized structure based on the distances obtained from (B). (G) A representative structure of the crystalline complex of zinc ions and Au nanoclusters.

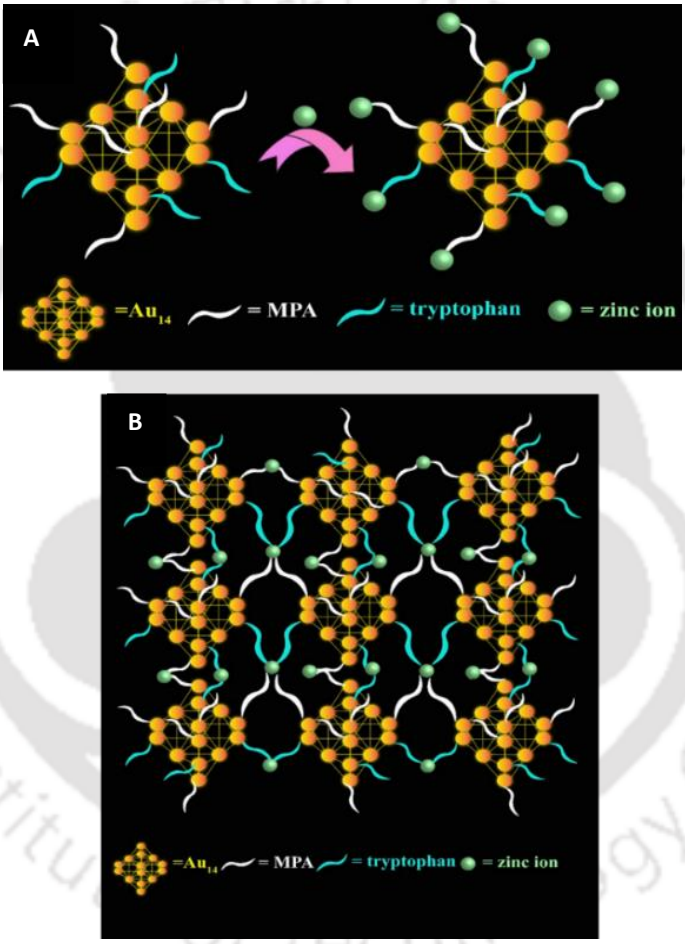

Scheme 1: Schematic representation of (A) the structure of D tryptophan and MPA stabilized Au nanoclusters prior to and following complexation with zinc ions. (B) The three dimensional network formed by Zinc and Au nanoclusters.

FTIR spectroscopic investigations further revealed possible mode of bonding between Zn^{2+} and the ligand-stabilized Au_{14} clusters. The results indicated that the bonding of Zn^{2+} might have occurred through carboxylate groups of MPA and tryptophan. This is evident

from the observation that while the peak due to asymmetric stretching of carboxylate group of tryptophan appeared at 1624 cm^{-1} in the spectrum of tryptophan stabilized Au nanoclusters, the same appeared at 1543 cm^{-1} for Zn-Au-NCs (Fig. 4.6 A-B). Similarly, the peak due to C-O stretching of carboxylate group of MPA at 1693 cm^{-1} in Au nanoclusters appeared at a lower stretching frequency (1582 cm^{-1}) in the product of reaction between Au nanoclusters and Zn^{2+} ions.

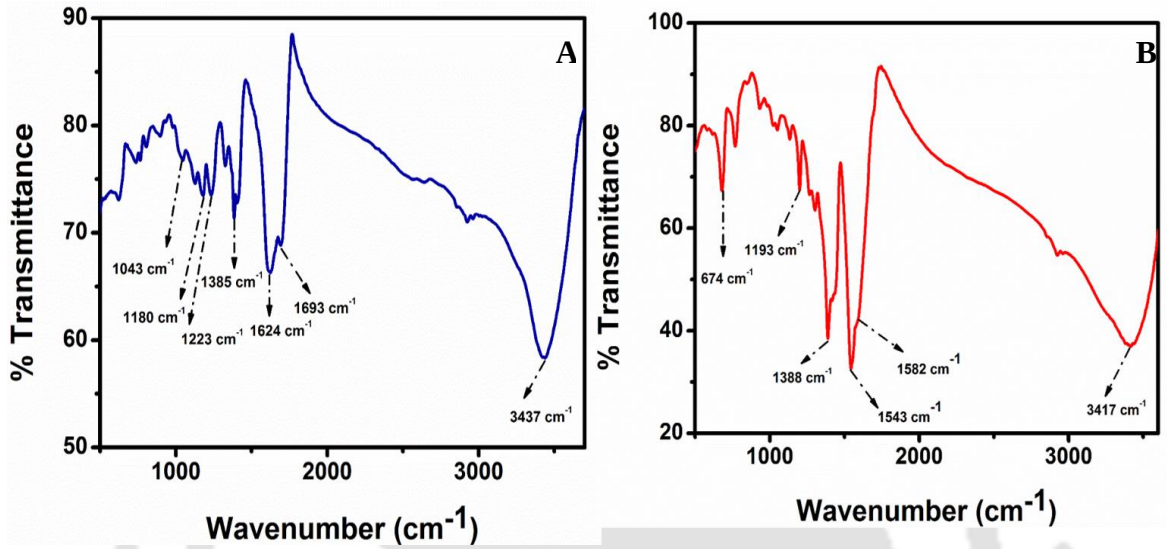

Fig. 4.6 Fourier transform infrared (FTIR) spectra of (A) D tryptophan stabilized Au nanoclusters and (B) D tryptophan stabilized Zn-Au-NCs.

Since the self-assembled nanostructure consisted of D tryptophan, it was deemed fit to test its efficiency in the chiral recognition of D and L tryptophan. Also, the intrinsic photoluminescence of Zn-Au-NCs could serve as a visual sensor for the chiral recognition of enantiomers of D and L tryptophan. It was observed that while the luminescence of D tryptophan stabilized Zn-Au-NCs was quenched significantly (24.7 %) in the presence of externally added D tryptophan, the same was quenched to a lesser extent (7.3 %) in presence of L tryptophan (Figure 4.7 A-B). As mentioned above, the enhanced photoluminescence of the zinc complex of gold nanoclusters could be attributed to the structural rigidity attained by the clusters following complexation with zinc. Also, it has been stated in the subsequent section that the recognition of appropriate enantiomer of tryptophan by the complex is due to coordination of the former with zinc ion present in the complex. Upon coordination of zinc with carboxylate group of externally added tryptophan, the structure of the otherwise rigid crystalline complex attains certain degree of flexibility owing to introduction of an additional

analyte in the crystal lattice. This in turn promotes non-radiative decay of the emitting complex causing consequential quenching of the same. The detection limit associated with the recognition technique has been quantified to be 1.44 mM. Analogous results were obtained when L tryptophan stabilized Zn-Au-NCs were treated with D and L tryptophan (Figure 4.8 A-B). In this case, the photoluminescence got quenched to a greater extent upon addition of L tryptophan (22.9%) than D tryptophan (10.5 %). To verify the critical role of assembled nanoclusters in chiral recognition, similar experiments were performed with the as-synthesized ligand-stabilized Au nanoclusters. Interestingly, their photoluminescence was barely affected by either enantiomers of tryptophan (Figure 4.9 A-D). Importantly, the results were similar irrespective of the chiral nature of the stabilizing tryptophan.

Chiral recognition of D and L tryptophan was further affirmed from circular dichroism (CD) measurements. This was pursued by addition of zinc complex of ligand stabilized Au nanoclusters to a solution of a particular enantiomer of tryptophan. Thus, while the ellipticity of L tryptophan got lowered to a lesser extent (6.14 %) upon addition of D tryptophan stabilized Zn-Au-NCs, the ellipticity of D tryptophan was more pronouncedly affected (lowered by 10.11 %) upon addition of the same (Figure 4.7 C-D). On the other hand, the ellipticity of the CD peak corresponding to L tryptophan showed a greater degree (46.98%) of lowering upon interaction with L tryptophan stabilized Zn-Au-NCs while the ellipticity of D tryptophan was decreased by a lesser factor (27.10%) upon interaction with the same (Figure 4.10 A-B). Further, given the micro heterogeneous nature of Zn-Au-NCs, the possibility of chiral separation supplementing recognition was deemed practical. The said objective was pursued following addition of D tryptophan stabilized Zn-Au-NCs to a mixture of D tryptophan and L tryptophan (in the ratio of 80:20) and monitoring consequential changes in the ellipticity of the CD peak of the latter. In consonance with the above observations, the ellipticity of CD peak of D tryptophan and L tryptophan mixture in the said proportion got lowered owing to interaction of D tryptophan with D tryptophan stabilized Zn-Au NCs. The attachment of D tryptophan was further confirmed by recording CD spectrum of the supernatant of the mixture following centrifugation. The ellipticity of the CD peak of the supernatant was the same as that of the mixture before centrifugation (Figure 4.7 E). This indicated that the alteration in ellipticity of CD peak of D tryptophan upon interaction with D and L tryptophan could be attributed to preferential attachment of molecule with same chirality as the stabilizer of the Zn-Au-NCs.

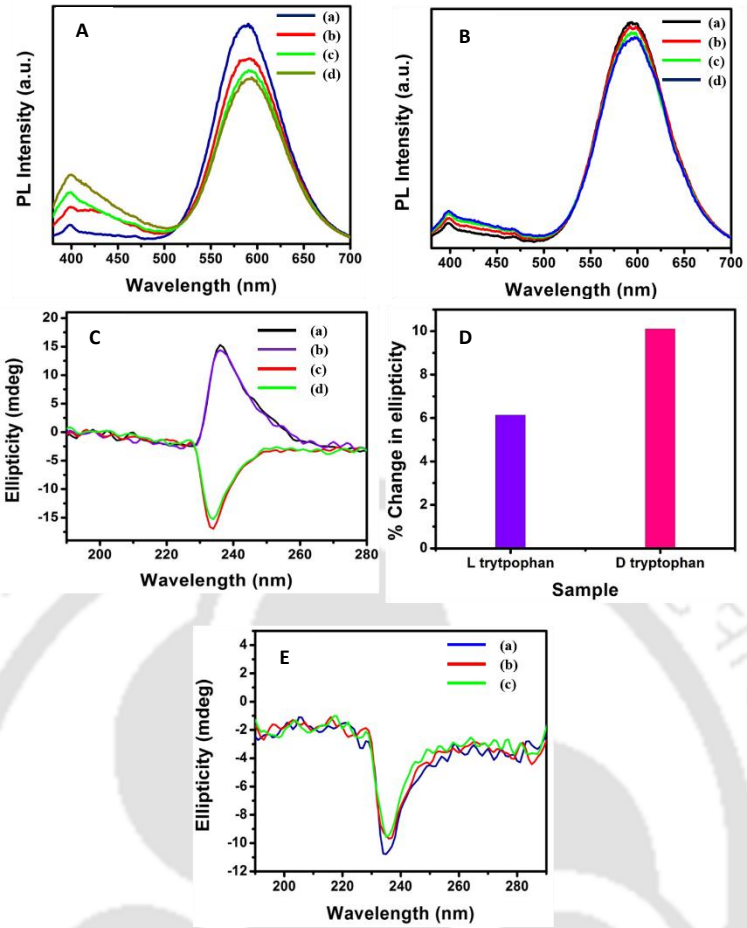

Fig. 4.7 (A) Photoluminescence spectra of (a) zinc complex of D tryptophan stabilized Au nanoclusters and following addition of (b) 100 µL, (c) 200 µL and (d) 300 µL of D tryptophan. (B) Photoluminescence spectra of (a) zinc complex of D tryptophan stabilized Au nanoclusters and following addition of (b) 100 µL, (c) 200 µL and (d) 300 µL of L tryptophan. (C) Circular dichroism spectra of (a) L tryptophan and following addition of (b) 100 µL zinc complex of D tryptophan stabilized Au nanoclusters, (c) D tryptophan and following addition of (d) 100 µL zinc complex of D tryptophan stabilized Au nanoclusters. (D) Bar diagram showing percentage change in ellipticity of D and L tryptophan upon interaction with zinc complex of D tryptophan stabilized Au NCs. (E) Circular dichroism spectra of (a) a mixture of D tryptophan and L tryptophan at a ratio of 80:20, following addition of (b) 100 µL of zinc complex of D tryptophan stabilized Au NCs and (c) the supernatant following centrifugation of the dispersion obtained in (b).

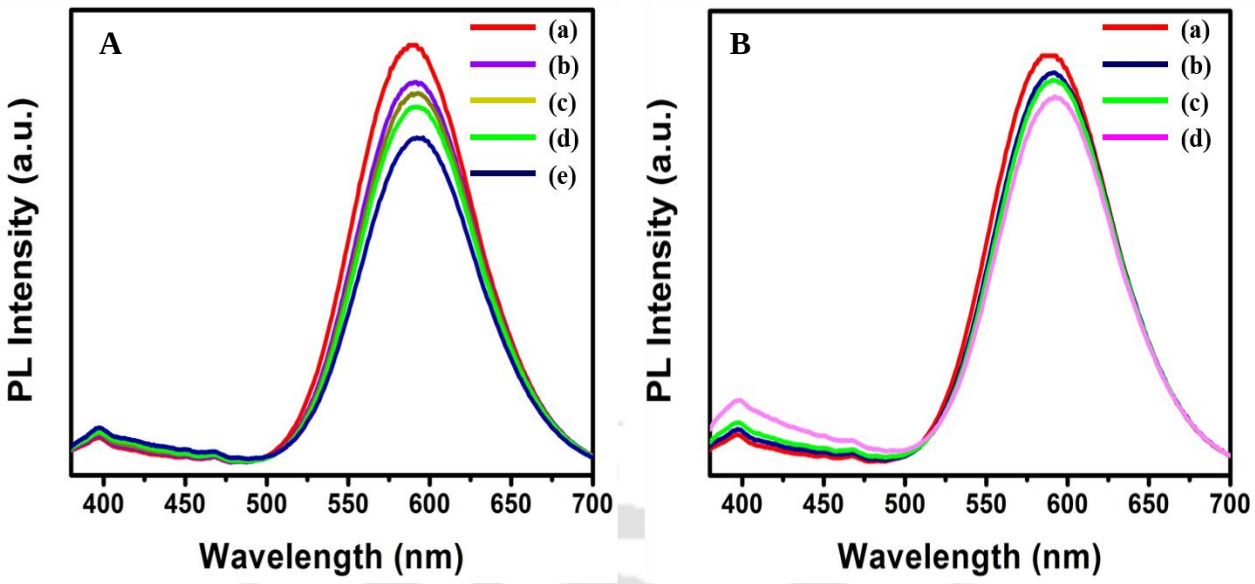

Fig. 4.8 (A) Photoluminescence spectrum of (a) zinc complex of L tryptophan stabilized Au nanoclusters and that following addition of (b) 100 µL, (c) 200 µL and (d) 300 µL of L tryptophan (5.1 mg/mL) and then following further addition of (e) 100 µL of L tryptophan (9.6 mg/mL). (B) Photoluminescence spectrum of (a) zinc complex of L tryptophan stabilized Au nanoclusters and that following addition of (b) 100 µL, (c) 200 µL of D tryptophan (5.2 mg/mL) and then following further addition of (d) 100 µL of D tryptophan (9.7 mg/mL).

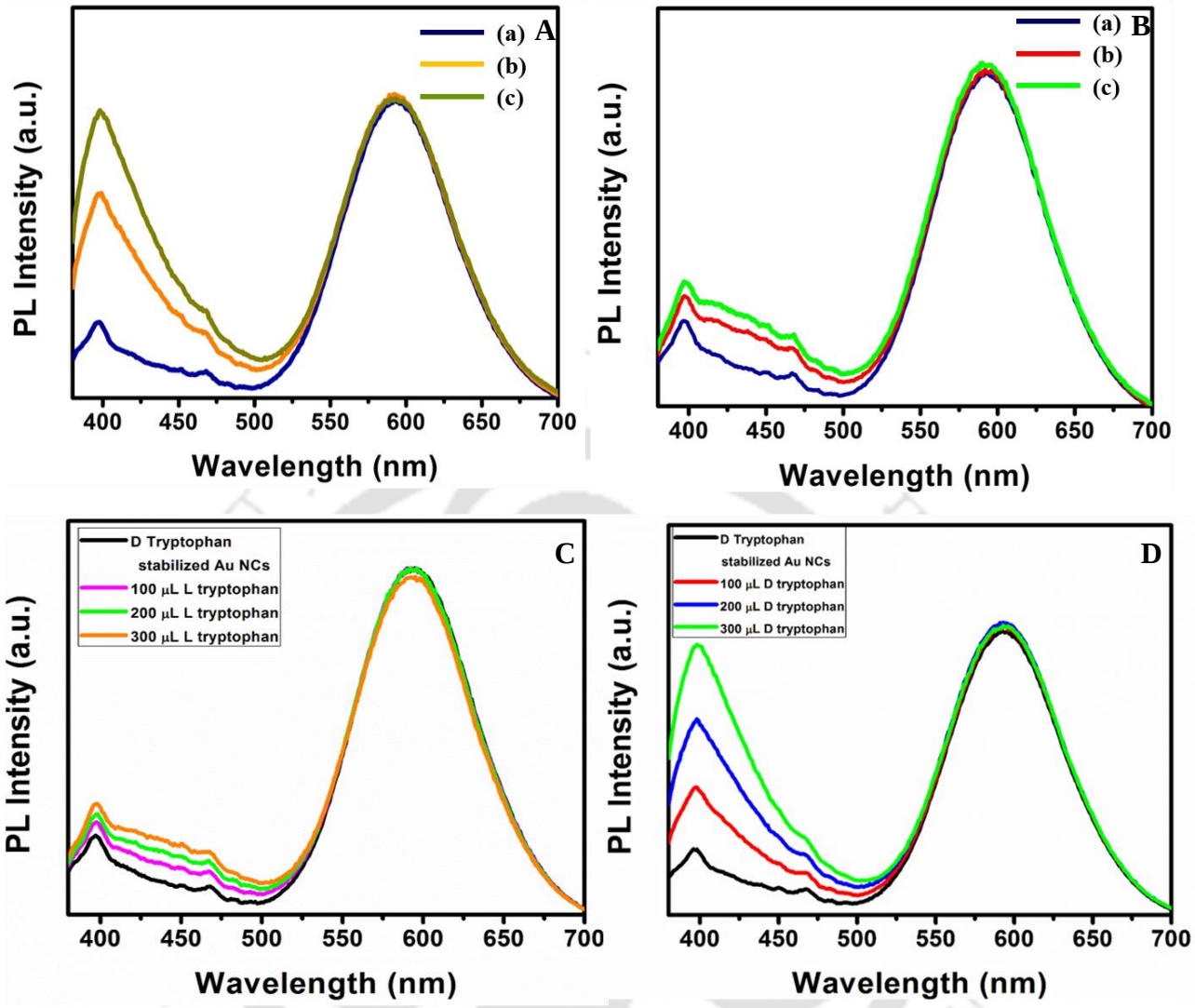

Fig. 4.9 (A) Photoluminescence spectrum of (a) L tryptophan stabilized Au nanoclusters, and the same following addition of (b) 200 µL and (c) 300 µL of D tryptophan. (B) Photoluminescence spectrum of (a) L tryptophan stabilized Au nanoclusters, and the same following addition of (b) 200 µL and (c) 300 µL of L tryptophan. (C) Photoluminescence spectra of D tryptophan stabilized Au nanoclusters following addition of 100 µL, 200 µL and 300 µL of L tryptophan. (D) Photoluminescence spectra of D tryptophan stabilized Au nanoclusters following addition of 100 µL, 200 µL and 300 µL of D tryptophan.

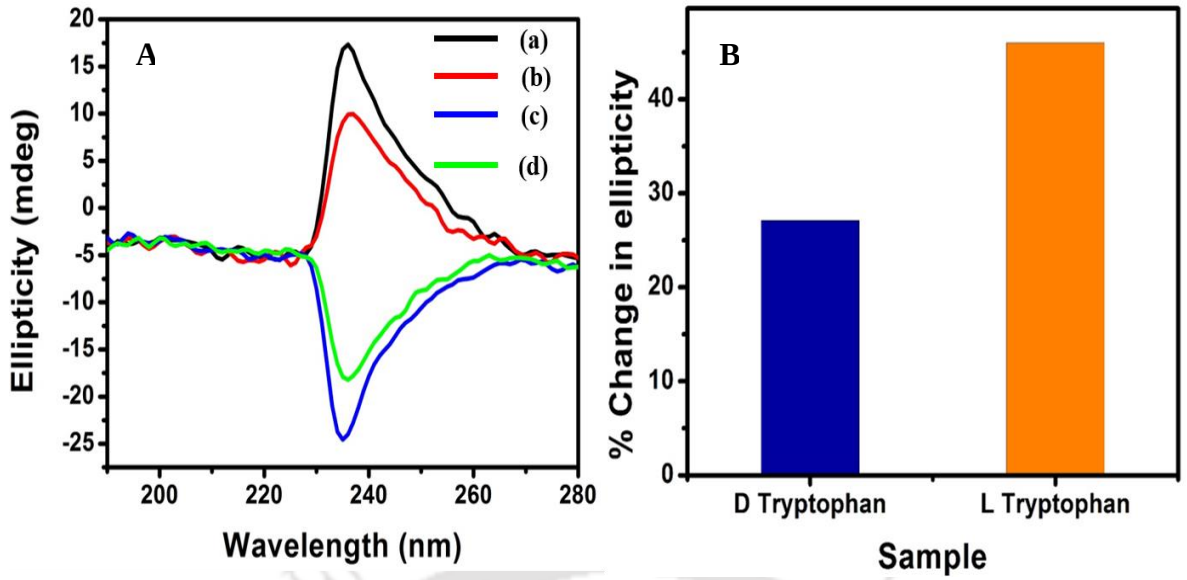

Fig. 4.10 (A) Circular dichroism spectrum of (a) L tryptophan and that following addition of (b) 200 µL zinc complex of L tryptophan stabilized Au nanoclusters, (c) D tryptophan and following addition of (d) 200 µL zinc complex of L tryptophan stabilized Au nanoclusters. (B) Bar diagram showing percentage change in ellipticity of D and L tryptophan upon interaction with zinc complex of L tryptophan stabilized Au NCs.

Next a possible mechanism of chiral recognition by the zinc complex of gold nanoclusters is proposed herein on the basis of classical "three-point versus two-point model" (Fig. 4.11 A-B). To elaborate, there are three points of interaction in tryptophan, namely – aromatic indole ring, COO^- and NH_3^+. In case of D tryptophan stabilized Zn-Au-NCs, coordinatively unsaturated surface zinc ion preferentially ligates to externally added D tryptophan, owing to more favourable spatial three-point interaction between D tryptophan stabilizing Zn-Au-NCs and D tryptophan added externally. The interaction between externally added L tryptophan and surface zinc ion of D tryptophan stabilized Zn-Au NCs is less favorable than the former, due to non-availability of one out of three points of interaction, keeping the coordination of zinc to externally added L tryptophan through carboxylate of the latter as a constant site of interaction. The same argument holds true in case of preferential interaction of L tryptophan stabilized Zn-Au-NCs with L tryptophan over D tryptophan.

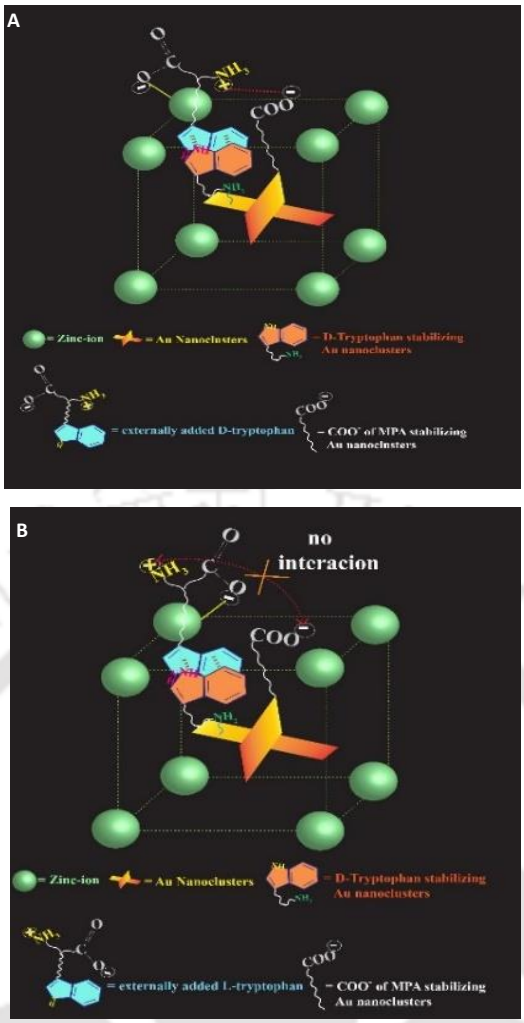

Fig. 4.11 (A) A representative model of three-point interaction between externally added D tryptophan and zinc complex of D tryptophan stabilized Au nanoclusters. (B) A representative model of two-point interaction between externally added L tryptophan and zinc complex of D tryptophan stabilized Au nanoclusters.

Moreover, the observation that no significant change in photoluminescence of ligand stabilized Au nanoclusters (without zinc ion) occurred, upon addition of D tryptophan and L tryptophan, further explains the essential role of zinc ion in chiral recognition and separation. In absence of zinc ion, it is unlikely that bare tryptophan would interact with itself in the liquid medium. Thus the mechanism of chiral recognition supplemented separation is likely to be based on coordination of zinc ion to D or L tryptophan; the degree of the interaction is being determined by higher number of interactions in case of D tryptophan with D tryptophan stabilized Zn-Au-NCs and L tryptophan with L tryptophan stabilized Zn-Au-NCs. Further, to verify the role of "pi- pi" interaction associated with hydrogen bonding in chiral recognition, an allied experiment was performed where L phenyl alanine was used to stabilize the clusters and the photoluminescence behavior of the same was studied upon interaction with L and D

phenylalanine. Interestingly, while for L tryptophan stabilized Au nanoclusters, the effect of L tryptophan and D tryptophan on photoluminescence of the former was markedly different, in the case of L phenylalanine stabilized Au nanoclusters, the difference in behavior of L and D phenylalanine was not stark. The photoluminescence of L phenylalanine stabilized Zn-Au-NCs was quenched by 6.3% upon addition of L phenylalanine while the photoluminescence of the former got quenched by 2.7% upon addition of D phenylalanine. The extent of decrease in photoluminescence of Zn-Au-NCs following interaction with phenylalanine (both D and L) is low as compared to tryptophan (D and L). This highlights that the feasibility of hydrogen bonding via hydrogen bonded to nitrogen in the indole ring of tryptophan played an additional role in chiral recognition, which, when as being absent in phenyl alanine, allowed chiral recognition with a lesser degree of distinction (Fig. 4.12).

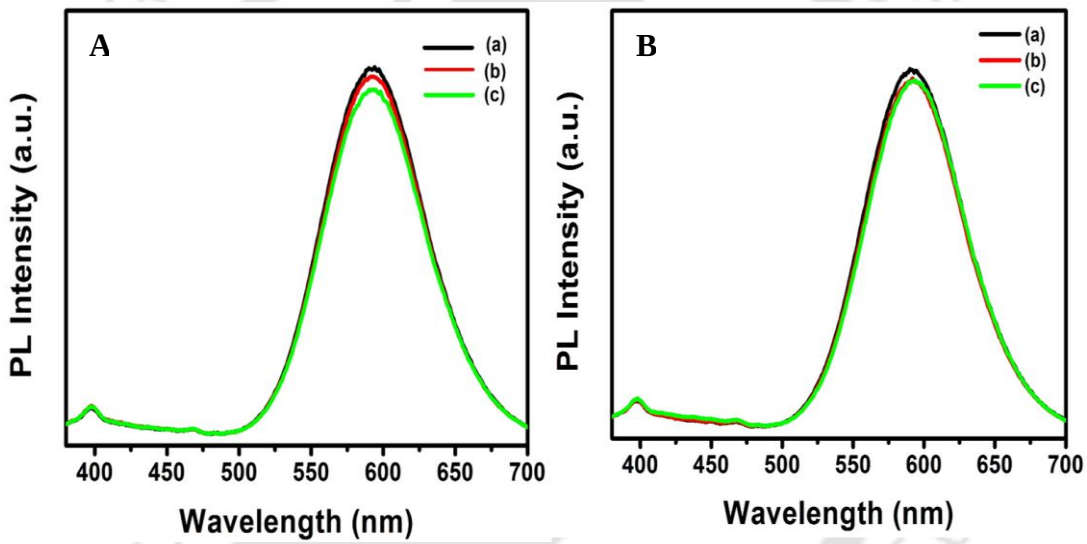

Fig. 4.12 (A) Photoluminescence spectrum of (a) zinc complex of L phenylalanine stabilized Au nanoclusters and that following addition of (b) 100 µL and (c) 200 µL of L phenylalanine (19.4 mg/mL). (B) Photoluminescence spectrum of (a) zinc complex of L tryptophan stabilized Au nanoclusters and that following addition of (b) 100 µL, (c) 200 µL of D phenylalanine (19.6 mg/mL).

The coordination between zinc ion and externally added D and L tryptophan was further confirmed by blocking the scope of surface reaction of zinc ion with D and L tryptophan. This has been pursued by performing reaction of D tryptophan stabilized Zn-Au-NCs with 8-hydroxyquinoline (HQ), which is known to form a stable complex with zinc ions on the surface of quantum dots with characteristic emission maxima at ~500 nm.[61] No change

in characteristic photoluminescence of D tryptophan stabilized Zn-Au-NCs, treated with HQ, was observed upon addition of D tryptophan, which otherwise had caused substantial quenching (Fig. 4.13).

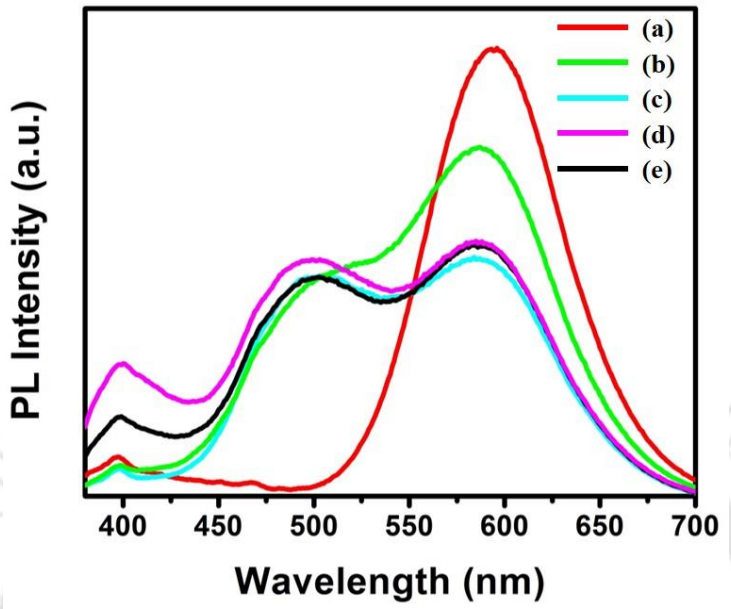

Fig. 4.13 Photoluminescence spectrum of (a) zinc complex of D tryptophan stabilized Au nanoclusters and that following addition of (b) 100 µL of 8- hydroxyquinoline, (c) the redispersion of the pellet obtained following centrifugation of the dispersion obtained in (b), and the spectra following addition of (d) 200 µL and (e) 400 µL of D tryptophan to the dispersion in (c).

Moreover, to stress upon the parity in dimensions of the amino acid stabilizing the cluster complex and the amino acid added to the complex, similar experiments were performed by adding glycine and L tyrosine to L tryptophan stabilized Zn-Au-NCs. Intriguingly, while interaction of L tryptophan with L tryptophan stabilized Zn-Au-NCs led to prominent change in photoluminescence of the latter, glycine and L tyrosine had much less pronounced effect on the photoluminescence intensity of Zn-Au-NCs. The response was much similar to that of D tryptophan added onto L tryptophan stabilized Zn-Au-NCs (Fig. 4.14). This highlights the criticality of geometry of the amino acid present in the chiral selector and the amino acid externally added, for favorable interaction between the two following coordination of the latter to zinc ions of the complex. Further, this also highlights the specificity in recognition, as we pursued the effect of an aliphatic and an aromatic amino acid – namely glycine and L tyrosine to the zinc complex of L tryptophan stabilized Au NCs

(Zn Au NCs). Glycine was chosen as a model of control experiment as it lacks intrinsic chirality and it exhibits maximum size mismatch with tryptophan. In contrast, tyrosine has been tested as another model as it has maximum structural similarity with tryptophan, except for the fact that it has a single six membered aromatic ring while tryptophan has a five membered aromatic ring fused with a six membered ring. It has been observed that while L tryptophan had prominent effect on photoluminescence intensity of L tryptophan stabilized Zn Au NCs, L tyrosine and glycine had much less pronounced effect on the photoluminescence intensity of L tryptophan containing Zn Au NCs. Rather, the effect of L tyrosine and glycine was much similar to that of D tryptophan added to L tryptophan stabilized Zn Au NCs. This result was much anticipated as the principle involved herein for chiral recognition is based on functional group specific interaction between the selector and the analyte. For example, the externally added tryptophan would undergo “pi-pi” interaction with the tryptophan present in the complex. Similarly, the NH_3^+ group of the externally added tryptophan would react with COO^- of mercaptopropionic acid present in the complex. This in turn demands not only perfect orientation of the functional groups of the selector with respect to the analyte but also exact size matching between the functional groups (in addition to three-dimensional orientations) of the two for successful recognition. This makes the tryptophan (both D and L) containing complex highly specific for its identical analogue to be sensed (Fig. 4.14).

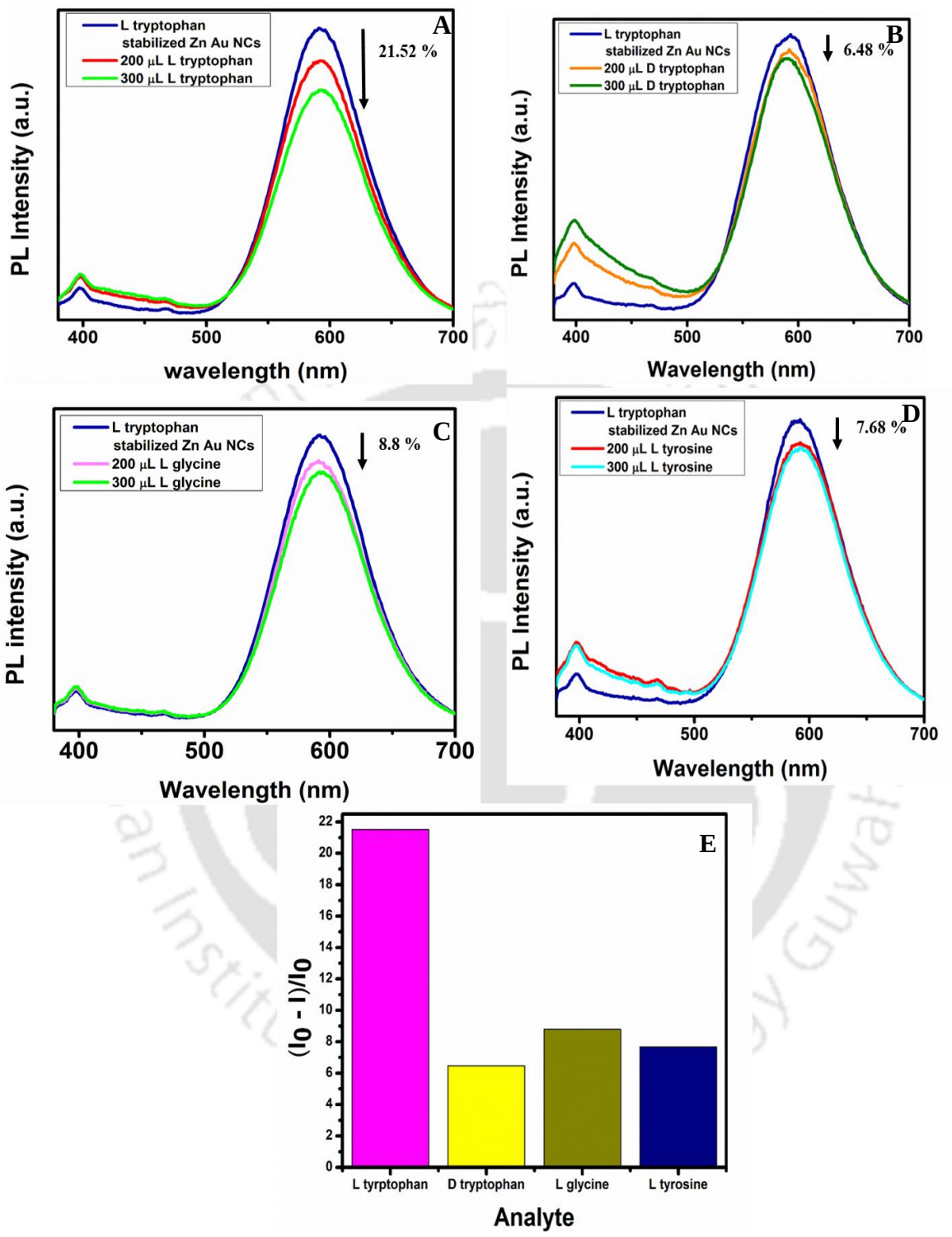

Fig. 4.14 Effect of (A) L tryptophan on PL intensity of L tryptophan stabilized Zn-Au-NCs, (B) D tryptophan on PL intensity of L tryptophan stabilized Zn-Au-NCs, (C) Glycine on PL intensity of L tryptophan stabilized Zn-Au-NCs, (D) L tyrosine on PL intensity of L

tryptophan stabilized Zn-Au-NCs. The (E) extent (%) of quenching of PL intensity of Zn-Au-NCs in presence of various amino acids.

The fact that the morphology of Zn-Au-NCs remained intact upon interaction with both D and L tryptophan was revealed from FESEM analysis (Fig. 4.15). This further proved that the mechanism of chiral recognition was through chemical coordination between selector and analyte and thus has no consequential change in external morphology of the chiral selector, Zn-Au-NCs.

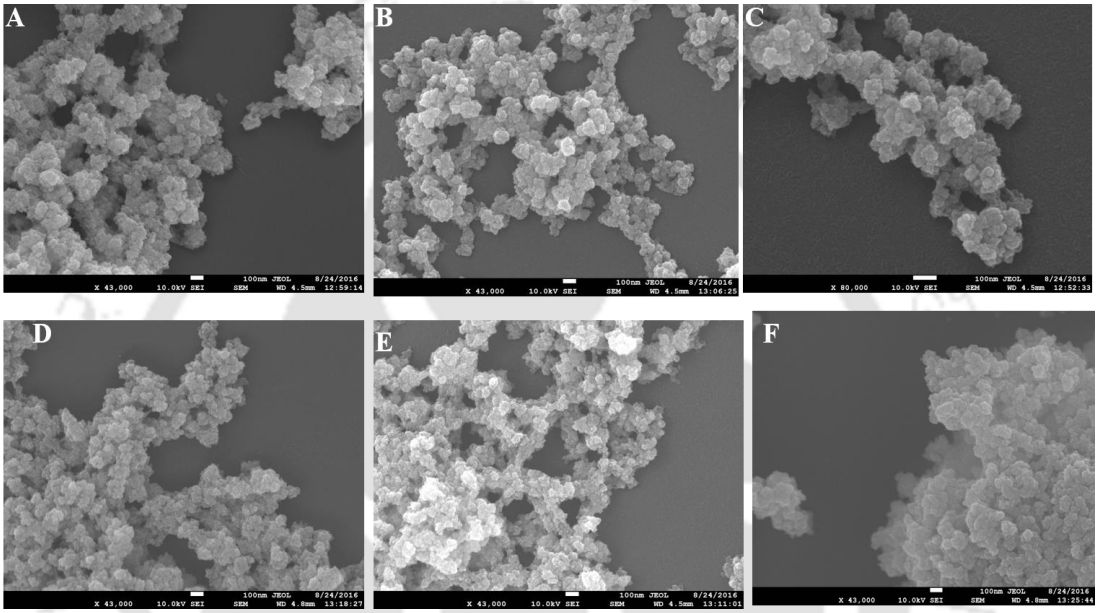

Fig. 4.15 FESEM image of (A) D tryptophan stabilized Zn-Au-NCs and that following addition of (B) 200 µL D tryptophan or (C) 200 µL L tryptophan. (D) L tryptophan stabilized Zn-Au-NCs and that following addition of (E) 200 µL D tryptophan or (F) 200 µL L tryptophan.

4.3 Conclusions

In summary, we have designed a new strategy for chiral recognition as well as separation based on a new crystalline assembly of chiral ligand stabilized Au_{14} nanoclusters. This is based on complexation reaction assisted three dimensional assembly of tryptophan (of a particular enantiomer) and MPA stabilized Au nanoclusters. The assembled nanoclusters not only exhibited superior optical properties but also enabled chiral recognition with concurrent separation of enantiomers of tryptophan, which was not possible using only ligand stabilized nanoclusters. Thus, hierarchical organization of quantum clusters, using wide repertoire of

fundamental chemistry along with subsequent application potential in chiral recognition of biologically relevant molecules, may provide a new and unique dimension to the emerging field.

Chapter 5

Crystalline Assembly of Gold Nanoclusters for Mitochondria Targeted Cancer Theranostics

Herein we report the formation of crystalline assembly of gold (Au) nanoclusters for cancer theranostics via active targeting of mitochondria. To the best of our knowledge this is the first report of target specific activity of "assembly of gold nanoclusters". Au_{14} nanoclusters were stabilized with mercaptopropionic acid and L tyrosine. Limited solubility of L tyrosine in methanolic solution led to formation of polycrystalline assembly of Au nanoclusters via interactions between ligands (tyrosine) stabilizing the clusters. Further, complexation reaction between zinc ions and ligands stabilizing Au nanoclusters led to formation of single crystalline assembly of gold nanoclusters. Transmission electron microscopy and selected area electron diffraction analyses revealed the formation of faceted crystals with hexagonal arrangement of Au_{14} nanoclusters. A theoretical structure of the crystalline complex of Au nanoclusters and zinc ions has been proposed herein based on experimental observations and computational optimization. Crystalline assembly of Au nanoclusters, formed via ligand association as well as complexation reaction, exhibited mitochondria targeted anti-cancer activity - as verified by Mito tracker staining experiments. However, MTT assay, FACS analysis and JC-1 staining experiments revealed that zinc mediated assembly of Au nanoclusters exhibited superior therapeutic action as compared to methanol driven assembly of the clusters.

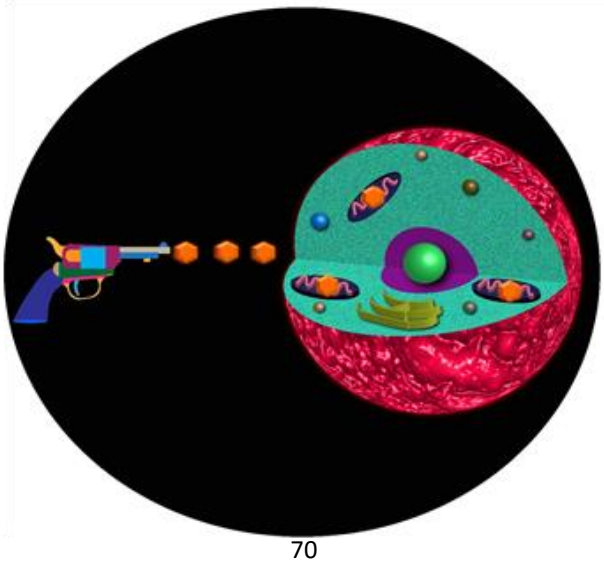

Basu, et. al. J Mat Chem B (2018), 6, 1650-1657. Reproduced with permission following the rules of Royal Society of Chemistry. Copyright belongs to J. Mater. Chem. B, RSC.

5.1 Experimental

5.1.1 Materials:

Tetrachloroauric acid, mercaptopropionic acid, L tyrosine, (3-(4, 5-dimethylthiazolyl-2)-2,5-diphenyltetrazoliumbromide)(MTT),5,5',6,6'tetrachloro1,1',3,3'tetraethylbenzamidazolylcarbocyanine iodide (JC-1 dye) and 2,7-dichlorofluoresceindiacetate (DCFH-DA) were purchased from Sigma-Aldrich. Zinc acetate dihydrate was procured from Merck. Mitotracker green was purchased from Imperial Life Science (P) Ltd. Two cell lines used in this work i.e. HeLa (human cervical carcinoma) and HEK-293 (human embryonic kidney cell) were procured from National Centre for Cell Sciences (NCCS), Pune, India.

Instruments:

Optical study: All experiments related to fluorescence study of Au nanoclusters, Au nanocrystals and the corresponding zinc complex was done using HORIBA Jobin Yvon FluoroMax-4 spectrofluorimeter. UV study was performed using Perkin Elmer, Lambda 750 UV-visible spectrophotometer.

Transmission electron microscopy (TEM) and selected area electron diffraction (SAED) study: TEM and SAED images of Au nanoclusters, Au nanocrystals and Zn Au NCs were acquired using JEOL JEM 2100 and JEOL JEM 2100F at an accelerating voltage of 200 kV. TEM samples were prepared following deposition of dispersion (aqueous) of samples on carbon coated copper grid.

Fourier transform infrared (FTIR) spectroscopy: Thermo Scientific FTIR spectrophotometer was used for FTIR analysis of Au nanoclusters and Zn Au NCs.

Time resolved photoluminescence (TRPL) analysis: TRPL analysis of Au nanoclusters and zinc complex of gold nanoclusters was performed using Life-Spec-II spectrofluorimeter (Edinburgh Instrument). TRPL analysis was done under continuous stirring condition to avoid settlement of the samples.

MTT assay: To check the cytotoxicity of Au nanocrystals and Zn Au NCs on Hela and HEK-293 cell lines, MTT (3-(4,5-dimethylthiazolyl-2)-2,5-diphenyltetrazolium bromide) assay was carried out after 24 h of treatment. For this 5×10^3 cells were seeded in each well of 96 well plate and kept overnight followed by treatment with varying concentrations of Au nanocrystals (77.5 µg/mL) and Zn Au NCs (77.5 µg/mL) for 24 h, in triplicates. MTT was

added in each well after 24h of treatment where it passes into mitochondria of metabolically active cells and results in formation of insoluble purple colored formazon. The resulting formazon was dissolved in DMSO and its absorbance was measured at 550 nm with background reference measured at 655 nm in Multiplate Reader (Tecan), which is calculated as:

$$\% \text{ of Cell Viability} = \frac{(A_{550} - A_{655})_{sample}}{(A_{550} - A_{655})_{control}} \times 100$$

Confocal Microscopy: To check the internalization of Au nanocrystals and Zn Au NCs confocal microscopy studies were carried using Zeiss LSM 880 microscope where 5×10^3 cells were first grown on a coverslip in 35mm culture plate and maintained at 5% CO_2 humidified conditions (37 °C for 24 h). Thereafter, cells attached on cover slip were treated with IC_{50} dose (77.5 µg/mL) of Au nanocrystals and Zn Au NCs for 4h followed by thorough washing with PBS. Finally, the cells were fixed using 70% chilled ethanol. Immediately, the coverslips were mounted on a glass slide and the sides were sealed. Similarly control cells (i.e without treatment) were also prepared in an allied manner. The prepared samples were observed under red channel (with λ_{ex} 405 nm).

JC-1: For JC-1 staining live cell confocal imaging was carried out where the cells were grown in special 35 mm live cell culture plate overnight. When confluent enough, the cells were treated with IC_{50} dose of Au nanocrystals and Zn Au NCs for 24h. Thereafter, the cells were thoroughly washed with PBS twice and were incubated with JC-1 dye (2.7 µM) for 10 minutes and live cell imaging was carried out in red and green with the diode laser λ_{ex}= 525 nm and λ_{ex}= 480 respectively.

Mitotracker Green : For imaging with Mitotracker green, the cells were incubated with Au nanocrystals and Zn Au NCs for 3 h and were washed twice with PBS followed by incubation with 300 nM mitotracker green for 30 min and were fixed using 70% chilled ethanol. The fixed cells were mounted on a glass microscopic slide, and the sides were sealed. The fixed samples were then imaged under Zeiss LSM 880 confocal microscope (λ_{ex} = 405 nm) and (λ_{em} = 590 nm) for the nanocrystals and (λ_{ex} = 405 nm) and (λ_{em} = 530 nm) for mitotracker green, respectively.

FACS Analysis for Reactive Oxygen Species Generation: Generation of reactive oxygen species was investigated by using 2,7-dichlorofluoresceindiacetate (DCFH-DA) dye, which diffuses into the cell through plasma membrane and is deacetylated by cellular esterases to a non-fluorescent compound DCFH. With elevation in ROS level, this DCFH is oxidized into 2', 7' –dichlorofluorescein (DCF) giving green fluorescence (λ_{ex}=488 nm and λ_{em}=530 nm). For this, the cells with 5×10^3 cells/well were seeded in 6 well plate and kept overnight which was followed by treatment with 77.5 µg/mL of Au nanocrystals and Zn Au NCs respectively for 3 h. Afterwards, in each well including the control 10 µM of DCFH-DA was added and kept at 37 °C for 30 min. Then the cells were collected after trypsinization and were re-dispersed in DMEM before being analyzed in a fluorescence activated cells sorter (FacsCalibur, BD Biosciences, NJ) in FL1-H channel (530/30nm), which corresponds to green emission. The Cell Quest program (BD Biosciences) was used to record the fluorescence data with 15000 cells in each well.

ICP atomic emission spectrometric ananlysis: For ICP atomic emission spectrometric analysis, 5×105 of HeLa cells were seeded in 6 well plates and were kept for 24h.The overgrown cells were treated with Au nanocrystals (77.5 µg/mL) and Zn Au NCs (77.5 µg/mL) for 6h. Thereafter the cells were treated with 3% sub-boiled nitric acid for 2h. Thereafter the supernatant was collected and used for ICP atomic emission spectrometric analysis.

Synthesis of Tyrosine stabilized Au nanoclusters and Au nanocrystals: 10 mL methanol was added with 1 mL $HAuCl_4$ (10 mM) followed by 0.4 mL MPA (0.11 M). The yellow color of the solution began to fade. In a separate vial, ~12 mg of tyrosine was dissolved in 1 mL water using 0.8 mL 1 M NaOH (freshly prepared). The mixture was allowed to stir for 10 min and then centrifuged at a speed of 10,000 rpm for 10 min. The pellet was redispersed in 1 mL water and centrifuged again. The so obtained pellet was redispersed in 1 mL water and was used for further complexation with zinc.

Synthesis of crystalline complex of Tyrosine stabilized Au nanoclusters and zinc ions: To 1 mL of above prepared dispersion, ~100 mg of zinc acetate dehydrate was added and further stirred for 10 min. The dispersion was centrifuged at a speed of 10,000 rpm for 10 min and the pellet was redispersed in 1 mL water and centrifuged again. Finally, the pellet was redispersed in 1mL water and used for further experiments.

5.2 Results and discussions

Experimentally, upon addition of mercaptopropionic acid (MPA) followed by L tyrosine (Tyr) to a solution of tetrachloroauric acid ($HAuCl_4$) in methanol, a luminescent colloidal dispersion was formed. This was indicative of the formation of Au nanoclusters. Transmission electron microscopy (TEM) analysis of the centrifuged product of the aforementioned dispersion indicated the presence of particles in the range of 2 nm, which substantiated the formation of atomic gold nanoclusters (Fig. 5.1). Electrospray ionization mass spectrometry (ESI-MS) indicated a peak at 1366.84 (Fig. 5.2). This was attributed to the presence of ligand stabilized Au_{14} species with a chemical formula of $Au_{14}MPA_6Tyr_4$. Interestingly, TEM images of the above dispersion (Fig. 5.3 A) also marked the presence of larger particles (~ 5-6 nm). However, the UV-Vis absorption spectrum of these particles was devoid of any peak at 530 nm, which is usually attributed to the presence of gold nanoparticles (Fig. 5.3 B). Thus, it could be ascertained that the bigger particles (as compared to the dimensions of Au_{14} nanoclusters) observed in the TEM were not Au NPs formed as a by-product of cluster synthesis. This was also evident from electron diffraction analysis of these particles, which were distinctly different from those of typical gold NPs (Fig. 5.3 C). Instead, it could be inferred that the bigger particles could be formed as a consequence of inter - ligand (Tyr) interaction based association. Given the fact that Tyr was bonded to the surface of Au nanoclusters, it could be anticipated that precipitation of Tyr would consequentially lead to assembly of Au nanoclusters embedded in it. Here, two different principles were combined to crystallize Au nanoclusters through association of Tyr. Firstly, methanol, which is known to cause “solvent induced aggregation” of nanoclusters, was used as the solvent for synthesis of clusters so as to imbue the clusters with an inherent tendency to aggregate. On the other hand, Tyr is known to be insoluble in methanol. Thus, when partially solubilized alkaline solution of Tyr was added to a mixture of $HAuCl_4$ and MPA, crystallization of Tyr (which was attached to the nanoclusters) was possible owing to lack of solubility of Tyr in methanol. These factors, in combination, might have led to formation of nanocrystals of Tyr with Au nanoclusters embedded in it, which are hereafter referred to as Au nanocrystals.

In the next step, complexation reaction between Au nanoclusters and zinc ions was pursued at room temperature following addition of zinc acetate dihydrate to the dispersion containing as –synthesized Au nanoclusters and Au nanocrystals (formed due to the

association of the Tyr-stabilized clusters in the medium). This led to the enhancement of luminescence intensity and excited state lifetime of Au nanoclusters (Fig. 5.4, Table 5.1). The increase in luminescence quantum yield as well as life time was attributed to the structural rigidity attained by the clusters upon reaction with zinc ions.

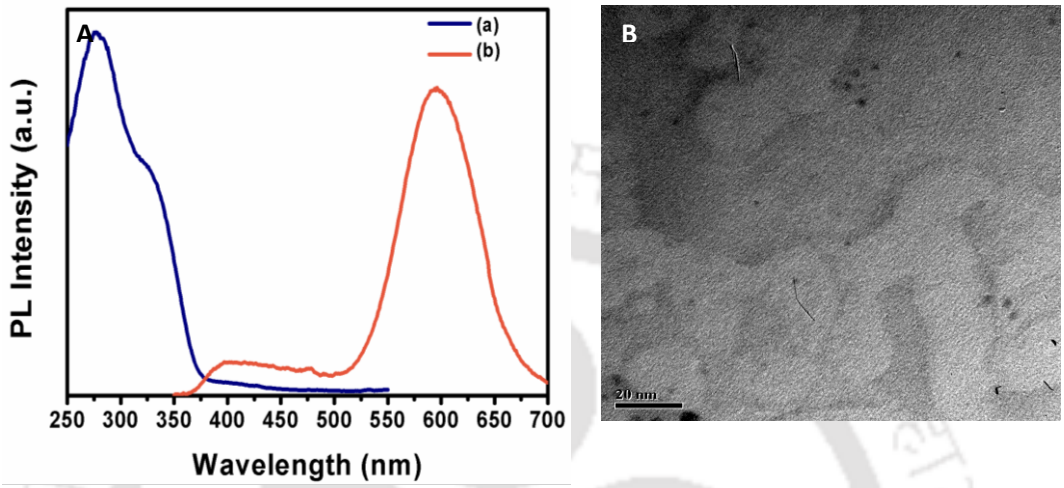

Fig. 5.1 (A): (a) Excitation and (b) emission spectra of dispersion containing MPA and tyrosine stabilized Au nanoclusters and nanocrystals. (B) Transmission electron microscopic (TEM) image of MPA and tyrosine stabilized Au nanoclusters.

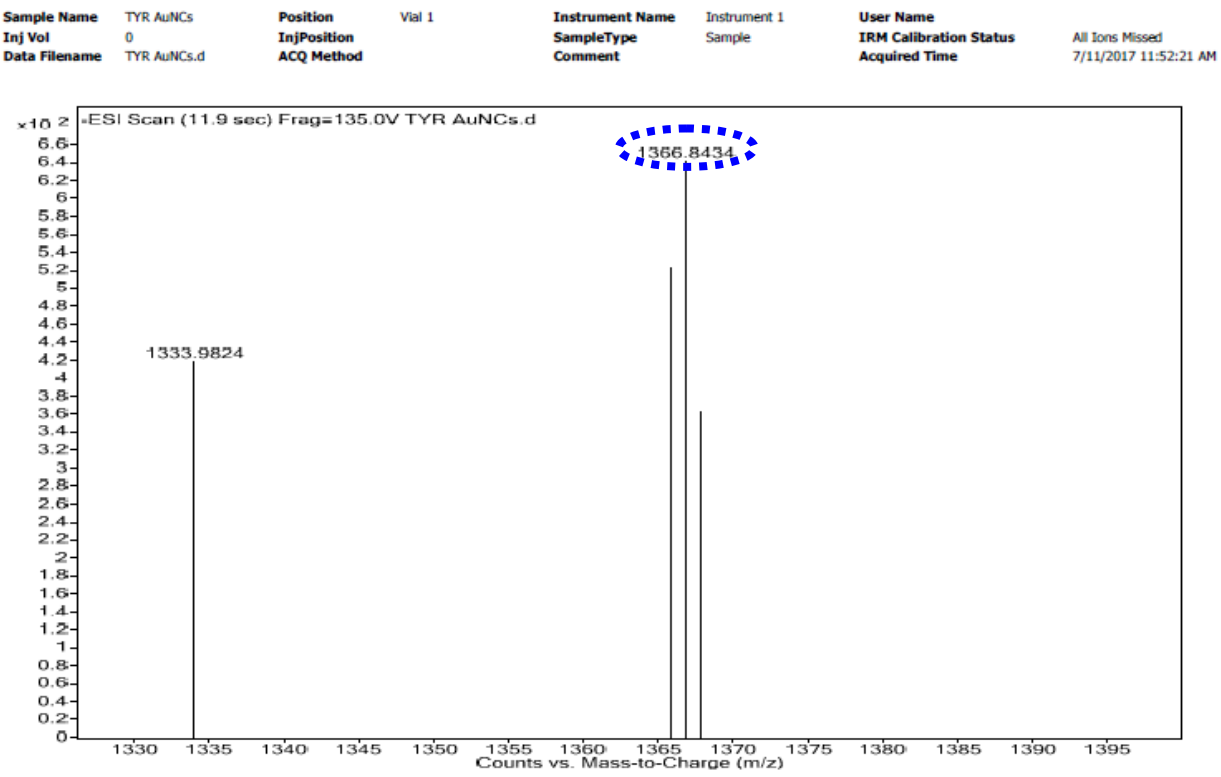

Fig. 5.2 Electrospray ionization mass spectrometric analysis of MPA and tyrosine stabilized Au nanoclusters. The peak at m/z equal to 1366.84 corresponds to the presence of $[Au_{14}MPA_6Tyr_4 + 3H^+]^{3-}$.

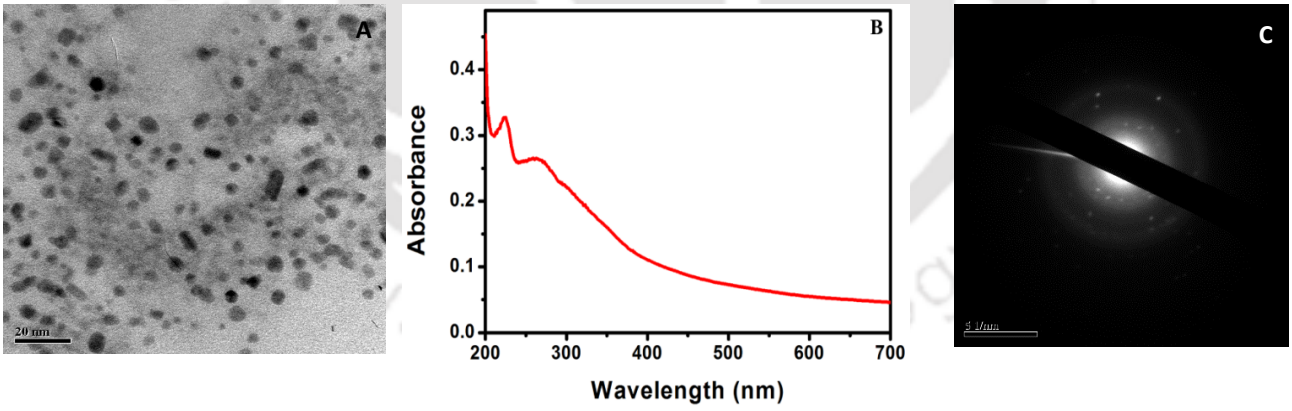

Fig. 5.3 (A) Transmission electron microscopic (TEM) image and (B) UV-Vis absorbance spectrum of Au nanocrystals formed by association of tyrosine. (C) SAED of a typical particle shown in (A).

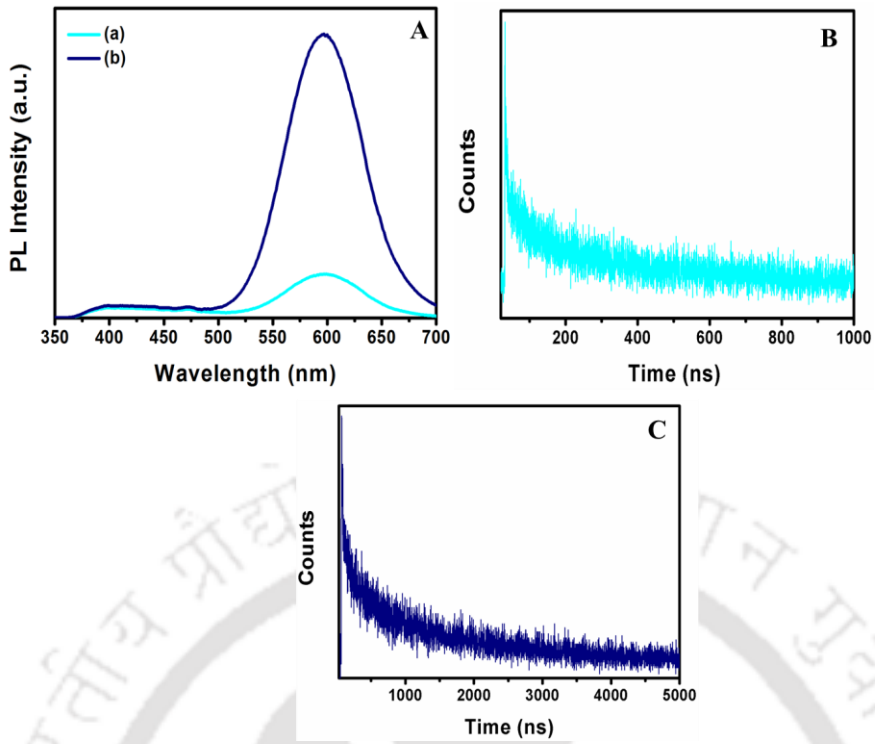

Fig. 5.4 A) Photoluminescence spectra of (a) Au nanoclusters and (b) product of reaction of Au nanoclusters with zinc ions. Time resolved photoluminescence spectra of (B) Au nanoclusters and (C) the product of reaction between Au nanoclusters and zinc ions.

Table 5.1 Time-resolved photoluminescence decay parameters of Au nanoclusters measured prior to and following reaction with zinc ions.

Sample	A1 (%)	τ_1 (ns)	A2 (%)	τ_2 (ns)
Au nanocrystals	**9.762**	**11.661**	**90.238**	**255.424**
Product of reaction between Au nanoclusters and zinc ions	**9.355**	**105.304**	**90.645**	**1453.341**

Interestingly, TEM analysis of the centrifuged product of the reaction between Au nanoclusters and zinc ions revealed the formation of crystalline nanoparticles with distorted

hexagonal electron diffraction pattern. The crystalline nanoparticles formed as a result of reaction between zinc ions and Au nanoclusters are hereafter referred to as Zn Au NCs. Zn Au NCs, as observed in TEM, marked the presence of hexagonal facets (Fig. 5.5 A-B). This was intriguing as synthesis of nanocrystals with high index facets is a persistent challenge in crystallography.[62] Each distorted hexagon observed in the selected area electron diffraction (SAED) pattern of one such particle comprised of two distinct edge lengths, which were measured to be 3.4 Å ± 0.2 Å and 3.1 Å ± 0.2 Å (Fig. 5.5 C). On the other hand, theoretical study reveals that flat 3D structure with D_{2h} symmetry is a stable form of Au_{14}.[63] Interestingly, the distances observed in SAED were in close corroboration with the intra cluster gold-gold distances of the theoretically predicted structure of Au_{14}. Similarly, the other dimension of the crystal was obtained from SAED performed on a typical particle. The third dimension of the crystalline particle has been observed to be 3.3 ± 0.2 Å (Fig. 5.5 D), which corresponds to gold –gold distances (vertical direction) in a single cluster. Further, the distance of 5.3 ± 0.3 Å (Fig. 5.5 E-F), obtained on relatively larger crystalline or NPs was attributed to separation between hexagonally arranged individual clusters coordinated through zinc ions. The formation of the crystal in the direction with longer axis is proposed to have been possible through coordination of tyrosine attached to one gold cluster to tyrosine of another cluster via zinc ion. This distance of 9.0±0.8 Å has been obtained from electron diffraction pattern of the crystalline complex (Fig. 5.5 G-H).

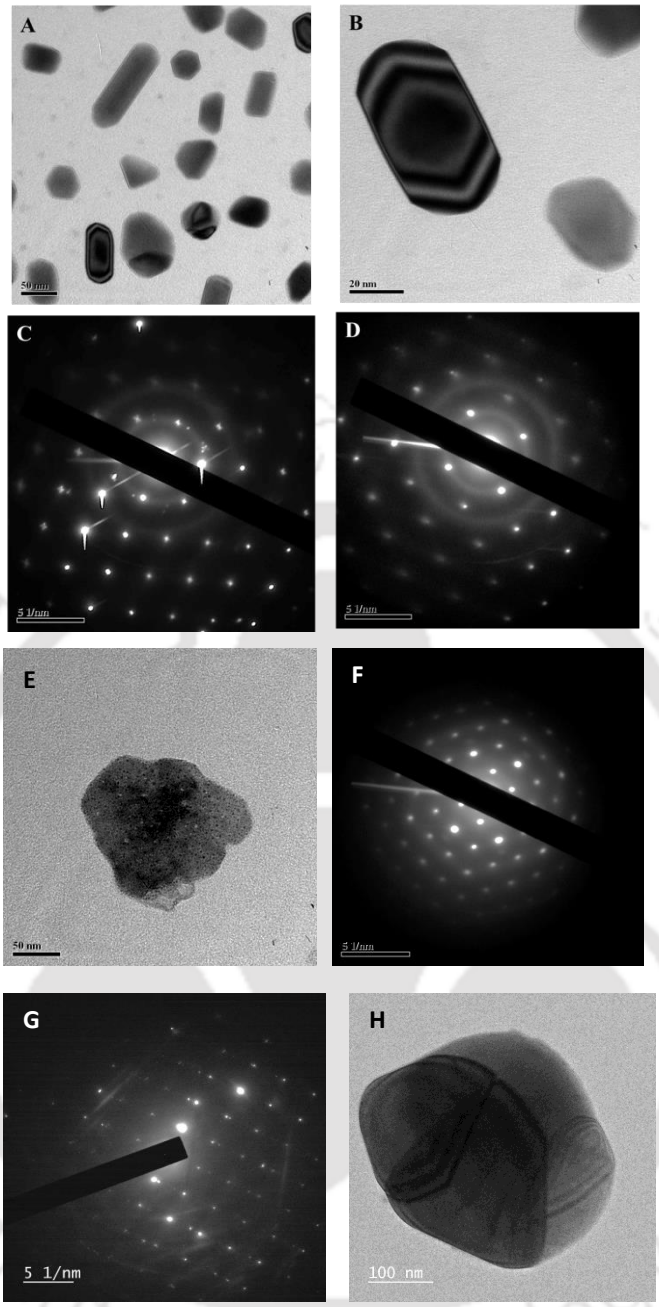

Fig. 5.5 (A-B) Transmission electron microscopic (TEM) images of zinc coordinated Au nanoclusters. (C) Corresponding selected area electron diffraction (SAED) pattern. (D) SAED of a typical particle viewed along a different zone axis. (E) TEM image of a particle comprising of zinc coordinated Au nanoclusters (F) Corresponding SAED pattern. (G) SAED pattern of Zn Au NCs viewed at a different zone axis and (H) corresponding TEM image.

A computed structure of Zn Au NCs based on the above experimental observations was obtained using "Avogadro". Interestingly; the distances obtained therein were in close

concordance with those observed experimentally (Fig. 5.6 A). Based on the electron diffraction patterns, a structure depicting the position of Au atoms and zinc ions has been proposed herein (Fig. 5.6 B - C). Briefly, six Au_{14} clusters are positioned in a hexagon where the clusters define the apexes of the hexagon and one Au_{14} cluster is positioned in the centre of the so formed hexagon. Each zinc ion is coordinated to two clusters at the apexes and one at the centre through MPA (two MPA per cluster) thereby attaining an octahedral geometry and thus forming the connection between the three clusters. Thus each repeat unit of the crystal in the plane is comprised of seven Au_{14} clusters (six at the apexes and one at the centre) and three zinc ions. On the other hand, zinc ions were coordinated to tyrosine attached to the clusters (two tyrosine per cluster) of each hexagonal layer (comprised of clusters) and further extend the crystal in the third dimension (as shown in Fig. 5.6 B-C). A representative structure depicting the spatial arrangement of the constituents is shown in Fig. 5.6 D. Fourier transform infra-red (FTIR) analysis of Au nanoclusters and the product of its reaction with zinc ions revealed the possible mode of bonding between the ligands stabilizing Au nanoclusters and zinc ions through carboxylate groups of MPA and Tyr. The detail of the analysis is provided in the Electronic Supporting Information (Fig. 5.7).

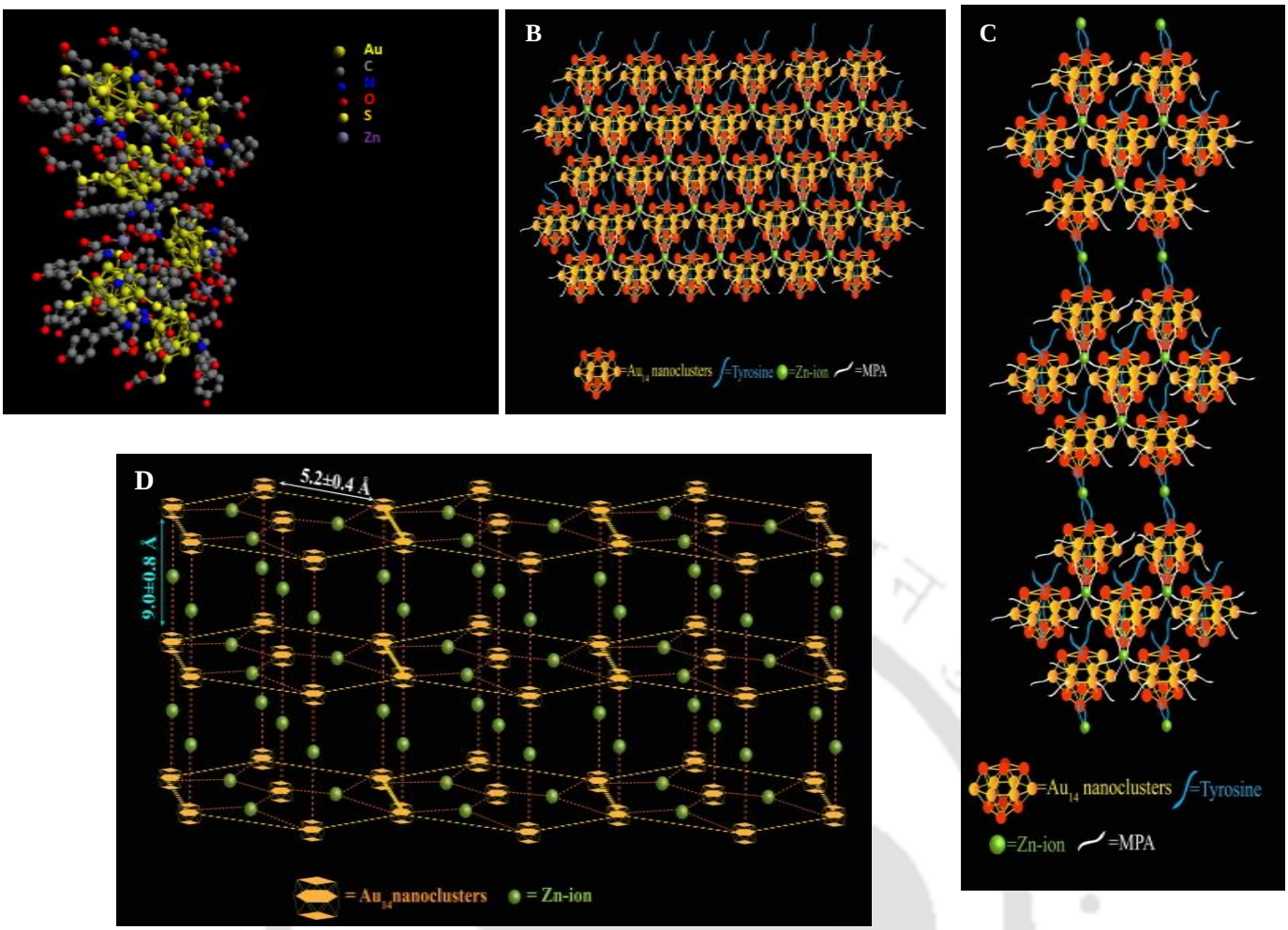

Fig. 5.6 (A) Computationally optimized structure of zinc assisted assembly of Au nanoclusters. (B - C) Schematic representation of the structure of zinc assisted assembly of Au nanoclusters. (D) Schematic representation of the structure of the crystalline complex of Au nanoclusters and zinc ions.

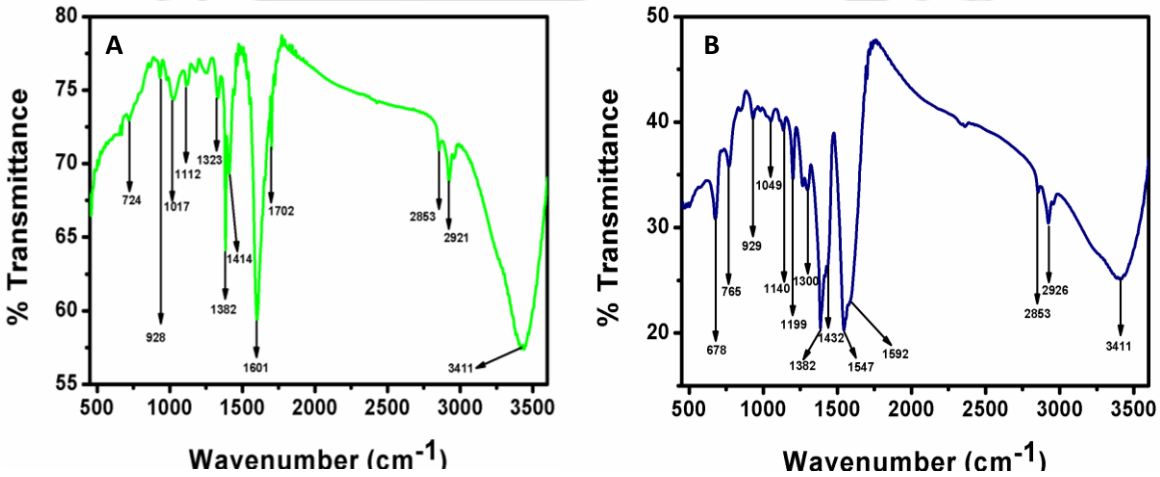

Fig. 5.7 FTIR spectra of (A) MPA and tyrosine stabilized Au nanoclusters and (B) the product of reaction between zinc ions and Au nanoclusters.

Additional representative TEM images are shown below (Fig. 5.8).

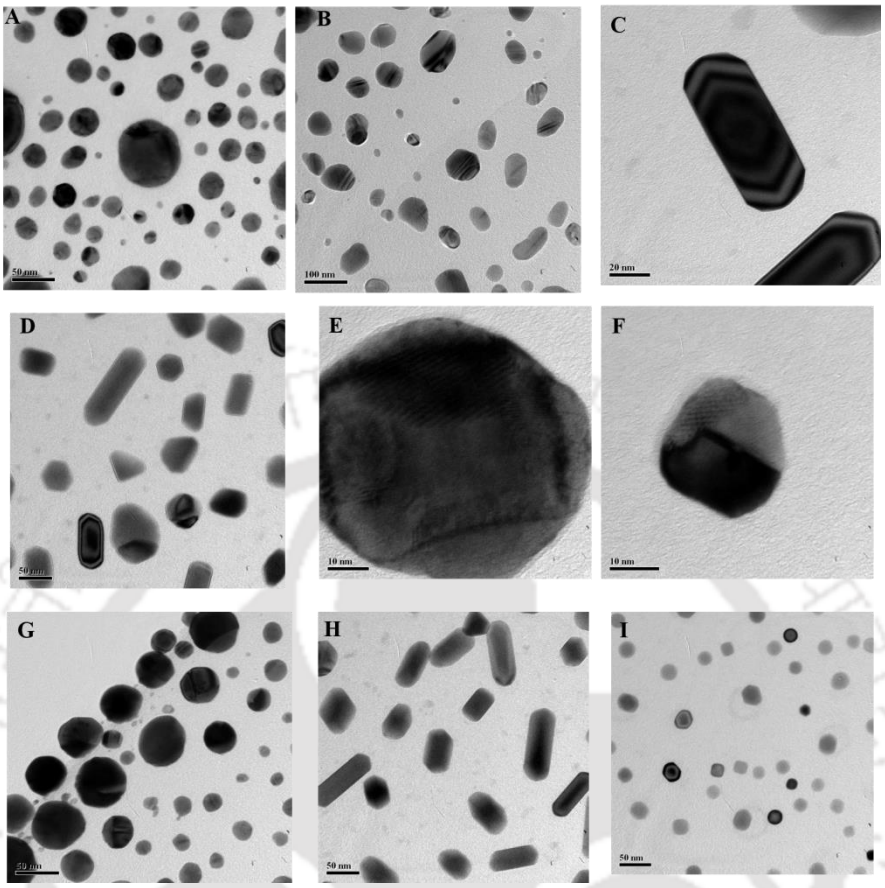

Fig. 5.8 (A) Additional representative TEM images of the product of reaction between zinc ions and Au nanoclusters (MPA and tyrosine stabilized) performed on different samples as well as recorded on different regions of the same sample.

Notwithstanding the significant progress made in the field of nanomedicines for anti-cancer activity, the development of organelle (such as mitochondria) targeting nanodrugs remains a challenge.[64] Additionally, use of NPs as supplement of molecular forms of drugs with the possibility of facile uptake at the site and possible renal clearance hold the key to their real life applications. Thus, nanoparticulate drugs not only portend to offer superior therapeutic efficacy but may also help minimize adverse effects.

The crystalline NPs comprising of Au nanoclusters coordinated by zinc ions, reported herein (Zn Au NCs), seemed an ideal candidate as mitochondria targeting anti-cancer agent. In general, nanoclusters of gold are known to be non-toxic and can be internalized in cells. Hence quantum clusters of gold have been used to fabricate drug delivery vehicles and bio imaging agents. Also, it has been demonstrated herein that Au nanoclusters synthesized in

presence of mercaptoundecanoic acid (MUA),[65] which did not self-assemble to form NPs, were non-toxic (Fig. 5.9). As mentioned above, Au nanoclusters synthesized in presence of MPA and Tyr led to the formation of NPs comprising of nanoclusters (via interaction of Tyr) with sizes on the order of 2 nm. As per MTT assay, Au nanocrystals were observed to induce cell death in Hela cells. MTT assay also revealed that Tyr induced minimum toxicity and hence is biocompatible (Fig. 5.10). Interestingly, superior anti-cancer activity of Zn Au NCs was observed in comparison to Au nanocrystals (Fig. 5.11 A). Precisely, while at a dose of 77.5 µg/mL Zn Au NCs, 52% cell death was observed, at the same dose of Au nanocrystals (18.9 nM), 31% cell death occurred.

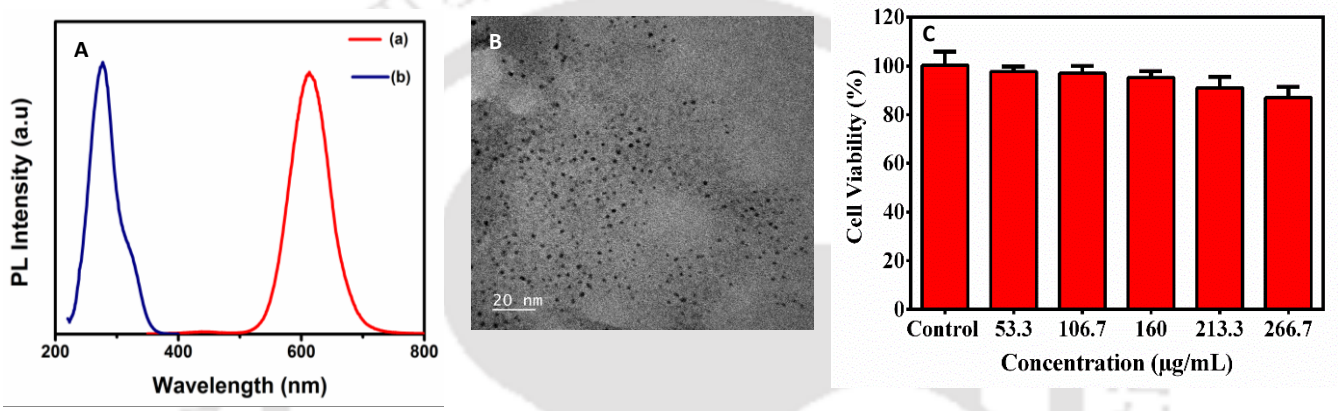

Fig. 5.9 (A) (a) Excitation and emission spectrum of mercaptoundecanoic acid stabilized Au nanoclusters (B) TEM image of mercaptoundecanoic acid stabilized Au nanoclusters. (C) MTT assay based cell viability of HeLa cells following treatment with mercaptoundecanoic acid stabilized Au nanoclusters. The results show that ultra-small Au nanoclusters have negligible cytotoxic effect on HeLa cells.

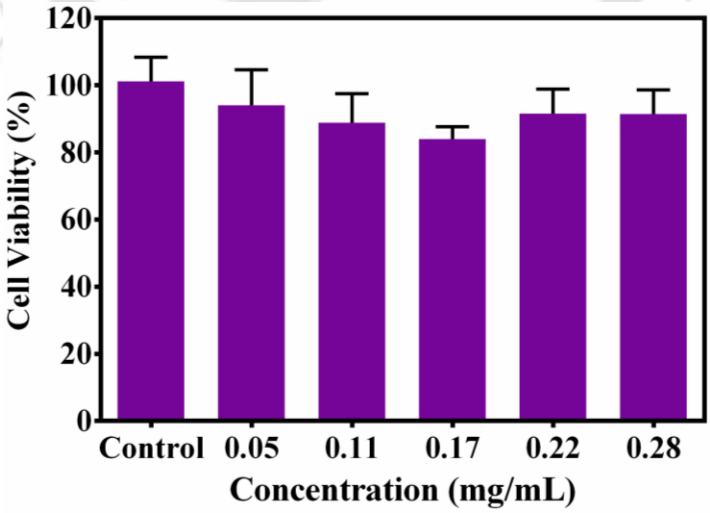

Fig. 5.10 MTT assay performed on Hela cells following treatment with L tyrosine.

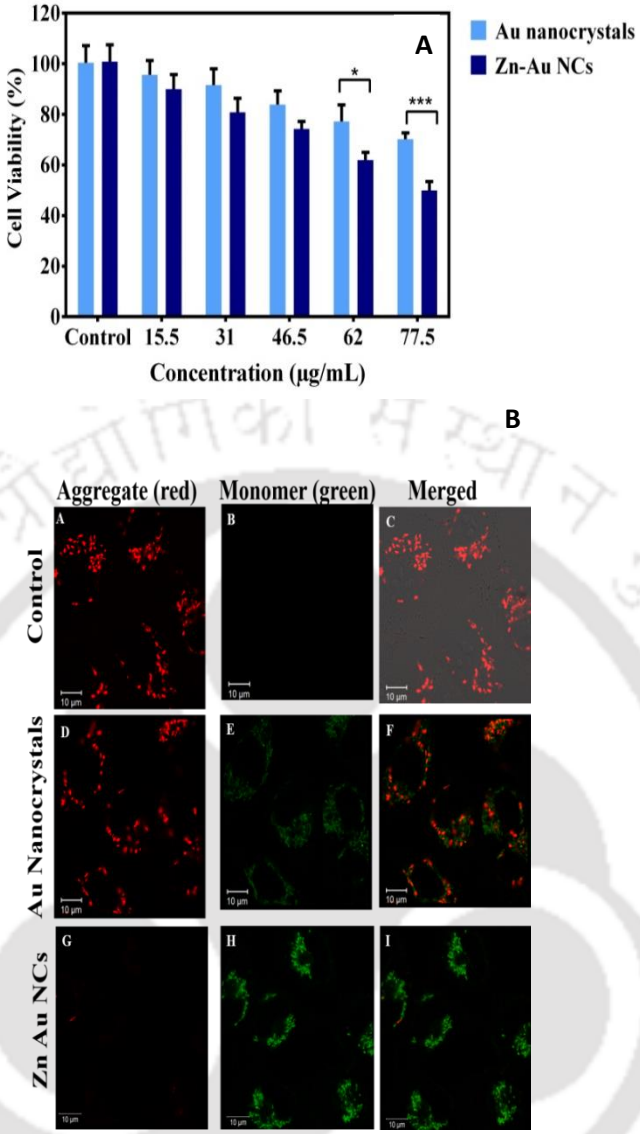

Fig. 5.11 (A) MTT assay of Hela cells treated with dispersion of Au nanocrystals and the product of reaction with zinc ions. (B) Confocal laser scanning microscopic (CLSM) images of HeLa cells with JC-1 dye in (A) Control Hela cells (i.e., without treatment) red channel, (B) green channel and (C) merged image of (A) and (B). CLSM images of Hela cells with JC-1 dye following treatment with dispersion containing Au nanocrystals acquired in (D) red channel, (E) green channel and (F) merged image of (D) and (E). CLSM images of Hela cells treated with JC-1 dye following treatment with zinc added Au nanoclusters acquired in (G) red channel (H) green channel and (I) merged image of G and H.

A plausible explanation for anticancer activity of assembled Au nanoclusters and higher cytotoxic activity of Au nanocrystals in comparison to Zn Au NCs is given below.

Plausible mechanism of anticancer activity of assembled Au nanoclusters:

Gold based compounds, owing to their medicinal properties, have been employed as anti-arthritis and anti-inflammatory agents. However, limited anticancer activity of Auranofin - a known anti-rheumatic agent – has expedited the quest for development of gold based anticancer agents. In this regard, substantial amount of efforts has been invested in modification of ligands coordinated to gold (I) to render them as effective anti-cancer agents. However, exploring coordination chemistry on the surface of Au nanoclusters to infuse them with anti-proliferative property would be an interesting approach towards development of newer "nanodrugs". This could, in principle, be achieved via formation of a metal ion mediated crystalline complex (assembly) of Au nanoclusters, where the surface Au atoms are known to be partially oxidized. It would be even better if the constituents of the clusters could specifically interact with the molecules – indispensible for cellular activities - present on the cellular organelles, thereby rendering them inactive and eventually leading to cell death. In this regard, mitochondria, owing to its pivotal role in cell metabolism, have emerged as an important target for cancer therapy. Efforts are being made to design nano vectors to specifically deliver therapeutic molecules to mitochondria. On the other hand, it is known that thioredoxin reductase (TrxR), an enzyme ubiquitous in mitochondria and upregulated in cancer cells, is essential to reduce thioredoxin (Trx). As per literature reports, Au (I) complexes specifically binds to the active site of TrxR. Thus, the enzyme activity of TrxR gets hindered, which finally leads to mitochondrial damage. Applying this principle to the case of ligand mediated and complexation assisted assembly of Au nanoclusters, targeted killing of cancer cells by specifically causing mitochondrial damage seemed a possibility. This would not only introduce an organelle specific, luminescent anti-cancer nanodrug with therapeutic and diagnostic potential but would also address key issues like drug resistance, limited therapeutic efficacy at ultimate stages of diseases and selective targeting of cancerous cells. Although, deciphering the exact mechanism of action of Zn Au NCs and Au nanocrystals as nanodrugs require much deeper investigations, it may be proposed herein that the activities of Zn Au NCs and Au nanocrystals are due to plausible binding of partially oxidised Au (I) to the active site of TrxR. Since the clusters are stabilized by Tyr and MPA and the active site of TrxR contains thiol containing cysteine, it may be possible that dissociation of Tyr occurs to achieve stronger bonding of gold (I) to thiol group of cysteine.

This eventually leads to inhibition of TrxR and thereby affects consequential cellular process, which finally leads to cell death. Further, to highlight the involvement of TrxR in

mitochondrial damage, MTT assay was performed on non-cancerous cells (HEK cells) following treatment with nanocrystals and Zn Au NCs and the results were compared to that of Hela cells. TrxR is known to be upregulated in cancer cells in comparison to normal cells. Interestingly, the cytotoxic effect of Au nanocrystals and Zn Au NCs on Hela cells was much pronounced than that on HEK-293 cells (Fig. 5.12). This could be due to higher expression of TrxR in Hela cells than in HEK cells. A schematic illustration showing the plausible mode of interaction between Au nanocrystals and Zn Au NCs with TrxR is shown below (Scheme 1)[66]

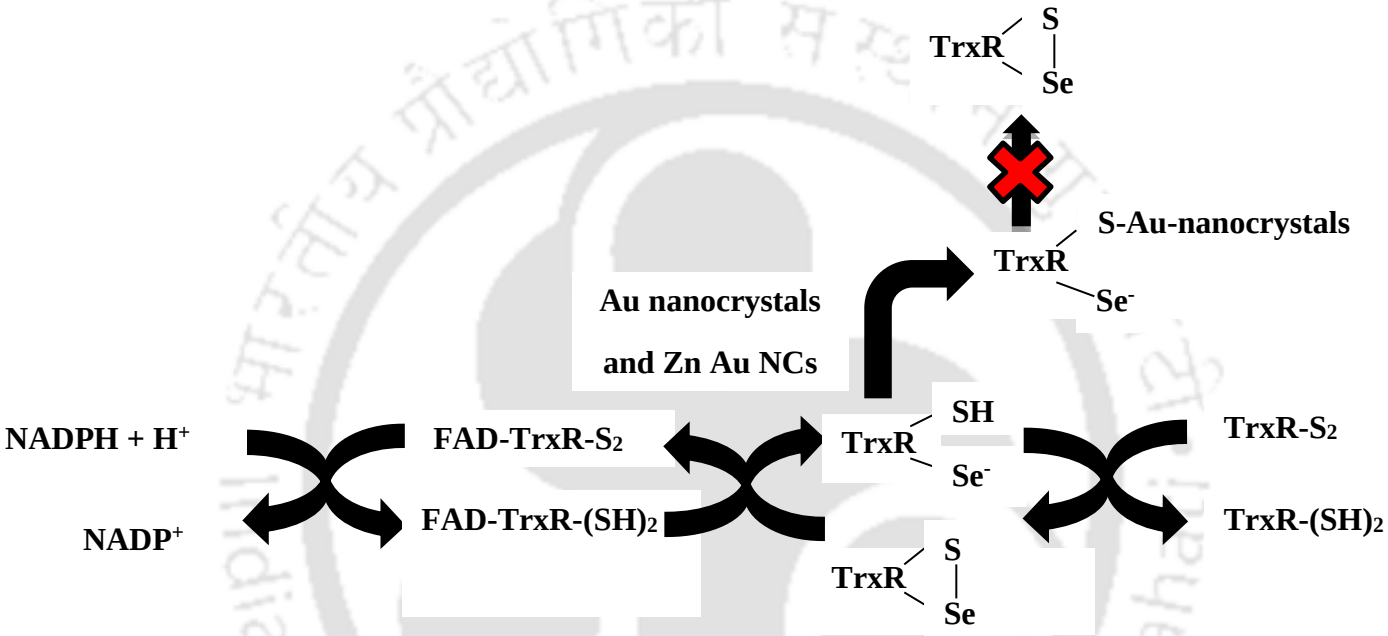

Scheme 1: A schematic illustration showing the plausible mode of interaction between Au nanocrystals and Zn Au NCs with TrxR.[66]

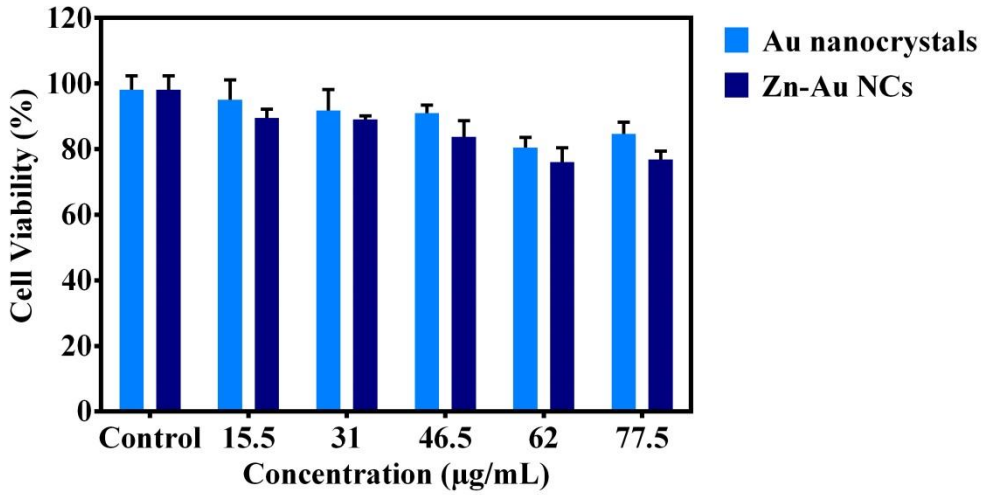

Fig. 5.12 MTT assay performed on HEK-293 cells following treatment with dispersion of Au nanocrystals and nanoclusters and the product of their reaction with zinc ions.

As already stated literature reports suggest the use of Au (I) complexes as mitochondria targeted anticancer agents.[2,3] Several studies have been performed to gain insight into the underlying mechanism of such mitochondria targeted anticancer activity of Au (I) complexes, which revealed preferential binding of Au (I) to thiol groups of thioredoxin reductase (TrxR). This inhibits the enzymatic action of TrxR, leading to consequential mitochondrial damage. A report investigating the detailed mechanism of action of gold complex based inhibitors of TrxR provides crystallographic evidences suggesting the replacement of chloride ion coordinated to gold complex by the thiol group of TrxR.[4] Similarly, in the case of tyrosine (Tyr) mediated assembly of Au nanoclusters, herein referred to as Au nanocrystals, the tyrosine moieties attached to the Au atoms are likely to be replaced by thiol groups (owing to labile nature of the former), which have stronger binding affinity towards Au atoms or Au (I) ions present on the surface of Au nanoclusters. The possibility of such ligand replacement is further supported by a report stating that insufficient thiol ligand stabilized Au nanoclusters may further interact with thiol containing ligands.[5] Another possible mode of interaction between Au (I) (of Au nanocrystals and Zn Au NCs) and TrxR could result from degradation of Au nanocrystals and Zn Au NCs in the presence of ROS. The nanocrystals disintegrated upon interaction with ROS could have exposed Au (I) on their surfaces, which might interact with thiol groups of TrxR.

Explanation for higher cytotoxic activity of Au nanocrystals in comparison to Zn Au NCs:

The extent of cellular uptake and hence the cytotoxic activity of a nanoparticulate drug is crucially determined by the free energy needed for "wrapping" of the same by cell membrane. This is defined by the thermodynamic drive of a particular entity to enter a cell. As per the studies of Warren et al.,[67] the size of a nanoparticle plays critical role in determining the extent to which it would be taken up by a mammalian cell. In an allied study, Gao et al.[68,69] have suggested that nanoparticles in the size range of ~ 55 nm produce sufficient free energy for endocytosis and thus undergo facile cellular uptake following effective wrapping by cell membrane. On the other hand, nanoparticles with size smaller than 50 nm are incapable of producing the amount of free energy required for complete wrapping of the nanoparticles within the surface of the cellular membrane and hence fail to undergo effective endocytosis. Thus, in order to undergo cellular uptake, smaller nanoparticles are clustered onto the surface of the cell to gain the optimum size required to meet the threshold thermodynamic driving force for endocytosis.

In the present study, Au nanocrystals typically were of 5-10 nm. Hence in order to meet the size criterion for endocytosis (~55 nm), Au nanocrystals are to be clustered on the surface of cell membrane. Hence, Au nanocrystals owing to their smaller sizes require an additional interaction among themselves to undergo endocytosis. On the other hand, as synthesised Zn Au NCs with size of ~50 nm need not go through such energy demanding clustering and hence are envisioned to undergo endocytosis in a more facile manner as compared to Au nanocrystals. This may possibly explain the difference between cytotoxic activity of Au nanocrystals and Zn Au NCs.

To this end, when Hela cells were incubated with 77.5 µg/mL of Au nanocrystals and Zn Au NCs for 24 h, 31% and 52% cell death was observed for Au nanocrystals and Zn Au NCs respectively. However, in order to check the long term cytotoxicity of Au nanocrystals and Zn Au NCs, Hela cells were treated with 77.5 µg/mL of Au nanocrystals and Zn Au NCs for 72 h and MTT assay was performed thereafter. The percentage cell death in case of Au nanocrystals was observed to be 28%, whereas in case of Zn Au NCs, percentage cell death was found to be 54% (Fig. 5.13, Table 5.2). Since the effect of Au nanocrystals and Zn Au NCs on Hela cells was found to be similar for incubation time of 24 h and 72 h, it may be concluded that Au nanocrystals and Zn Au NCs did not have any additional cytotoxic effect

on Hela cells. Hence the possibility of long term cytotoxic effect of Au nanocrystals and Zn Au NCs could presumably be ruled out. Also, as described in the subsequent section, the Au nanocrystals and Zn Au NCs get degraded in the presence of hydrogen peroxide and thus there is the possibility of clearance from the body. Thus long term cytotoxicity may not be there.

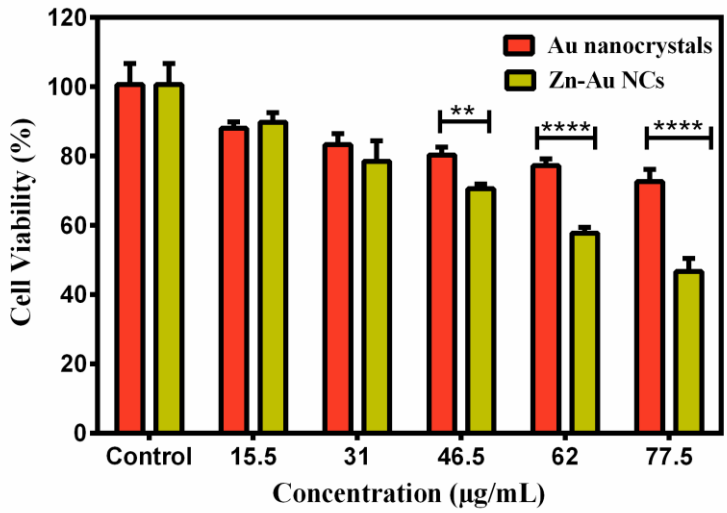

Fig. 5.13 MTT assay based cell viability of Hela cells treated with dispersion of Au nanocrystals and the Zn Au NCs for 72 h.

Table 5.2 A comparative tabulation of percentage cell death of Hela cells upon incubation with Au nanocrystals and Zn Au NCs for 24 h and 72 h.

Sample	Incubation time(h)	Percentage cell death
Au nanocrystals	24	31
	72	28
Zn Au NCs	24	52
	72	54

Further, cellular uptake study performed on HeLa cells revealed effective internalization of both Zn Au NCs and Au nanocrystals (Fig. 5.14). Enhanced luminescence

of Zn Au NCs compared to Au nanocrystals showed that cells treated with Zn Au NCs had bright red luminescence while those incubated with Au nanocrystals showed much weaker luminescence (with λ_{ex}-405 and λ_{em}-590). The corresponding depth projections are shown in Fig. 5.14.

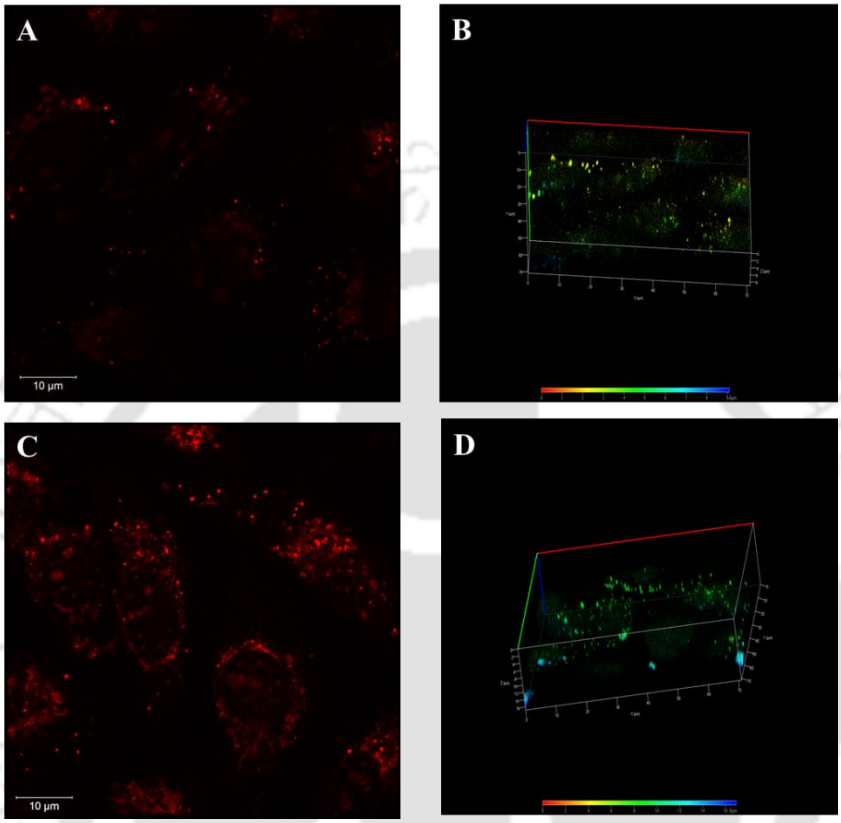

Fig. 5.14 Confocal laser scanning microscopic analysis of HeLa cells treated with (A) dispersion containing Au nanocrystals and nanoclusters (B) Depth projection analysis of HeLa cells treated with dispersion containing Au nanocrystals and nanoclusters. (C) Confocal laser scanning microscopic analysis of HeLa cells treated with zinc complex of Au nanoclusters and (D) Depth projection analysis of HeLa cells treated with dispersion containing Au nanocrystals and nanoclusters.

For ICP atomic emission spectrometric analysis, 5×10^5 of HeLa cells were seeded in 6 well plates and were kept for 24 h. The overgrown cells were treated with Au nanocrystals (77.5 µg/mL) and Zn Au NCs (77.5 µg/mL) for 6 h. Thereafter the cells were treated with 3% sub-boiled nitric acid for 2 h. Thereafter, the supernatant was collected and used for ICP atomic emission spectrometric analysis. As per the studies of Voliani et al., the amount of

ions internalized in cells provides a better probe for uptake studies.[23] In order to estimate the amount of gold and zinc ions internalized by HeLa cells following treatment with Au nanocrystals and Zn Au NCs, inductively coupled plasma atomic emission spectroscopy (ICP-AES) was performed. In case of Zn Au NCs, the amount of gold and zinc ions internalized by HeLa cells was estimated to be 0.046 ppm and 0.106 ppm, respectively. The presence of Au in the cells treated with Au nanocrystals could not be detected. The detection limit of the ICP atomic emission spectrometer used herein is 0.01 ppm. Hence, in case of Au nanocrystals, in same number of cells as that in case of Zn Au NCs (approximately), owing to lesser uptake of Au nanocrystals as compared to Zn Au NCs (due to size factor), the amount of Au (in Au nanocrystals) internalized by HeLa cells might have been less than 0.01 ppm and hence could not be estimated.

In order to investigate the effect of Au nanocrystals and Zn Au NCs on mitochondrial membrane potential damage, confocal laser scanning microscopy (CLSM) analysis was performed using 5,5',6,6' tetrachloro 1,1',3,3' tetraethylbenzamidazolylcarbocyanine iodide (JC-1) dye as a probe. JC-1 is a cationic dye, which shows mitochondrial potential based alteration of emission characteristics. In the normal range of mitochondrial membrane potential; it forms J aggregates, thereby exhibiting red emission. While, upon depolarization of the mitochondrial membrane, JC-1 fails to undergo J aggregation. Instead, it remains in its monomer form, which is associated with green emission. Thus, mitochondrial membrane potential damage was verified herein by incubation of HeLa cells with Zn Au NCs at the IC_{50} dose (as determined from MTT assay with the value being 77.5 µg/mL) and thereafter treatment with JC-1 dye. This was followed by investigation under CLSM in red and green emission channels, respectively. In an allied vein, untreated HeLa cells and HeLa cells treated with Au nanocrystals were also subjected to JC-1 staining. Interestingly, it was observed that while for untreated control cells, JC-1 dye exhibited pronounced red emission, for cells treated with Zn Au NCs, the emission was primarily green. This clearly indicated alteration of the mitochondrial membrane potential by Zn Au NCs, eventually leading to cell cytotoxicity. On a similar note, HeLa cells treated with Au nanocrystals following treatment with JC-1 dye resulted in emission from both green (λ_{ex}-488 and λ_{em}-530) and red (λ_{ex}-514 and λ_{em}-590) channels, indicating depolarization of mitochondrial membrane. It was evident that green emission from JC-1 dye incubated with cells treated with Zn Au NCs was greater than those treated with Au nanocrystals (Fig. 5.11 B). This further substantiated the MTT results indicating higher therapeutic efficacy of Zn Au NCs than Au nanocrystals. Also, it

was anticipated that mitochondrial membrane potential alteration should ideally cause heightening of reactive oxygen species (ROS) in the cells. Thus, flow cytometry (FACS) analysis was performed using 2',7' –dichlorofluorescein diacetate (DCFH-DA) dye in order to quantitate ROS generated upon treating HeLa cells with Zn Au NCs and Au nanocrystals. Interestingly, ROS generated in the presence of Au nanocrystals was higher in comparison to that of untreated (control) HeLa cells but lower in comparison to Hela cells treated with Zn Au NCs (Fig. 5.15). This was further supported by MTT assay and results of JC-1 staining experiments. It is important to note here that Au nanocrystals and the corresponding zinc complex showed little toxicity to non-cancerous HEK-293 cells (Fig. 5.13).

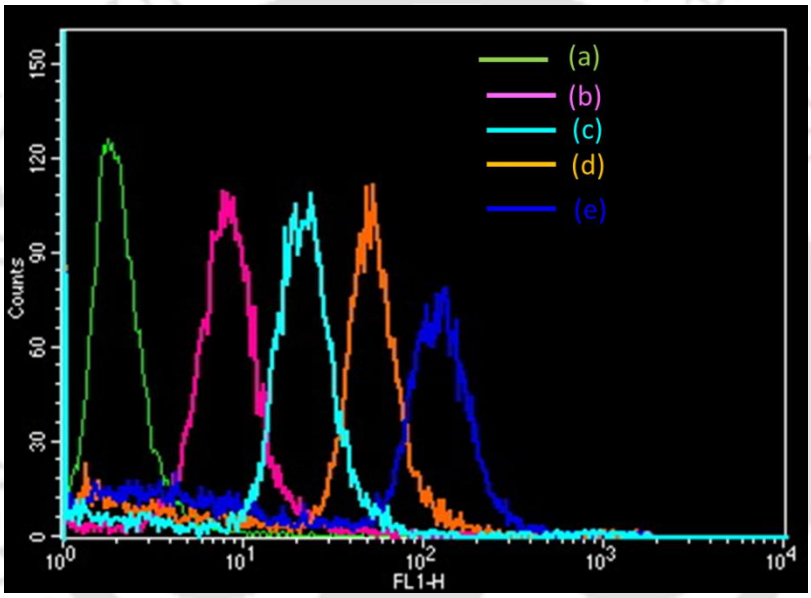

Fig. 5.15 FACS analysis showing ROS generation. (a) Untreated HeLa cells and HeLa cells treated with (b) 42 μg/mL and (c) 77.5 μg/mL of dispersion containing Au nanoclusters and Au nanocrystals. FACS analysis showing ROS generation of HeLa cells upon treatment with (d) 42 μg/mL and (e) 77.5 μg/mL of zinc complex of Au nanoclusters.

The specific localization of Au nanocrystals and Zn AuNCs within mitochondria was confirmed by CLSM analysis. In order to demonstrate this, Mito tracker green was used as a probe. As observed in Fig. 5,16, the red luminescence obtained from Au nanocrystals and Zn Au NCs (λ_{ex}-405 and λ_{em}-590) overlapped with the green fluorescence from Mito tracker green (λ_{ex}-488 and λ_{em}-530).

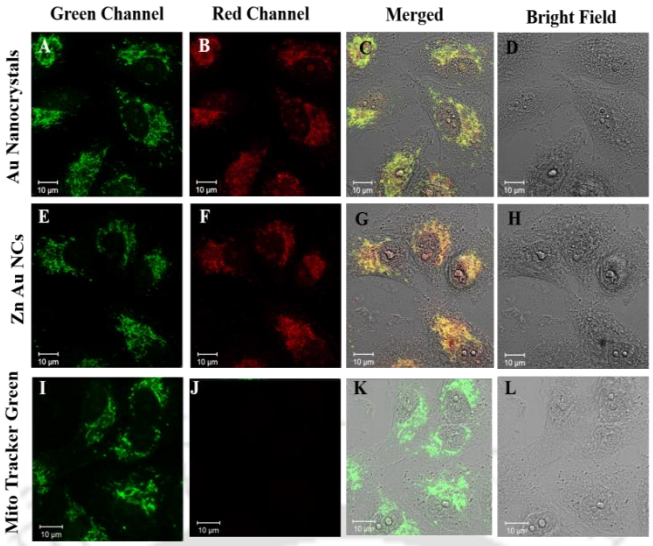

Fig. 5.16 CLSM images of HeLa cells incubated with Au nanocrystals and Mito tacker green acquired in (A) green channel (B) red channel, (C) merged images of (A) and (B). (D) Corresponding bright field image. CLSM images of HeLa cells incubated with Zn Au NCs and Mito tacker green acquired in (A) green channel (B) red channel, (C) merged images of (A) and (B). (D) Corresponding bright field image. CLSM images of Hela cells incubated with Mito tracker green (only) acquired in (A) green channel (B) red channel, (C) merged images of (A) and (B) and (D) corresponding bright field image.

However, Au nanoclusters synthesized using water soluble amino acid like histidine,[24] unlike tyrosine in the present case (which leads to ligand assisted crystallization of nanoclusters) were also analyzed under confocal microscope in presence of Mito Tacker green. Interestingly, in this case, the luminescence from the clusters seemed to appear from the entire cell and not specifically from the region probed with Mito tracker (Fig. 5.17). This clearly highlights the specificity of tyrosine attached nanocrystals and their zinc complex analogue towards mitochondria eventually leading to mitochondria targeted cell death. A plausible mechanism of anticancer activity of assembled Au nanoclusters (both zinc mediated and tyrosine mediated) has been proposed based on inhibition of thioredoxin reductase (TrxR), an enzyme present in mitochondria and which is known to be upregulated in cancer cells. Gold complexes are known to inhibit TrxR by preferential binding with the active site. [70,71] Also, Au nanoclusters are known to consist of atoms with Au (I) oxidation state. [72] Thus it may be possible that Au (I) on Au nanoclusters binds with the active site of TrxR in manner

akin to gold complexes thereby rendering the latter inactive and thus leading to mitochondrial damage.

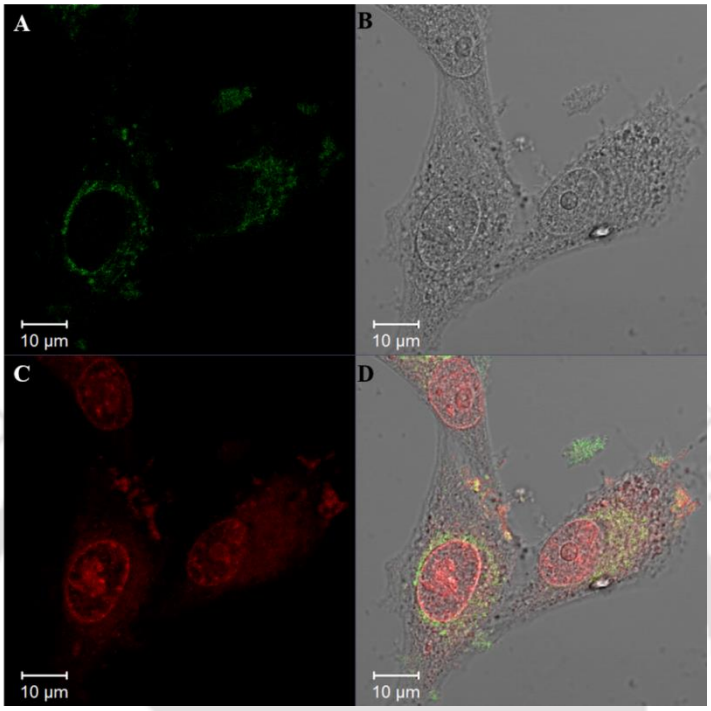

Fig. 5.17 CLSM images of Hela cells incubated with Au nanoclusters (stabilized with histidine and mercaptopropionic acid) and Mito tracker green acquired in (A) green channel, (B) corresponding bright field image, (C) acquired in red channel, (D) merged images of (A) and (C).

Confocal laser scanning microscopic (CLSM) analysis revealed the localization of Au nanocrystals and Zn Au NCs within mitochondria. This has been achieved using Mito tracker and JC-1 dye as probes. Also, as mentioned above, generation of reactive oxygen species (ROS) was observed in the presence of Au nanocrystals and Zn Au NCs. This could be attributed to alteration of mitochondrial membrane potential. Hence the observed cell death upon treatment of Hela cells with Au nanocrystals and Zn Au NCs was ascribed to mitochondria targeted therapeutic potential of the Au nanocrystals and Zn Au NCs. To this end, experiments were performed to elucidate the effect of ROS on the chemical stability of Au nanocrystals and Zn Au NCs, which could easily be probed by recording the luminescence of the crystalline assemblies. Interestingly, the luminescence of Au nanocrystals and Zn Au NCs was significantly quenched upon addition of H_2O_2 (Fig. 5.18 A-

B). This was indicative of structural disruption of the nanocrystals leading to possible degradation of the assemblies into their constituents. The structural deformation of Au nanocrystals and Zn Au NCs was further confirmed by transmission electron microscopic (TEM) analysis. Dispersions of Au nanocrystals and Zn Au NCs added with H_2O_2 were analysed by TEM. Intriguingly, such analysis revealed the presence of a large number of smaller particles (2-3 nm) in addition to initially formed larger Au nanocrystals (~10 nm), which might have been formed by degradation of Au nanocrystals upon reaction with H_2O_2. The presence of still larger particles (~10 nm) could be due incompletion of reaction between the nanocrystals and H_2O_2. The lack of crystallinity of smaller particles was confirmed by electron diffraction (Fig. 5.19 A-F). In an allied vein, TEM analysis of Zn Au NCs treated with H_2O_2 revealed the formation of featureless smaller particles (6 -10 nm) with low crystallinity (Fig. 5.20 A-F). In this case also, the presence of a small population of larger particles (~ 20 nm) was observed and could be due to the fact the reaction between Zn Au NCs and H_2O_2 was yet to reach completion. Given the observation that these nanocrystals generate ROS in cellular environment, degradation of the nanocrystals into smaller particles in presence of oxidizing species under allied condition within cellular environment, offers a possible route to clearance of these species - thus avoiding the possibility of deposition in organs like liver and spleen. Such approach of using small sized nanoscale particles, keeping their theranostic potential unaffected, is deemed important for clinical use of the same. This is also substantiated by a detailed study performed by Voliani et al.[73]

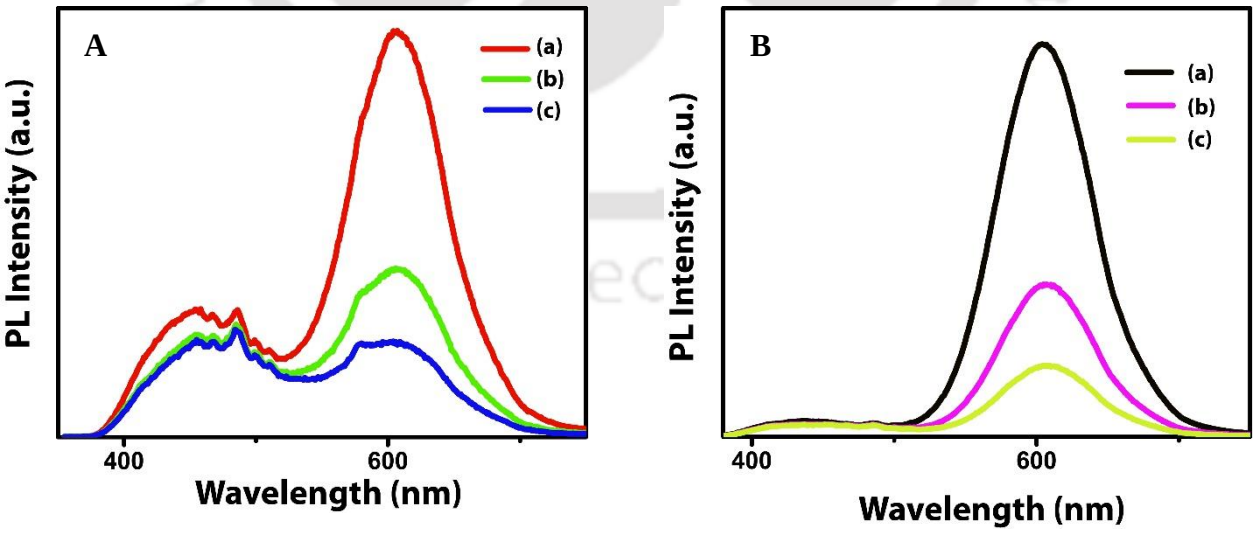

Fig. 5.18 (A) Luminescence spectrum of (a) Au nanocrystals and that following treatment with (b) 100 µL hydrogen peroxide and (c) 200 µL hydrogen peroxide. **(B)** Luminescence

spectrum of (a) Zn Au NCs and that following treatment with (b) 100 µL hydrogen peroxide and (c) 200 µL 37.2 % hydrogen peroxide.

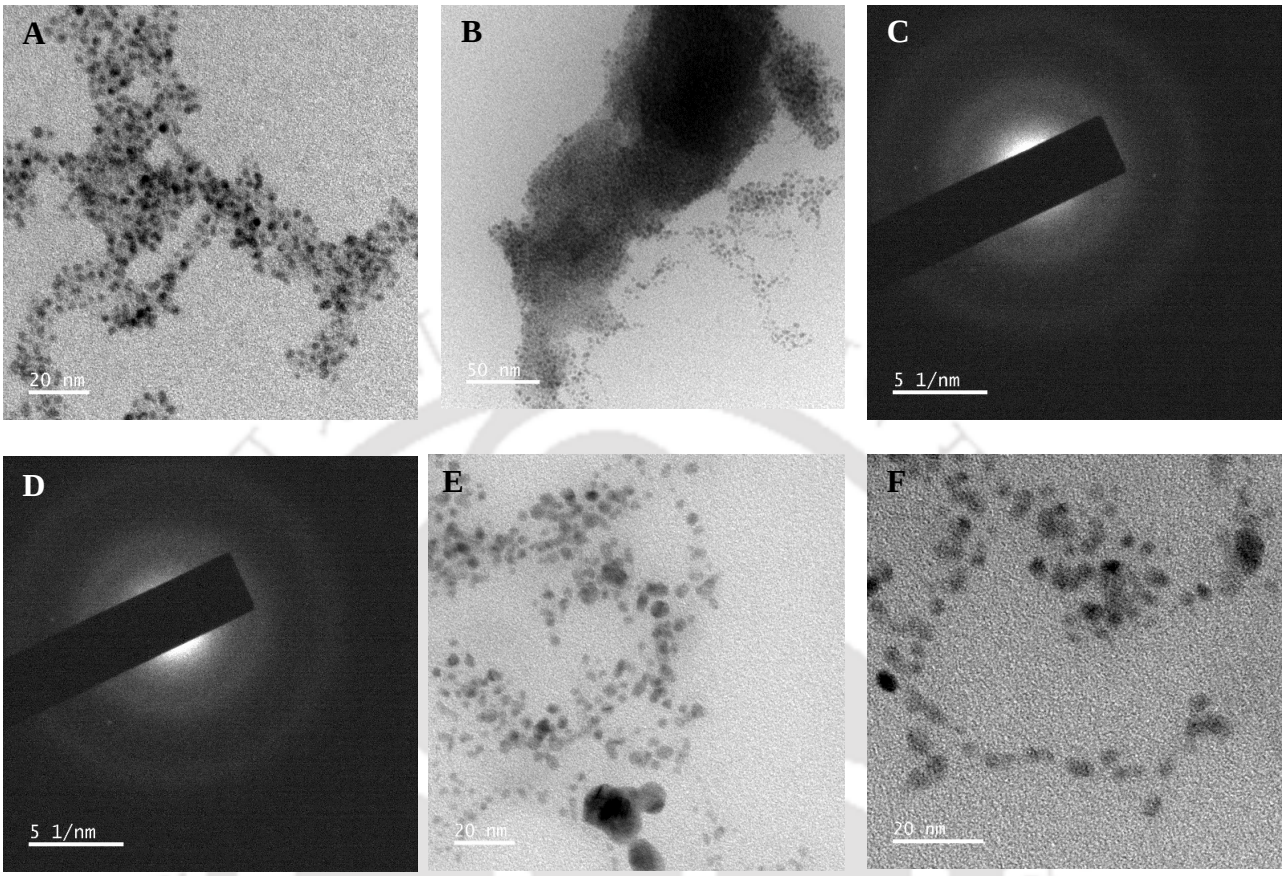

Fig. 5.19 Transmission electron microscopic (TEM) images of **(A-B)** products of reaction of Au nanocrystals with hydrogen peroxide. These images have been collected in different areas of the TEM grid. **(C-D)** Corresponding selected area electron diffraction (SAED) images. **(E-F)** Additional TEM images of product of reaction of Au nanocrystals with hydrogen peroxide acquired on various areas of the TEM grid.

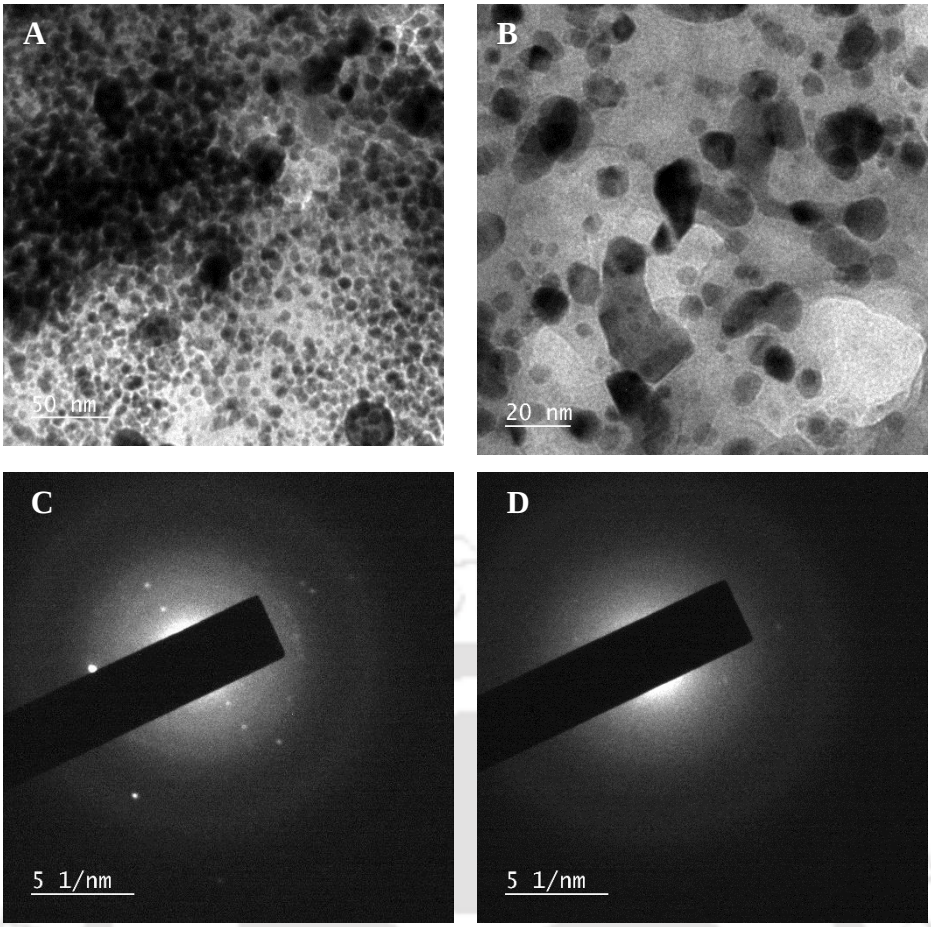

Fig. 5.20 Transmission electron microscopic (TEM) images of **(A-B)** product of reaction of Zn Au NCs with hydrogen peroxide. These images have been collected in different areas of the TEM grid. **(C-D)** Selected area electron diffraction (SAED) images acquired on typical particles.

Further for practical applicability, we have recorded the luminescence of Au nanocrystals and Zn Au NCs for an interval of 24 h. It was observed that the luminescence of Au nanocrystals remained almost unaltered and the luminescence of Zn Au NCs was negligibly attenuated. Further, we have also measured the stability of Au nanocrystals and Zn Au NCs in human blood serum. The luminescence spectra of Au nanocrystals and Zn Au NCs were recorded in human blood serum for an interval of 24 h. While no discernible change was observed in the luminescence spectrum of Au nanocrystals upon incubation in human blood serum for 24 h, a little enhancement in luminescence of Zn Au NCs was observed after 24 h (Fig. 5.21). Also, any structural and size deformation of Au nanocrystals and Zn Au NCs would had caused significant change in their luminescence properties. As no such discernible alteration in luminescence characteristics of Au nanocrystals and Zn Au NCs was observed, it could be stated that human blood serum (comprising majority of biological constituents of the circulating system) might not have any consequential effect on the structural properties of the crystals. This was further confirmed by performing TEM analysis

of the nanocrystals following incubation with human blood serum. TEM analysis revealed that the nanocrystals retained their integrity in the blood serum (Fig. 5.22 A-F).

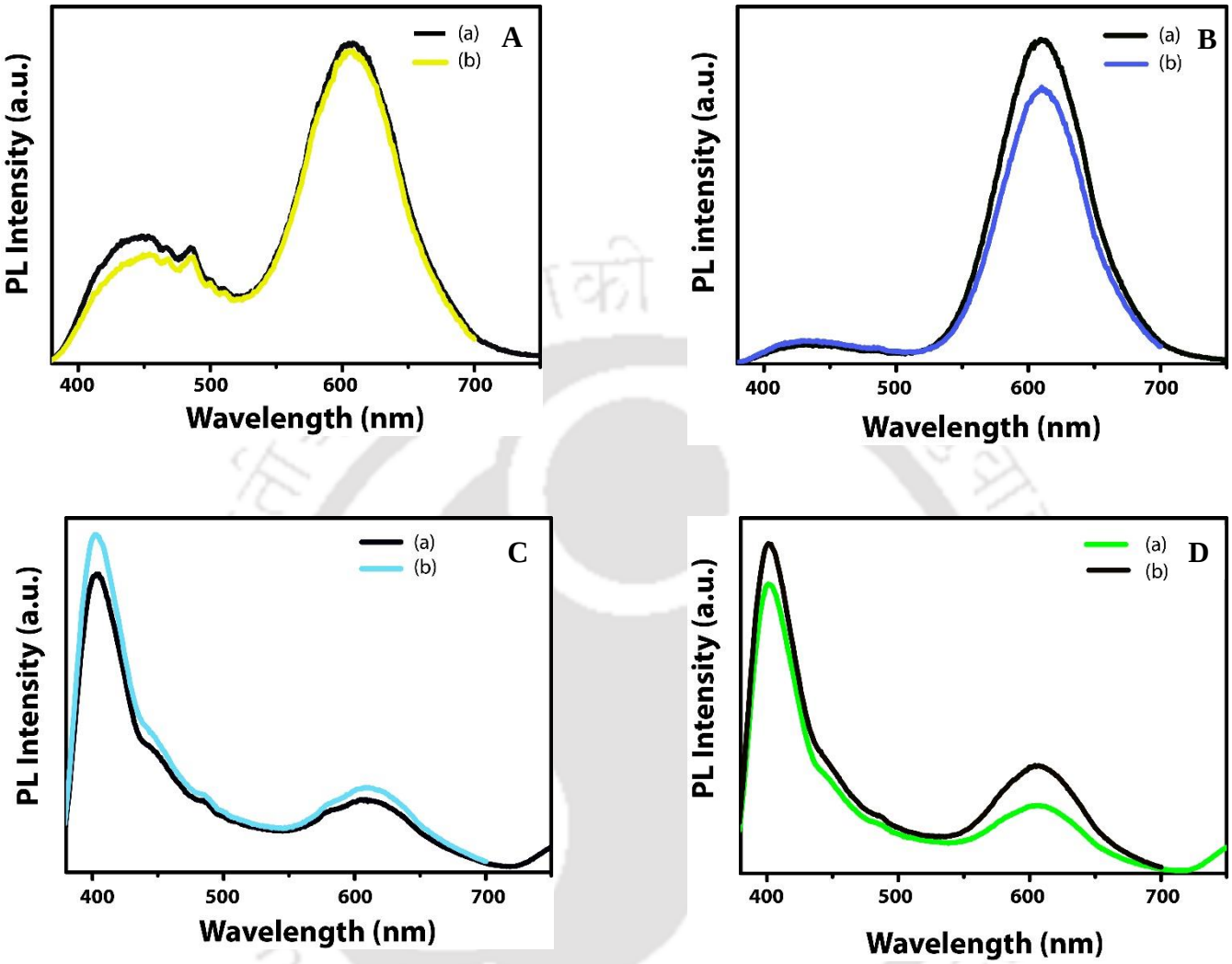

Fig. 5.21 (A) (a) Luminescence spectrum of Au nanocrystals acquired initially and that (b) after 24 h. **(B)** Luminescence spectrum of Zn Au NCs acquired initially and that (b) after 24 h. **(C)** (a) Luminescence spectrum of Au nanocrystals incubated in human blood serum acquired initially and that (b) after 24 h. **(D)** Luminescence spectrum of Zn Au NCs in human blood serum acquired initially and that (b) after 24 h.

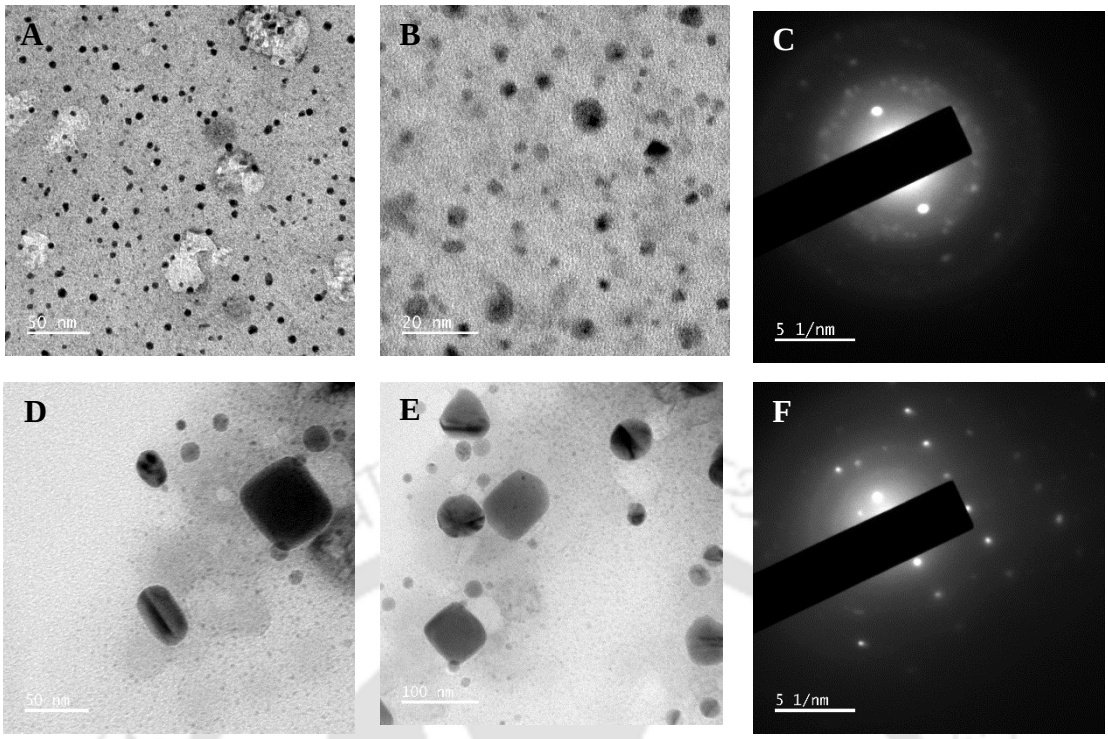

Fig. 5.22 (A-B): TEM images of Au nanocrystals incubated with human blood serum. **(C)** SAED image acquired for a typical particle. **(D-E)** TEM images of Zn Au NCs incubated with human blood serum. **(F)** SAED image acquired for a typical particle.

5.3 Conclusion

In a nutshell, we have reported that assembled atomic clusters of Au (i.e., Au_{14}) in the forms of nanoscale particles led to killing of cancer cells. Moreover, the single crystalline particles formed in the presence of Zn^{2+} i.e., Zn Au NCs had exhibited higher efficiency as an anticancer agent in comparison to the solvent driven assembly. Further MTT assay, FACS analysis and JC1 staining experiments revealed that the therapeutic potential of Zn Au NCs was much higher than Au nanocrystals. The nanocrystals of Au nanoclusters formed by either of the strategies mentioned above exhibited mitochondria targeted efficacy with regard to cancer therapy. Also, the use of crystalline particles with size in nanometer range offers an additional advantage of possible renal clearance (upon disintegration in the process). The principle of assembling nanoclusters via chemical reaction, as demonstrated herein does not only open up newer routes for hierarchical organization of atomic clusters but also confers Au nanoclusters with important new properties having application potential.

Chapter 6

Crystalline Nanoscale Assembly of Gold Clusters for Reversible Storage and Sensing of CO_2 via Modulation of Photoluminescence Intermittency

We report that zinc mediated crystalline nanoscale assembly of atomic gold nanoclusters (NCs) were able to reversibly store gaseous carbon dioxide with adsorption capacity of 1.79 mM g^{-1} at 20 ˚C and 20 bar. Importantly, carbon dioxide induced reversible change in the photoluminescence intermittency of the clusters in the assembly helped in indication of the storage using confocal laser scanning microscopy. Briefly, Au_{14} NCs, having a single valued "on" time, exhibited a wide distribution of "off" time blinking profile that could be fitted with truncated power law. However, the blinking of ligand stabilized Au_{14} NCs was eliminated following the formation of zinc ion mediated three dimensional crystalline assembly of Au_{14} NCs. In the presence of carbon dioxide, the single crystalline assembled nanoclusters showed intermittency behavior of the original clusters. However, upon desorption of carbon dioxide, the non-blinking nature of the crystalline assembly was restored.

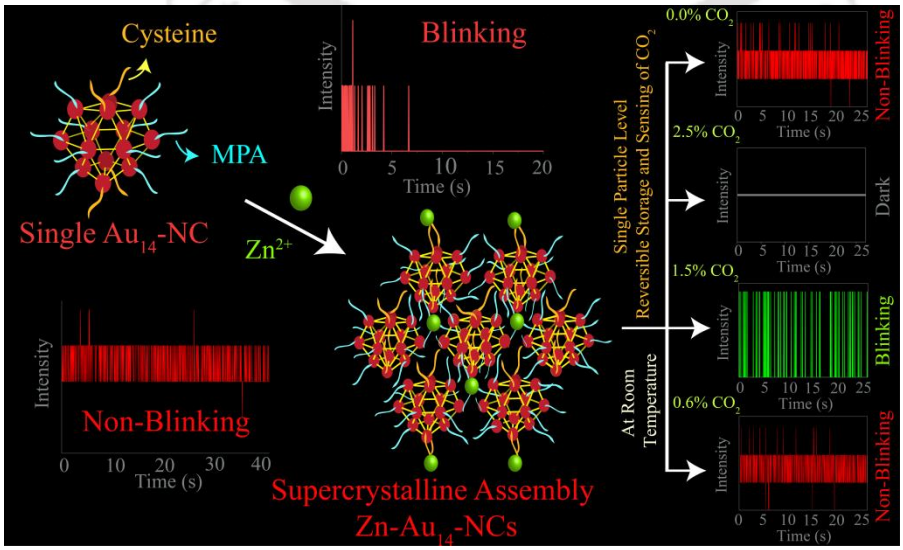

Basu et al. J. Mater. Chem. C, Just Accepted Manuscript. Reproduced following rules of Royal Society of Chemistry. Copyright belongs to J. Mater. Chem. C, RSC

6.1 Experimental Section

Chemicals: Tetrachloroauric acid ($HAuCl_4$), mercaptopropionic acid (MPA), L cysteine (Cys), D tryptophan (Trp), histidine (His) and potassium bromide were procured from Sigma Aldrich. Zinc acetate dihydrate was purchased from Merck. All chemicals were used as received without further purification.

Synthesis of Cys-Au_{14} NCs: 5.0 mL methanol and 5.0 mL water were taken in a beaker. To the mixture, 1.0 mL of $HAuCl_4$ was added followed by 0.4 mL MPA. The resultant mixture was added with 2.0 mg L-Cys and further stirred for ~5 min. This led to formation of a dispersion, which was luminescent upon excitation at 355 nm. The dispersion was centrifuged at a speed of 10,000 rpm for 10 min. The so obtained pellet was redispersed in water and used for further experiments.

Synthesis of Zn-Cys-Au_{14}-NCs: Cys Au_{14} NCs (prepared using the method as mentioned above) was redispersed in 1.0 mL water and further 50.0 mg of Zn acetate dihydrate was added into that. This led to formation of a dispersion with higher luminescence in comparison to only Cys Au_{14} NCs. The dispersion was centrifuged at a speed of 10,000 rpm for 10 min. The so obtained pellet was redispersed in water and used for further experiments.

Confocal microscopic measurements and blinking analysis: Confocal imaging and single particle experiment of Au_{14} NCs and their Zn-Au_{14}-NCs crystalline assembly (followed by depositing their diluted dispersions on glass cover slips of thickness 0.17 mm) were analyzed by using Carl Zeiss LSM-880 confocal laser scanning microscope. This was equipped with a 355 nm diode-pumped solid-state UV laser for excitation and Apochromat ,63X, NA 1.40, oil- immersion objective for imaging. The GaAsP detector and Airyscan detector were used to collect the data from the single particle experiments. The binning time of 27 ms with maximum laser power of excitation fixed at 63mW for a time duration of 20-40 s were used to record blinking profile and video of single particles of Au_{14} NCs and their Zn-Au_{14}-NCs crystalline assembly. The ZEN black software was used to analyze the so obtained images and blinking data.

Calculation of probability density distributions of off states of Au_{14} NCs: The following equation was used to calculate the probability densities of off states for particles consisting of Au_{14} NCs. $\rho_i(t) = \frac{N_i(t)}{N_{total}} \times \frac{1}{\Delta t_{i,av}}$, (i=off) Where ρ_i is the probability density of *off* events at

time t, $\Delta t_{i,av}$ is average of the time intervals to the events, N_i is the number of *off* events and N_{total} is the total number of events. α_{off} distributions can be fitted to the truncated power law: $\rho_i(\tau) = A_i \tau^{-\alpha_i} \exp(-\mu_i \tau)$; where A_i = amplitude, α = power law exponent and μ = saturation rate.

Carbon dioxide adsorption analysis: In order to perform CO_2 adsorption analysis, 79.2 mg of Zn Cys Au NCs was degassed at a temperature of 90 ˚C. Thereafter, CO_2 adsorption analysis was performed using isorbHP1-XKRL SPN100 by varying the target pressure from 0.25 bar to 20 bar and back.

6.2 Results and discussions

The details of the synthesis of (i) Au_{14} NCs, stabilized by the combination of mercaptopropionic acid (MPA) and cysteine (Cys) and (ii) their corresponding Zn^{2+} mediated crystalline assembly are described in the experimental section. It may be mentioned here that facile complexation reaction involving zinc ion and the carboxylate or amine group of the ligand stabilizing the clusters, along with the anticipation of useful application of the crystalline assembled nanoclusters, led us to carry out the present work. Cys-Au NCs were luminescent (λ_{em}-590 nm) upon UV excitation (Fig. 6.1).

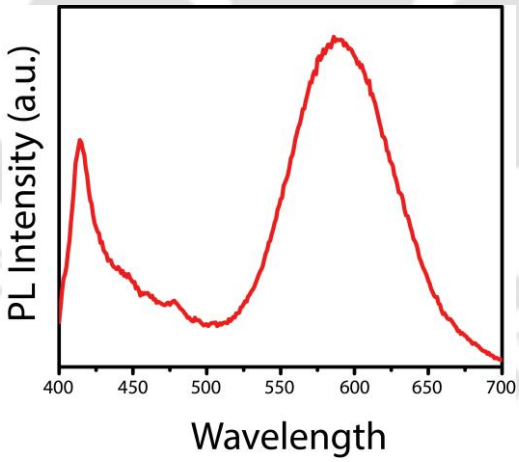

Fig. 6.1 Emission spectrum (λ_{ex} - 355 nm) of the as-synthesized Cys-Au_{14} NCs.

The origin of the aforementioned emission (at 590 and 425 nm) in the luminescence spectra of Au NCs is described as follows (Fig. 6.2).

Origin of luminescence in Cys-Au NCs. The origin of the emission at 590 nm is likely to have occurred from a metal ligand emission state. As per studies of Goodson and co-workers relaxation pathway in a typical cluster primarily involves five states:

(i) A ground state

(ii) A core state (akin to excited state in case of molecular fluorophores)

(iii) An intermediate state associated with the core state

(iv) A dark state

(v) A metal-ligand emission state

In a typical relaxation process, following excitation from the ground state to the core state, the system initially relaxes to an intermediate state. This relaxation is often referred to as "fast relaxation" and occurs on an ultrafast time scale. At this stage, three possibilities exist:

(i) A fast emission to the ground state referred to as "fast core emission".

(ii) Transition to a dark state. Relaxation from the above mentioned intermediate state to the dark state has been proposed to occur via intracluster non-radiative transitions.

(iii) Transition to an emissive metal ligand state.

However, this emission is proposed to have originated from the ligands stabilizing the clusters and has no direct contribution from the clusters. It may be noted that the ligands stabilizing the clusters are amino acids (cysteine, histidine and tryptophan) in all three cases. Thus, their intrinsic emission is likely to be preserved even after coordination to the Au atoms of the clusters. In order to establish this statement, we have performed control experiments of cysteine, tryptophan and histidine. Interestingly, in all three cases, the emission at ~410 nm with a sharp feature at 400 nm could be observed (Fig. 6.2). It is to be noted here that the variation in intensity is attributed to the different concentration of the amino acids used during measurement.

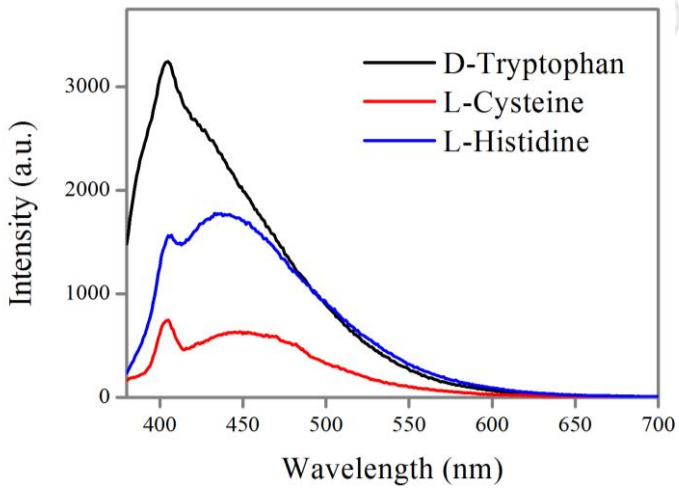

Fig. 6.2 Emission spectra of L-cysteine, L histidine and D tryptophan. λ_{exc} was set at 355 nm.

Transmission electron microscopic (TEM) image showed that Cys-Au NCs had average particle size of 2.5 nm and devoid of crystalline characteristics (Fig. 6.3).

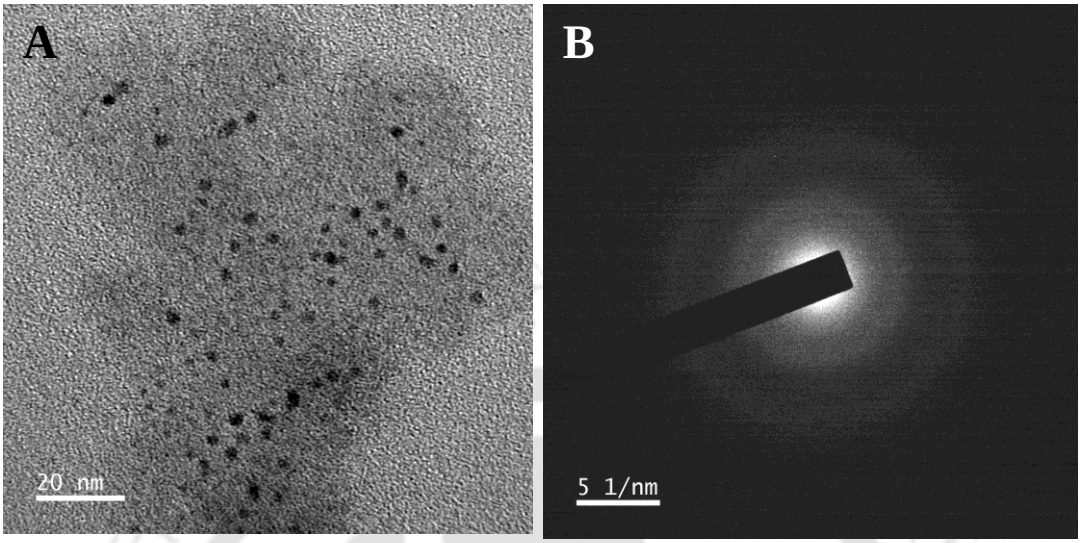

Fig. 6.3 (A) Transmission electron microscopy (TEM) image and **(B)** selected area electron diffraction (SAED) pattern of the as-synthesized Cys-Au_{14} NCs.

Additionally, the successful formation of Cys-Au NCs was indicated by the absorption spectrum (which did not exhibit any characteristic peak due to plasmon active Au nanoparticles; Fig. 6.4).

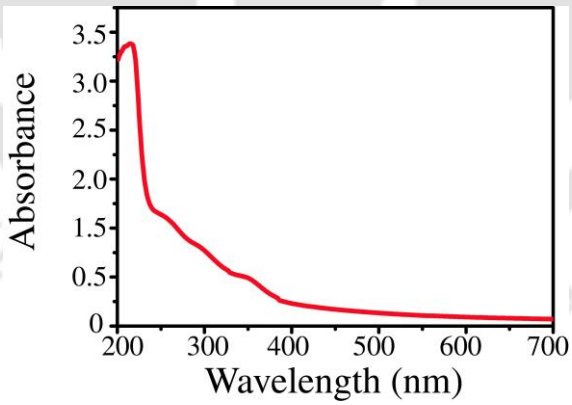

Fig. 6.4 Absorption spectrum of the Cys-Au_{14} NCs.

Electrospray mass spectrometric analysis (ESI-MS) clearly showed the presence of a peak at 1449.80 due to the formation of Au_{14} NCs with molecular formula of Au_{14}-MPA_{10}-Cys_4 (Fig. 6.5 and Table 6.1).

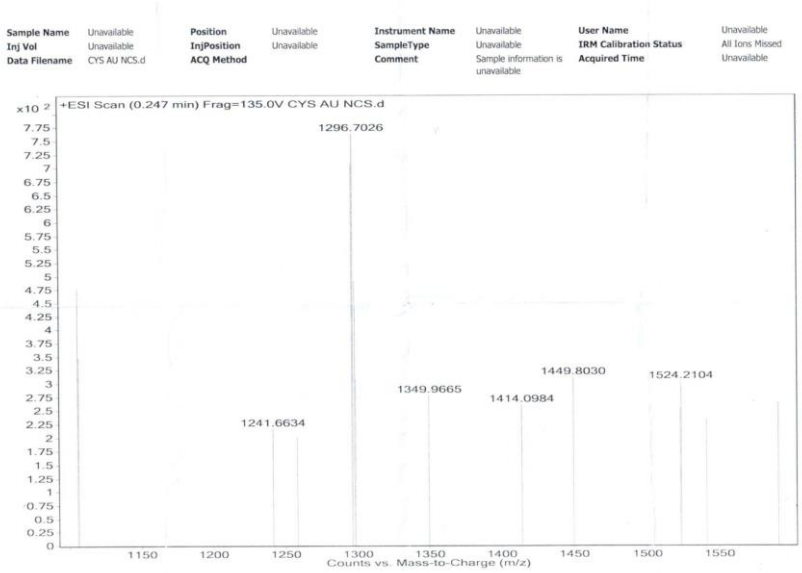

Fig. 6.5 Electrospray Ionization mass spectrum (ESI-MS) of Cys-Au_{14} NCs.

Table 6.1 Mass fragments corresponding to the observed peaks in ESI-MS of the as-synthesized Cys-Au_{14} NCs. This clearly indicated the successful formation of Au_{14} NCs with the molecular formula $Au_{14}MPA_{10}Cys_4$.

Peak position	Component
1449.80	$[Au_{14}MPA_{10}Cys_4 +3\ Na^+]^{3+}$
1241.66	$[Au_{14}MPA_4Cys_4 +3\ Na^+]^{3+}$
1414.09	$[Au_{14}MPA_9Cys_4 +3\ Na^+]^{3+}$
1296.70	$[Au_{14}MPA_9Cys +3\ Na^+]^{3+}$
1349.96	$[Au_{14}MPA_{10}Cys_2 +3\ H^+]^{3+}$
1524.21	$[Au_{14}Cys_2 +2\ Na^+]^{2+}$

Similarly, other two Au_{14} NCs stabilized by combination of (i) MPA and tryptophan (Trp) and (ii) MPA and histidine (His), exhibited emission maximum at 590 nm (Fig. 6.6) were synthesized according to our earlier reported methods. These two Au_{14} NCs are termed hereafter as Trp-Au_{14} and His-Au_{14} NCs.[74,75]

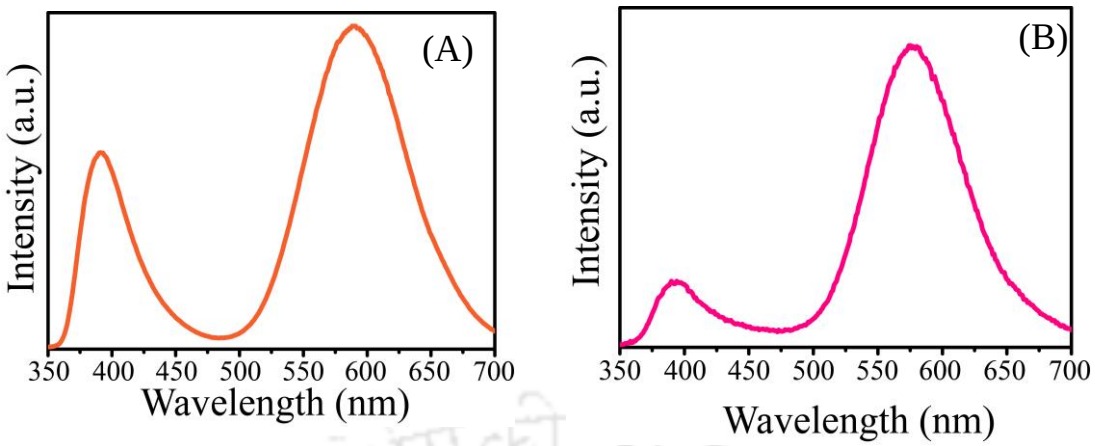

Fig. 6.6 Emission spectra (λ_{ex} - 355 nm) of the as-synthesized (A) Trp-Au_{14} NCs and (B) His-Au_{14} NCs.

The behavior of all three different Au_{14} NCs (Cys-Au_{14}, Trp-Au_{14} and His-Au_{14}), was confirmed by observing their blinking characteristics using CLSM under super resolution mode (with 355 nm laser). Fig. 6.7 A1, Fig. 6.7 B1 and Fig. 6.7 C1 depict the representative super resolution CLSM images of Cys, Trp and His stabilized Au_{14} NCs, respectively. Importantly, the blinking profiles of all three Au_{14} NCs were recorded for particles (consisting of Au_{14} NCs) as marked with a yellow serrated circle (Fig. 6.7). The blinking activities of three different Au_{14} NCs (as marked in Fig.6.7) were observed to have larger numbers of *off* states as compared to the *on* states. Importantly, the photobleaching of the clusters occurred with an abrupt drop of intensity to background level (Fig. 6.7), while gradual photobleaching was noticed for aggregated Au_{14} NCs (Fig. 6.8).

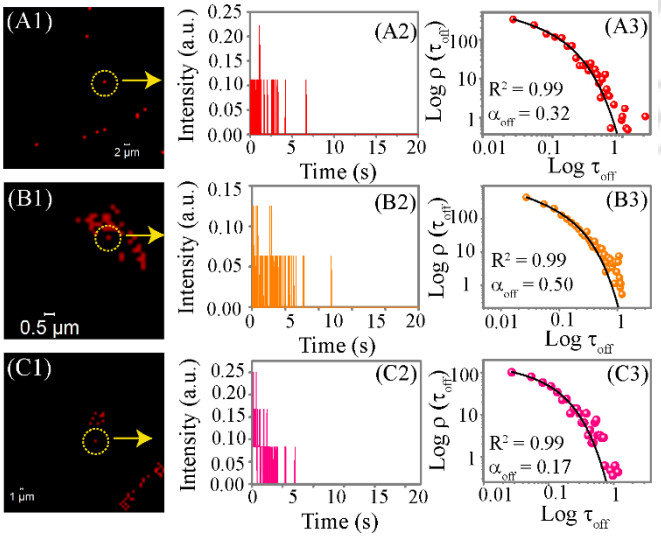

Fig. 6.7 (A) Confocal laser scanning microscopic images and **(B)** time dependent photoluminescence intermittency profiles (which was recorded against a particle as marked

for each image in Fig. 1A) and **(C)** distribution of *off* times of as-synthesized (1) Cys-Au_{14}, (2) Trp-Au_{14} and (3) His-Au_{14} NCs, respectively.

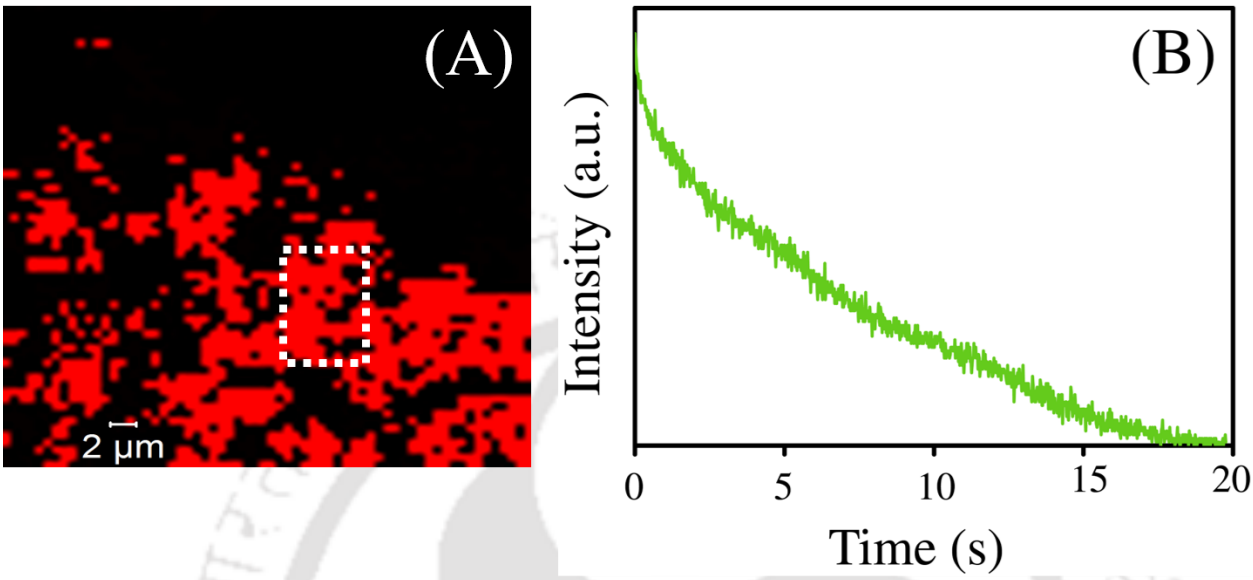

Fig. 6.8 (A) Confocal laser scanning microscopic image and (B) time dependent photoluminescence intermittency profile (which was recorded against marked portion in Fig. S6A) of aggregated Cys-Au_{14} NCs. The blinking profile was recorded using a fixed binning time of 27 ms and with excitation power of 63 mW (wavelength of 355 nm) for a time span of 20 s.

These results suggested that the intermittency was possibly due to single particle of Au_{14} NCs in all three cases.[76] However, considering the sizes observed in TEM images, the presence of multiple clusters in these particles cannot be ruled out. As mentioned above, it is plausible that particles were agglomerated when evaporated for the CLSM measurements. The size of the aggregated particles might be much larger than the single clusters. Thus the emission from agglomerated clusters (the intensity of which might have been much higher than individual clusters) might have led to the appearance of an apparent size much larger than the laser spot size. Further, the evidences of the (i) possible single particle nature, (ii) quantum yield at single particle level and (iii) ruling out the interference of the detector noise with blinking of Cys-Au NCs are given below (Fig. 6.9-6.14 and Table 6.2).

Control experiments and explanations to eliminate the interference of detector noise in the intermittency signals of Cys Au NCs

In the CLSM model used for pursuing the current study (Zeiss LSM 880), range indicator is used to specify the area of luminescence and that of background in a particular frame of measurement. By default, red portions indicate non-zero or high pixel values and blue portions are indicative of zero pixel values.

Also, in the confocal setup (LSM 880), gain master is adjusted to maximize the signal to noise ratio in a particular measurement. Herein, an optimized gain master of value 833 has been used to eliminate the background noise and acquire noise free images. Thus we have recorded a CLSM image of the background (recorded without inserting any sample), at a gain master of 833, with the range indicator being enabled. In an allied vein, we have recorded the CLSM image of Cys Au NCs along with background with the range indicator enabled. Interestingly, while in case of the background (only) the entire frame appeared blue indicating no detectable signal (Fig. 6.9 A-B), in case of Cys Au NCs, the area comprising of the clusters appeared red and the background (where absence of clusters was anticipated) appeared blue (Fig. 6.9 C-D).

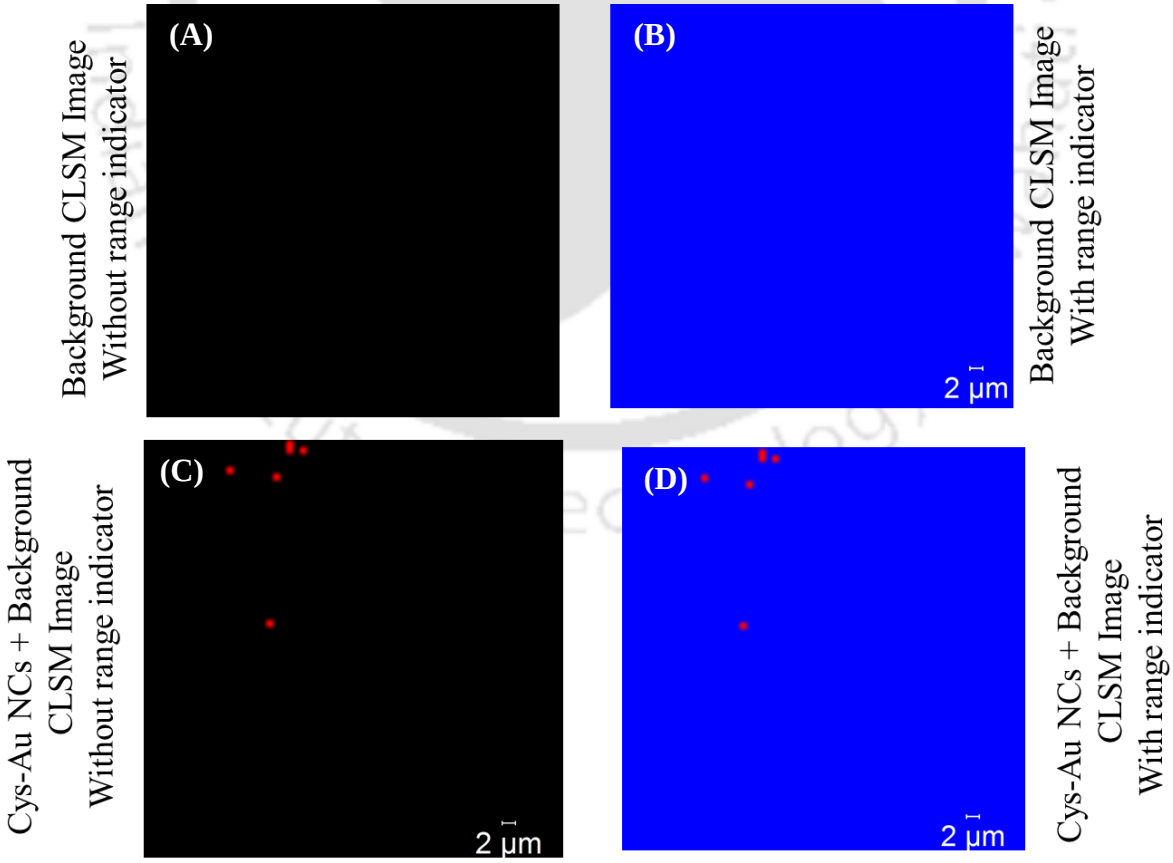

Fig. 6.9 (A) Confocal laser scanning microscopic image of a background (recorded without inserting any sample). **(B)** Corresponding image of background with range indicator being enabled. **(C)** Confocal laser scanning microscopic image of Cys Au NCs in presence of background **(D)** Corresponding image Cys Au NCs in presence of background with range indicator being enabled.

Secondly, in order to establish that the reported images and the blinking profiles are typical signatures of the luminescent clusters, we have acquired the luminescent spectrum on a typical particle of Cys Au NCs. Similarly, we have acquired the spectrum of the background in the same frame as that of the clusters. It is worthy to be mentioned here that the acquisitions have been done at a gain master value of 833. This value was optimized to completely eliminate the interference of background. Details of the optimization process is discussed in the subsequent section. Interestingly, in case of clusters, the spectrum matched exactly with that of the solution phase, exhibiting an emission maximum at 589 nm. On the other hand, the spectrum acquired on the background was devoid of any characteristic peak at ~ 590 nm (Fig. 6.10).

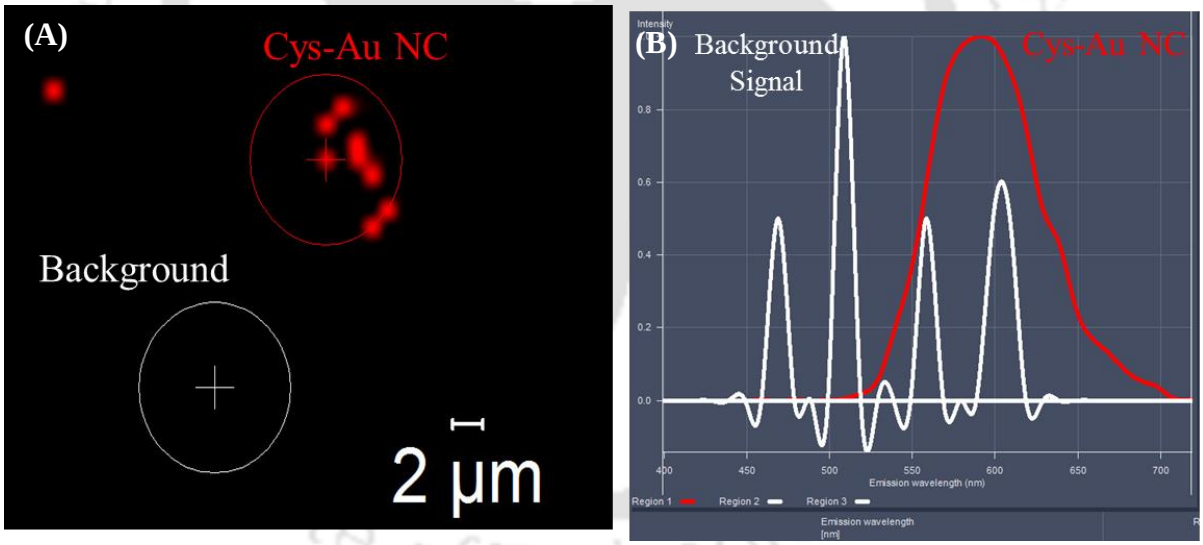

Fig. 6.10 (A) CLSM image of Cys Au NCs **(B)** Corresponding spectra acquired on the regions marked in **(A)**. The instrument displays the emission spectrum in the scale of 1.0 for all measurements.

Thirdly, it was observed that the interference of the detector noise could be tuned by adjusting the value of gain master. Intriguingly, acquiring the blinking of profile of the background (without using any sample) at a gain master of 833, no signal from background could be observed. However, upon increasing the gain master to 1000, background signals could be observed (The results are shown in Fig. 6.13-6.14 in subsequent section).

Nevertheless, the value of the intensity of the background profile was 10^{-3} times of that of the clusters. Thus, in order to avoid even the slightest of interference of background noise, all measurements have been performed at a gain master of 833, as a consequence of which it may be considered that the images and blinking profiles shown in the manuscript are characteristics of luminescent particles and not of background. Please note that the images given as evidence of the integrity of our experimental approach are snapshots taken during the measurement.

In line with point 3 stated above, we have acquired the blinking profiles of Cys Au NCs and the corresponding background in the same frame and shown herein. It may be noted that the maximum intensity of the intermittency profile of the position containing Cys Au NCs was recorded to be ~1 unit. While negligible background noise was recorded for the corresponding background. The snapshots of the results are shown herein (Fig. 6.11).

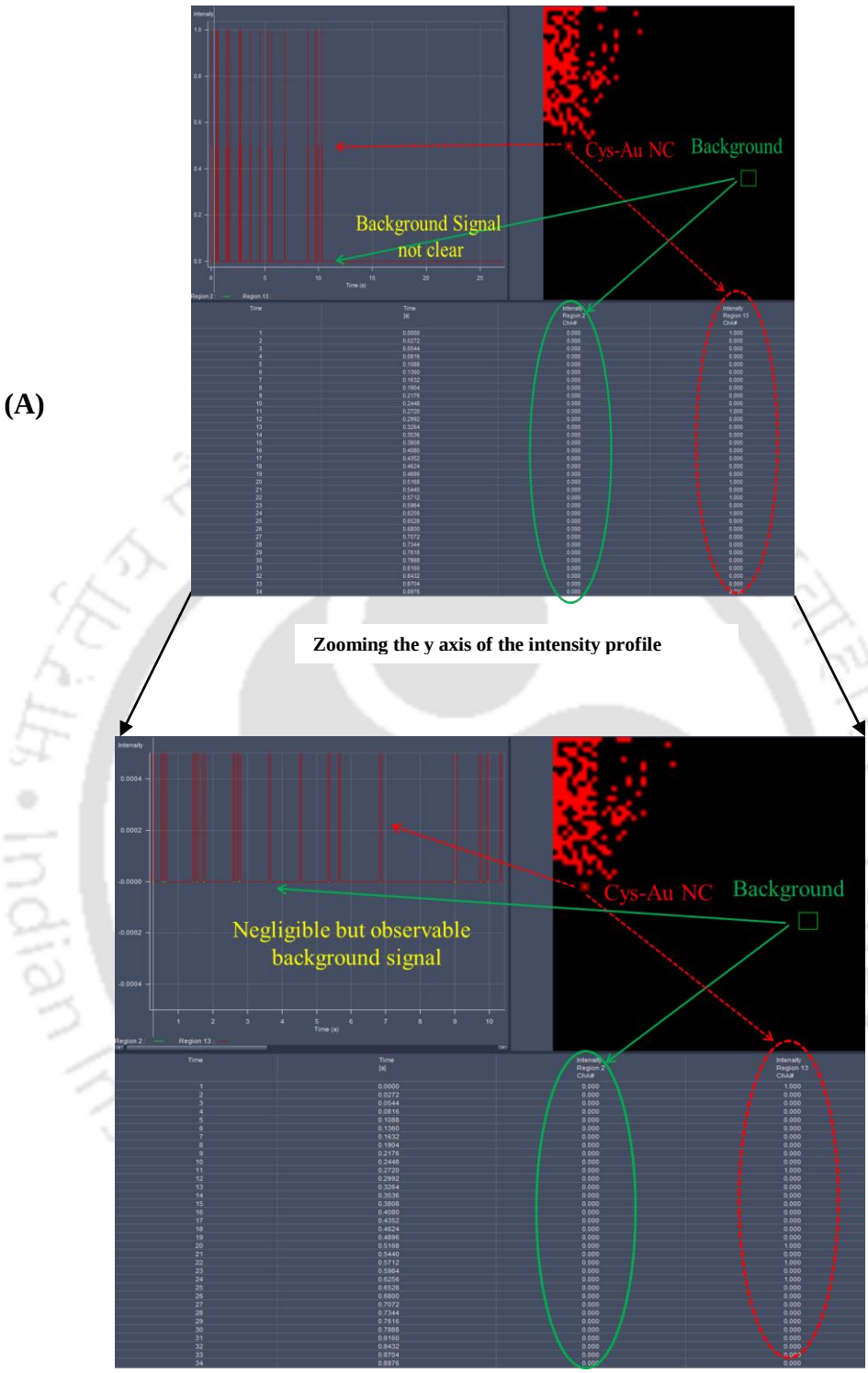

Fig. 6.11 (A) Screenshot of blinking profile of background plus Cys Au NCs and corresponding image of the area at which the blinking profile has been acquired, and corresponding table tabulating the intensity profile of blinking. **(B)** Zoomed version of **(A).** Gain master was set at 833. Frame size was measured to be 64 × 64 μm^2

Thus, based on the above results, it may be considered unequivocally that the results given in the manuscript are due to intermittency characteristics of Cys Au NCs and are not due to detector noise.

Experimental results and explanations to substantiate the possible single particle nature of Cys Au NCs (assembled into a particle)

(1) Calculation of diffraction limited size of the laser focus:

Diffraction limited size of the laser focus = (1.22 x λ) / NA; where NA = numerical aperture = 1.4 for confocal microscope (make: Zeiss LSM 880) and λ = wavelength of the laser =355 nm. Thus, diffraction limited size of the laser focus = 0.309 µm.

(2) Single particle level quantum yield was calculated to corroborate the possible single particle nature of Cys Au NCs and Zn Cys Au NCs (assembled into a particle). The details of the calculation are as follows:

Calculation of quantum yield of Cys Au NCs and Zn Cys Au NCs at a single particle level:

The absorption cross sections of Cys Au NCs, Zn Cys Au NCs and rhodamine 6G (Rh6G) were calculated. In order to do so, the absorption coefficients of Cys Au NCs, Zn Cys Au NCs and Rh6G were calculated from a plot of absorbance versus concentration of the samples. The absorbance of the samples varied linearly with their concentrations (as per Lambert Beer's law). The value of the absorption coefficient was extracted from the slope of the plot, keeping the path length fixed for all the measurements. The absorption coefficients for Cys Au NCs, Zn Cys Au NCs and Rh6G were calculated to be 5.63×10^{-3}, 5.58×10^{-3}, and 5.28×10^{-5} $\mu M^{-1}cm^{-1}$

respectively (Fig.s 6.12 A-C).

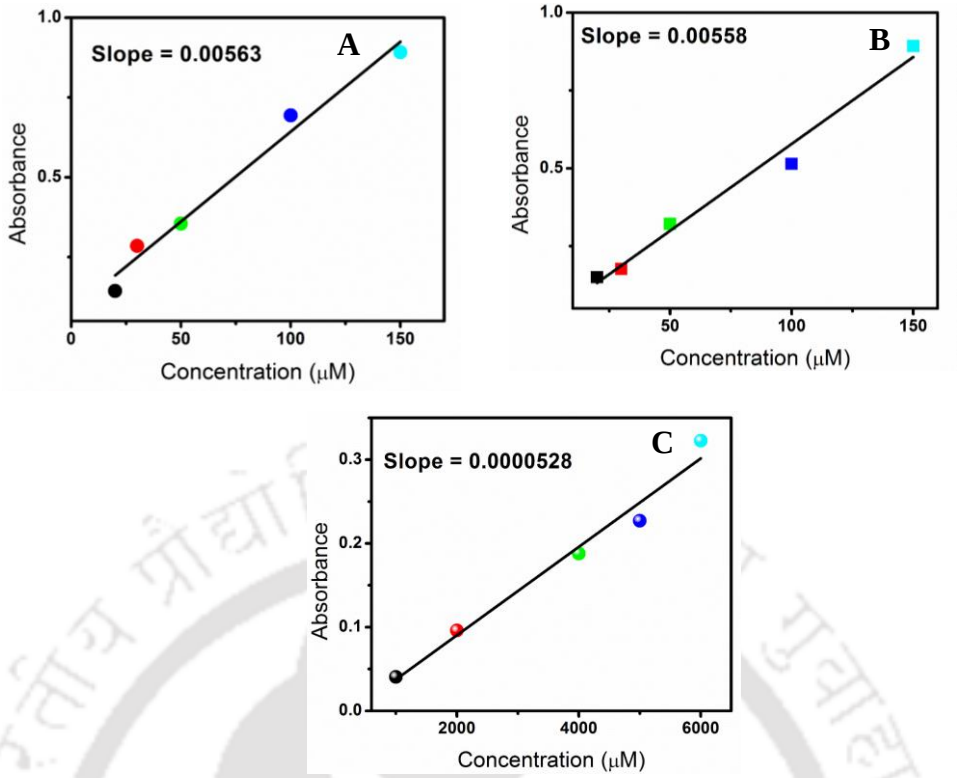

Fig. 6.12 Plot of Absorbance versus Concentration for (A) Cys-Au NCs, (B) Zn-Cys-Au NCs and (C) Rh6G.

Calculation of quantum yield for Cys Au NCs at single particle level:

$\varepsilon_{cys\ Au\ NCs} = 0.00563\ \mu M^{-1}cm^{-1}$

Thus absorption cross section of Cys Au NCs= $(0.00563)/(6.023 \times 10^{23}) = 9.34 \times 10^{-27}\ cm^2$

Similarly, $\varepsilon_{Rh6G} = 0.0000528\ \mu M^{-1}cm^{-1}$

Thus absorption cross section of Rh6G = $(0.0000528)/(6.023\times 10^{23}) = 8.76 \times 10^{-29}\ cm^2$

Mean intensity of 10 particles consisting of Cys Au NCs was calculated (using image J) to be 13.23.

On the other hand, mean intensity of 10 particles consisting of Rh6G was calculated (using image J) to be 13.74. Thus quantum yield of Cys Au NCs is given by:

$QY = QY_{reference} \times (Intensity_{sample}/Intensity_{reference}) \times (Absorption\ cross\ section_{reference}/ Absorption\ cross\ section_{sample}) \times$ (refractive index of sample /refractive index of reference)

Given $QY_{reference} = 0.95$, and refractive indices for reference and sample are same,

QY of Cys Au NCs = 0.008 = **0.8%.**

On the other hand, the quantum yield of Cys Au NCs in solution phase using Rh6G as a standard was calculated to be **0.2 %** by conventional methods. The deviation obtained in quantum yield calculation at a single particle level versus bulk phase could be attributed to the possible aggregation of more than one emitter Cys Au NCs) in one particle observed in CLSM analysis.

Calculation of quantum yield for Zn Cys Au NCs at single particle level:

$\varepsilon_{\text{Zn cys Au NCs}} = 0.00558\ \mu M^{-1}cm^{-1}$

Thus absorption cross section of Zn Cys Au NCs= $(0.00563)/(6.023 \times 10^{23}) = 9.34 \times 10^{-27}\ cm^2$

Similarly, $\varepsilon_{Rh6G} = 0.0000528\ \mu M^{-1}cm^{-1}$

Thus absorption cross section of Rh6G = $(0.0000528)/(6.023\times 10^{23}) = 8.76 \times 10^{-29}\ cm^2$

Mean intensity of 10 particles consisting of Zn Cys Au NCs was calculated (using image J) to be 16.66.

On the other hand, mean intensity of 10 particles consisting of Rh6G was calculated (using image J) to be 13.74. Thus quantum yield of Zn Cys Au NCs is given by:

$QY = QY_{reference} \times (Intensity_{sample}/Intensity_{reference}) \times (Absorption\ cross\ section_{reference}/ Absorption\ cross\ section_{sample}) \times$ (refractive index of sample /refractive index of reference)

Given $QY_{reference} = 0.95$, and refractive indices for reference and sample are same,

QY of Zn Cys Au NCs = 0.007 = **1.2%**

On the other hand, the quantum yield of Zn Cys Au NCs in bulk phase using Rh6G as a standard was calculated to be **0.5 %** by conventional methods. The deviation obtained in quantum yield calculation at a single particle level versus bulk phase could be attributed to the possible aggregation of more than one emitter Zn Cys Au NCs) in one particle observed in CLSM analysis.

Table 6.2 Tabulation of the values of quantum yield at single particle level and bulk phase

Samples	Reference	Quantum Yield (%)	
		Bulk phase	Single particle
Cys-Au NCs	Rhodamine 6 G	0.2	0.8
Zn-Cys-Au NCs		0.5	1.2

(3) The density of the luminescent spots in a particular frame was found to be proportional with concentration of samples used for the measurements.

(4) As it may be noted in Fig. 6.7 (B1), (B2) and (B3), the photo bleaching occurred in a single step rather than via a monotonically decreasing intensity. In order to affirm this, a control experiment was performed where the blinking profile of a portion containing aggregated clusters was acquired. The observed profile demonstrated gradual photo bleaching owing to the presence of multiple particles. Please refer to Fig. 6.8.

Profiles of Detector Noise acquired at various gain masters.

The blinking profiles of only background were also acquired. As already mentioned, the background noise could be adjusted by tuning the value of gain master, the background profiles have been acquired at two different gain master values – i.e., (i) 833, at which no background noise could be detected and hence all measurements in the reported manuscript had been done at that value and at (ii) 1000, the only value at which insignificant but low detector noise could be detected. The results are shown below (Fig. 6.13-6.14):

Gain master set at 833:

A

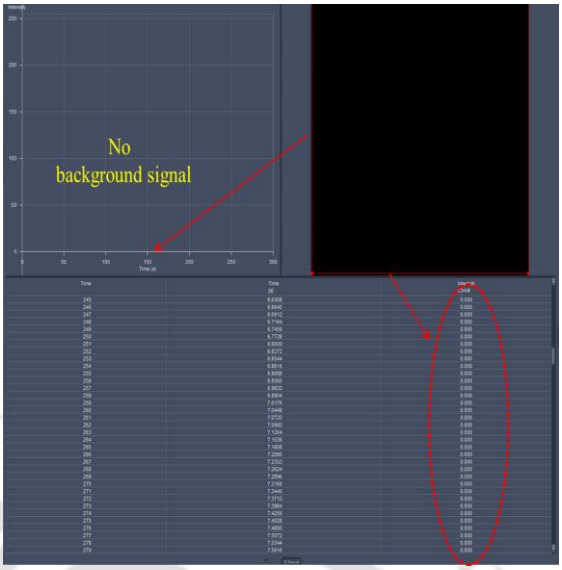

B

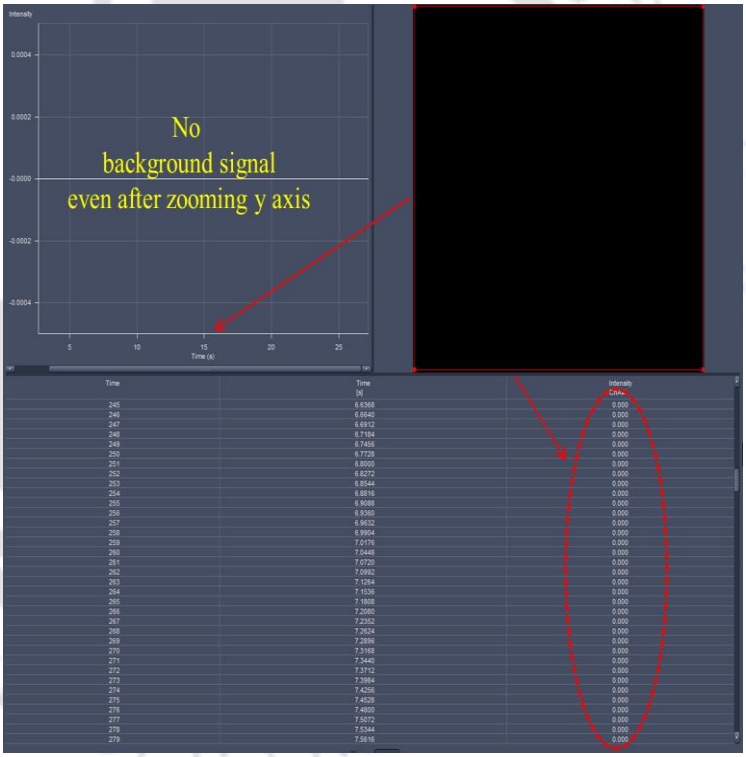

Fig. 6.13 (A) Screenshot of blinking profile of background and the corresponding image of the area at which the blinking profile has been acquired, and the corresponding table tabulating the intensity profile of blinking. **(B)** Zoomed version of **(A).** Gain master was set at 833. Frame size was measured to be 64 × 64 μm^2

Gain master set at 1000:

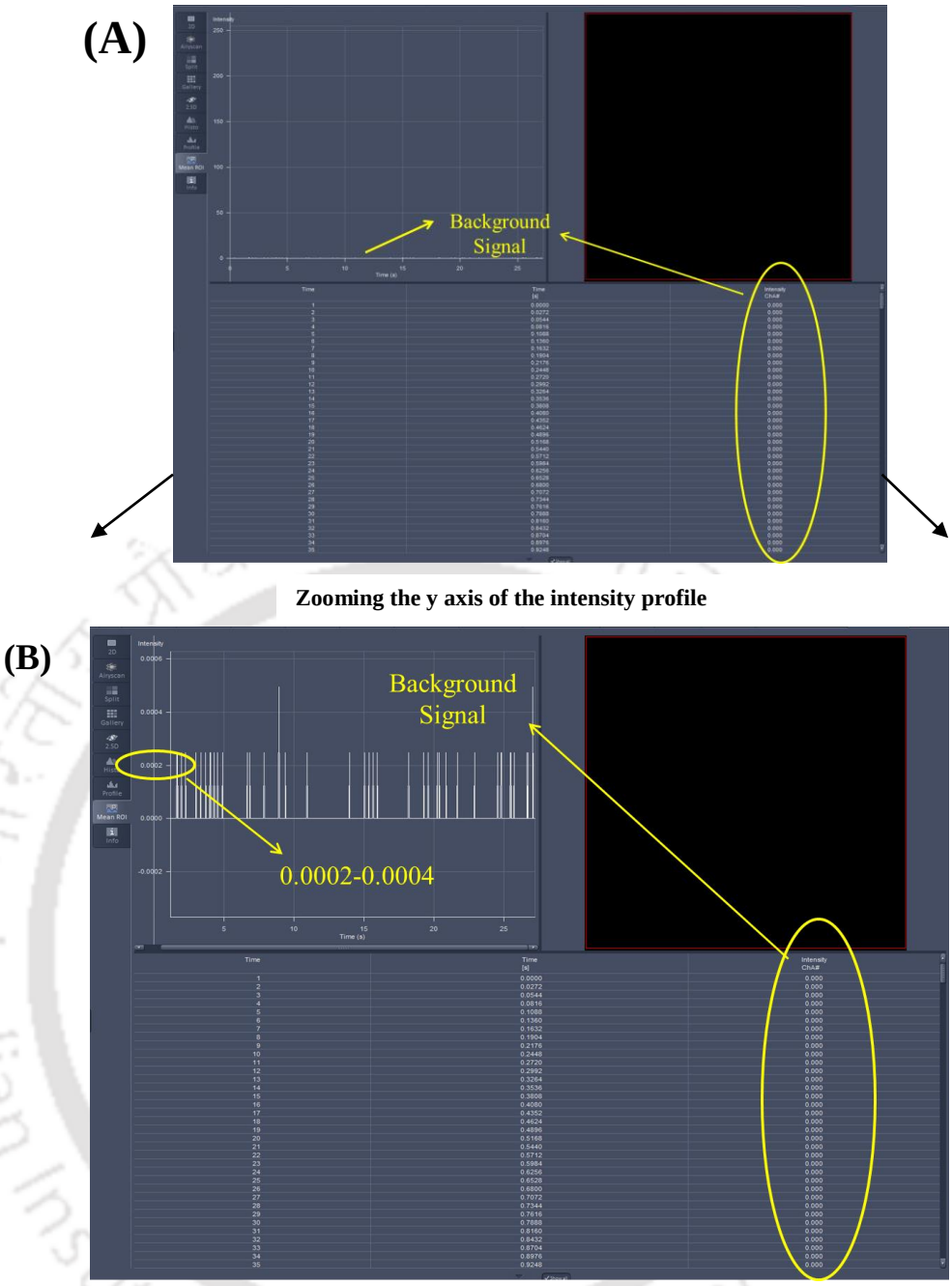

Fig. 6.14 (A) Screenshot of blinking profile of background and the corresponding image of the area at which the blinking profile has been acquired, and the corresponding table tabulating the intensity profile of blinking. **(B)** Zoomed version of **(A).** Gain master was set at 1000. Frame size was measured to be 64 × 64 μm^2.

Intriguingly, the *off* time probability distributions could be fitted with a truncated power law[77-80]through a log-log plot extracted from the obtained data points to particles consisting of Au_{14} NCs (Fig. 6.7). While *on* time values obtained were devoid of any distribution and a single specific value of 27 ms was obtained for all the mentioned NCs. 50 particles were analyzed in case of Cys-Au_{14} NCs and 30 particles in case of Trp-Au_{14} NCs and His-Au_{14} NCs. Importantly, the value of the exponent (α_{off}) of the *off* time probability

distribution of a particles consisting of Cys-Au_{14} NCs (0.32) was found to be lesser compared to Trp-Au_{14} NC (0.50) and higher compared to His-Au_{14} NC (0.17) (Fig. 6.7 and Table 6.3). The difference in the exponents of the off time probability distribution of all three Au_{14} NCs may be due to the presence of different ligands attached to the clusters. Additionally, in order to confirm the photobleaching of Cys-Au NCs, the blinking profile was recorded for longer time (189 s, Fig. 6.15).

Table 6.3 Fitting parameters (as per the data obtained from Fig. 1) for probability density of *off*-states (α_{off} (t) for (A) Cys-Au_{14} (B), Trp-Au_{14} and (C) His-Au_{14} NCs.

Equation: $\rho_i(\tau) = A_i \tau^{-\alpha_i} \exp(-\mu_i \tau)$

Sample	α_{off}	μ_{off}	A_{off}	χ^2
(A) Cys – Au_{14} NCs	0.32 ± 0.06	6.9 ± 0.86	124.7 ± 32.2	0.99
(B) His - Au_{14} NCs	0.17 ± 0.06	7.2 ± 0.8	67.9 ± 17.06	0.99
(C) Trp - Au_{14} NCs	0.49 ± 0.03	5.8 ± 0.47	88.4 ± 12.58	0.99

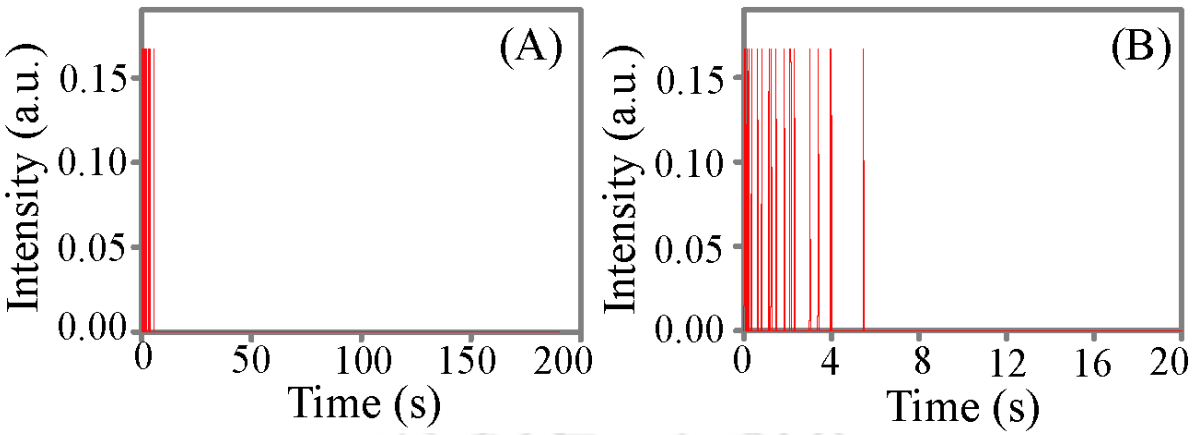

Fig. 6.15 (A) Blinking profile of Cys Au NCs acquired for 189 seconds. **(B)** The same profile as shown in (**A**) plotted at a time scale of 20 seconds.

Interestingly, upon formation of crystalline assembly of Cys-Au_{14} NCs following complexation with Zn^{2+} ions, hereafter referred to as Zn-Cys-Au_{14}-NCs, enhancement in emission intensity (at 590 nm with λ_{ex}-355 nm) and life time was noticed (Fig. 6.16-6.17 and Table 6.4). Similar observations in terms of emission intensity (at 590 nm) were made in the case of crystalline assemblies of Trp-Au_{14} and His-Au_{14} NCs (6.16).

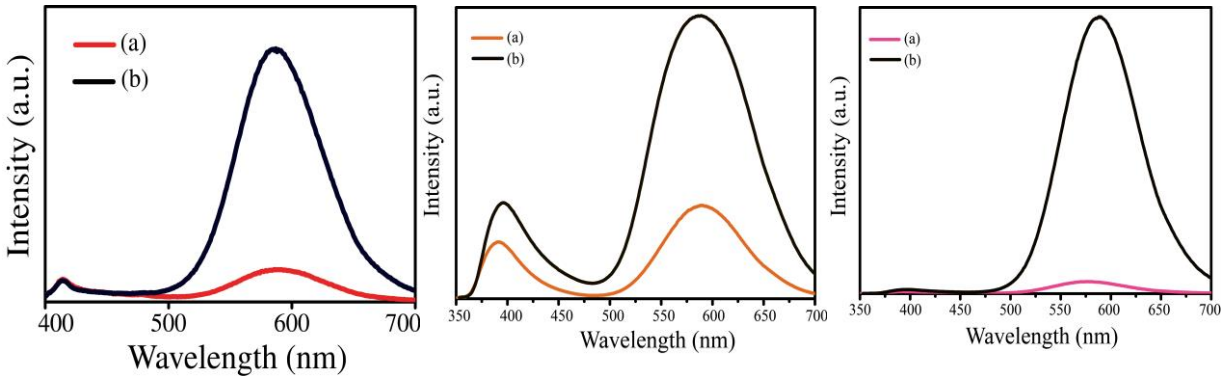

Fig. 6.16 Emission spectra (λ_{ex} - 355 nm) of as-synthesized (A) Cys-Au_{14} NCs, (B) Trp-Au_{14} NCs and (C) His-Au_{14} NCs (a) before and (b) after complexation with Zn^{2+} ions.

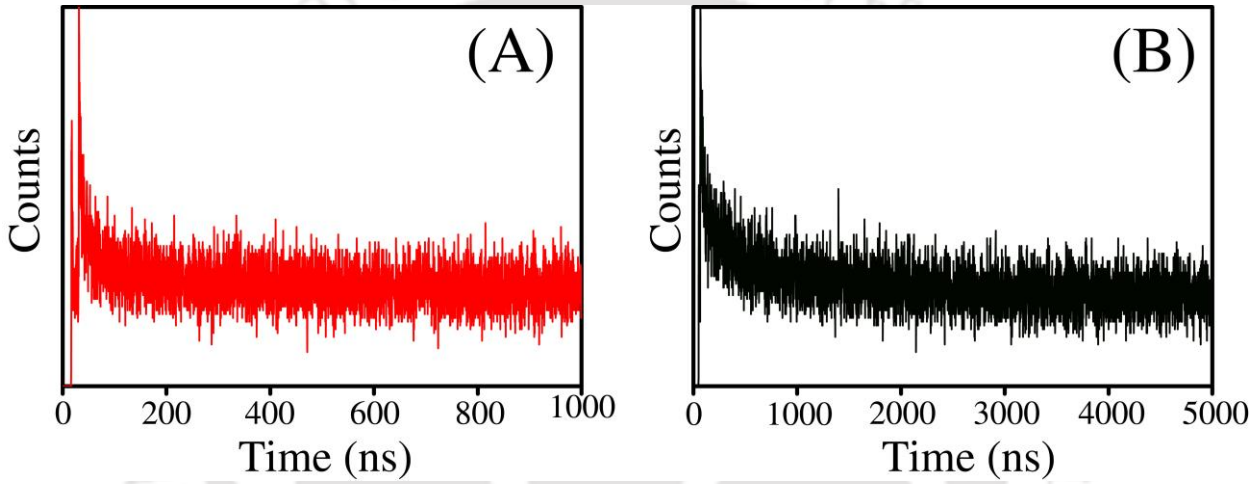

Fig. 6.17 Time-resolved photoluminescence spectra (recorded using 375 nm excitation laser) of as-synthesized (A) Cys-Au_{14} NCs and (B) Cys-Au_{14} NCs following complexation with Zn^{2+} ions.

Table 6.4 Average emission life times calculated from the time resolved photoluminescence spectra (recorded using 375 nm excitation laser) of as-synthesized (A) Cys-Au_{14} NCs and (B) Cys-Au_{14} NCs following complexation with Zn^{2+} ions.

Sample	A_1 (%)	τ_1 (ns)	A_2 (%)	τ_2 (ns)	χ^2
(A) Cys-Au_{14} NCs	41.1	7.01	58.9	142.5	1.03
(B) Zn-Cys-Au_{14} NCs	22.2	44.1	77.8	846.1	1.07

Selected area electron diffraction (SAED) analysis performed on the particle shown in Fig. 6.18 confirmed the crystalline nature of the product formed due to reaction between Cys-Au_{14} NCs and Zn^{2+} ions (6.18)**.** SAED analysis of Zn-Cys-Au_{14}-NCs revealed hexagonal arrangement of the constituents with corresponding edge length of 4.7 ± 0.2 Å. The lattice spacing obtained from high resolution transmission electron microscopic (HRTEM) analysis performed on the particle shown in Fig. 6.18 C-D was measured to be 22 Å and 8.4 Å. The details of possible coordination between zinc ions and Au clusters via the ligands are discussed below. A possible structure of the crystalline complex (Cys-Zn-Au_{14}-NCs) has been proposed based on these experimental observations and computational optimization using Avogadro software (Fig. 6.19). On the other hand, no hexagonal diffraction pattern in the SAED was observed when a mixture of Cys, MPA and Zn^{2+} ions was subjected to SAED analysis (Fig. 6.20). A schematic diagram depicting the spatial organization of Au_{14} NCs and Zn^{2+} ions coordinated by the ligands stabilizing the NCs the structure based on aforementioned observations has been represented herein (Fig. 6.18 E). Additionally, FTIR spectroscopic analysis clearly indicated the formation of the complex between Zn^{2+} ions and Au_{14}-NCs, which might have occurred by coordination through the carboxylate groups of Cys (Fig. 6.21).

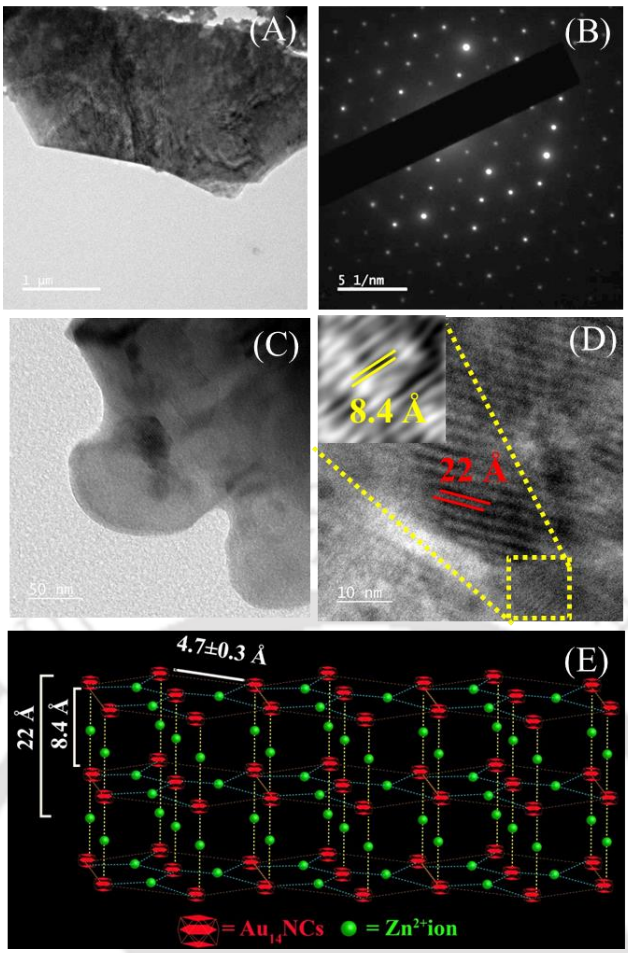

Fig. 6.18 (A) Transmission electron microscopy (TEM) image and **(B)** corresponding selected area electron diffraction (SAED) pattern of Zn-Cys-Au_{14}-NC. **(C)** TEM image and **(D)** corresponding high resolution TEM image and inverse fast Fourier transformed (IFFT) image (inset) of Zn-Cys-Au_{14}-NC. **(E)** Representative schematic depiction of the structure of Zn-Cys-Au_{14}-NCs

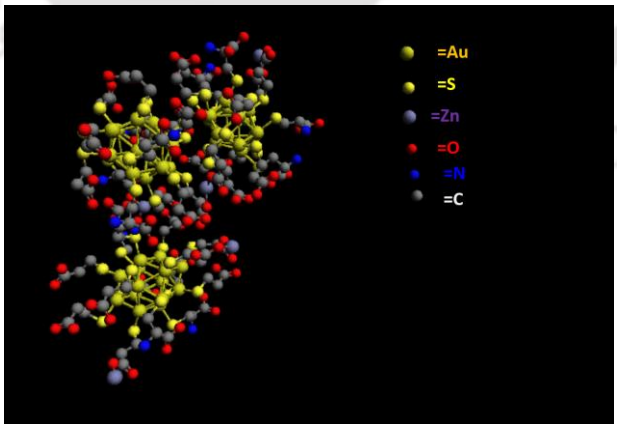

Fig. 6.19 Computationally optimized structure of Zn-Cys-Au_{14}-NC complex obtained using Avogadro software. Hydrogen atoms have not been included for simplicity.

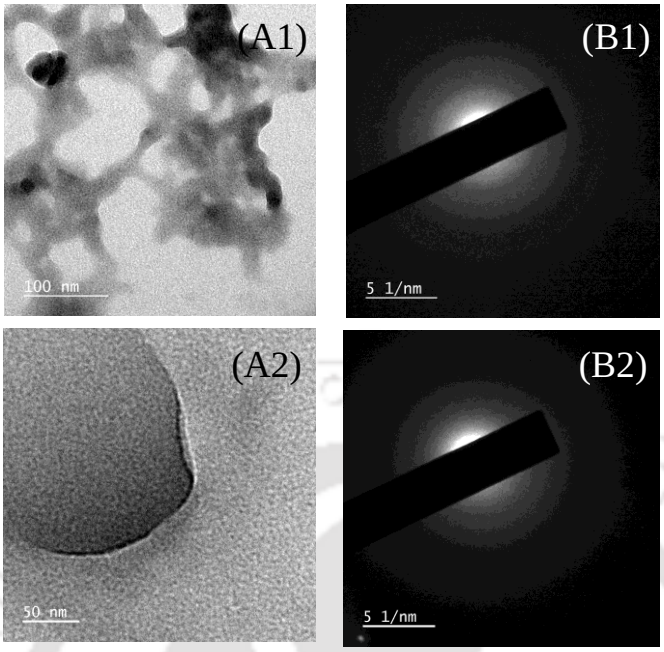

Fig. 6.20 (A) Transmission electron microscopy (TEM) images and **(B)** selected area electron diffraction (SAED) patterns of the evaporated dispersion containing Cys, MPA and Zn^{2+} ions and acquired at two different positions (1 and 2) of the sample.

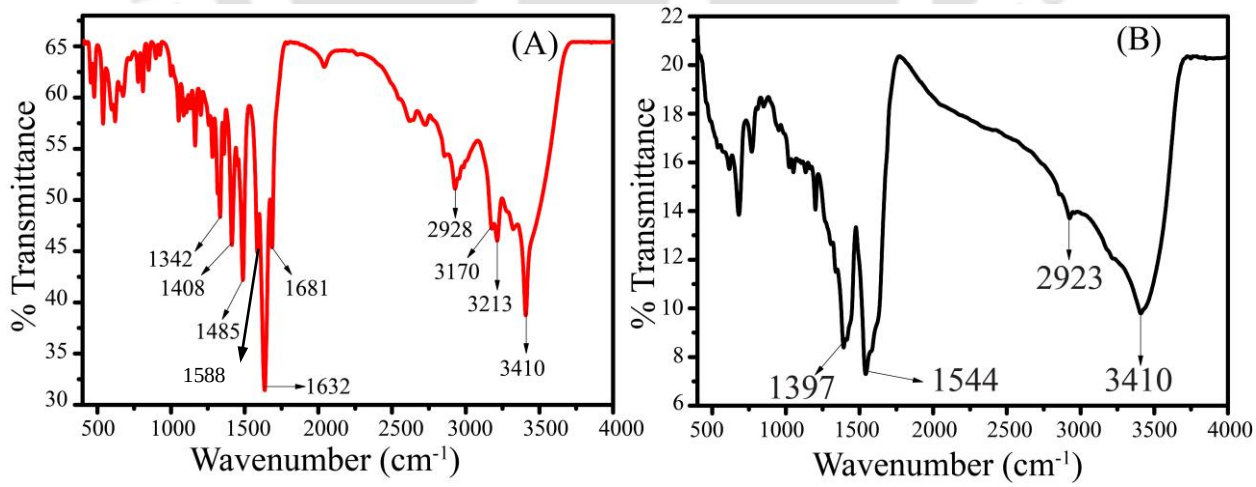

Fig. 6.21 FTIR spectra of (A) Cys-Au_{14} NCs and (B) Zn-Cys-Au_{14} NCs.

Structural details of Zn-Cys-Au_{14}-NCs - Concisely, a regular hexagon is formed comprising of six flat 3D Au_{14} NCs (with D_{2h} symmetry)[63] at the apexes and one Au_{14} NC at the center. The two NCs at the apexes and the one at the center are connected via Zn^{2+} ion coordinated to MPA ligated to the Au atoms constituting the NCs. Hence, a two dimensional hexagonal layer is formed where each hexagon comprises of seven Au_{14} NCs and three Zn^{2+} ions. The distance between each Au_{14} NCs forming the hexagon (i.e., the edge length of the hexagon) has been computed to be 4.4 Å, which is close to the observed value of 4.7 ± 0.2 Å. On the other hand, vertically, the NCs are linked through Cys molecules attached to the Au_{14} NCs via coordination through Zn^{2+} ions. The cluster to cluster distance in the vertical dimension has been calculated to be 8.7 Å, which is in close concordance with the observed value of 8.4 Å. Moreover, in the vertical direction, the distance between Au_{14}–Cys–Zn-Cys–Au_{14} –Cys–Zn has been calculated to be 17.2 Å. Further, Zn-Cys distance has been observed to be 6.3 Å which when added to 17.2 Å is close to the observed value of 22 Å and hence defines the repeat unit in the crystal.

FTIR analysis: It is interesting to note that the peak due to asymmetric stretch of carboxylate group of MPA attached to Cys-Au_{14} NCs at 1681 cm^{-1} was absent in the FTIR spectrum of Zn-Cys-Au_{14}-NCs. This indicates possible binding of MPA with zinc ions through the carboxylate group of the former. Additionally, the peak due to asymmetric stretch of cysteine at 1588 cm^{-1} was shifted to 1544 cm^{-1} upon complexation with zinc ions thereby indicating possible binding of cysteine attached to Cys-Au_{14} NCs with zinc ions via the carboxylate group of the former. Also, the peaks due to symmetric stretches of carboxylate group of MPA and cysteine attached to Cys-Au_{14} NCs were observed to have been dampened upon complexation with zinc ions. The non-involvement of the amine group of cysteine in complexation with zinc ions was confirmed from the observation that the peak position due NH_3^+ at 3410 cm^{-1} practically remained unaltered upon complexation with zinc ions.

Importantly, the suppression of the blinking of all three Au_{14} NCs was noticed upon formation of their Zn^{2+} mediated crystalline assembly (Zn-Au_{14}-NCs) (Fig. 6.22). The evidences of the (i) single particle nature (ii) quantum yield at single particle level and (iii) ruling out the interference of the detector noise with blinking of Zn-Cys-Au NCs are given (Fig. 6.23-6.25). Further, the blinking profile (using CLSM) of Zn-Au_{14}-NCs was recorded against particles shown in 6.22. As opposed to all three individual clusters, their corresponding crystalline assemblies were found to be devoid of *off* states. Additionally, it

was found that the on time of all three crystalline Zn-Au_{14}-NCs was much sustained and prolonged compared to non-assembled Au_{14} NCs. This clearly indicated the non-blinking behavior of all three mentioned Zn-Au_{14}-NCs and subsequently demonstrated the generality of the approach of forming crystalline assembly to arrest blinking in particles consisting of gold clusters. This is consistent with the observation of higher emission intensity (at 590 nm) of Zn-Au_{14}-NCs compared to individual Au_{14} NCs for all three cases (Fig. 6.16). Additionally, the higher luminescence lifetime of Zn-Au_{14}-NCs, compared to the ligand stabilized Cys-Au_{14} NCs supported the non-blinking behavior of Zn-Cys-Au_{14}-NCs (Fig. 6.17). Thus the approach of formation of programed assembly of atomic NCs may be claimed to be an effective and general strategy to eliminate the blinking observed in non-assembled clusters.

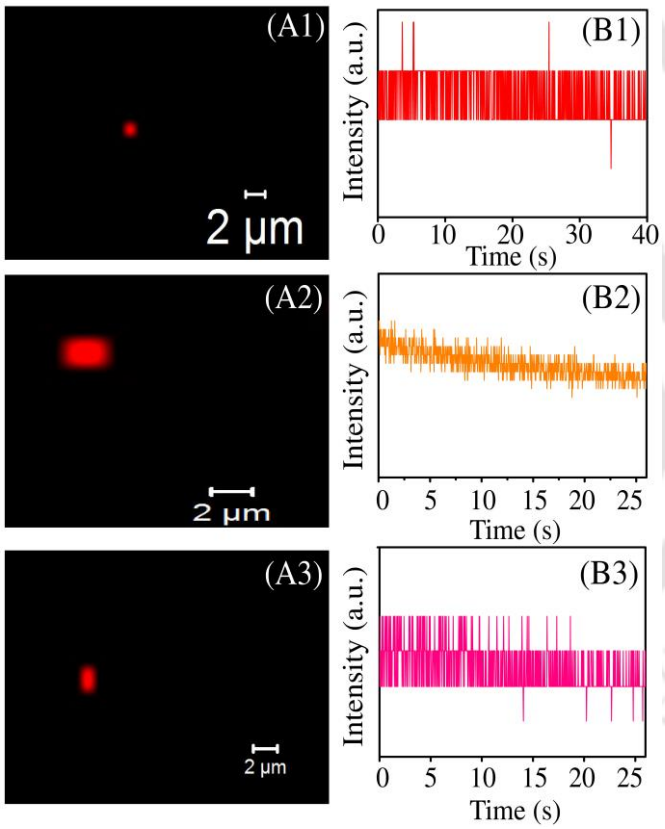

Fig. 6.22 (A) Confocal laser scanning microscopic images and **(B)** time dependent photoluminescence intermittency profile (which was recorded against a particle each as marked in Fig. 1A) of crystalline assembly of (1) Cys-Au_{14}, (2) Trp-Au_{14} and (3) His-Au_{14} NCs, respectively, following reaction with Zn^{2+} ions.

Control experiments and explanations to eliminate the interference of detector noise in the intermittency signals of Zn Cys Au NCs

In the CLSM model used for pursuing the current study (Zeiss LSM 880), range indicator is used to specify the area of luminescence and that of background in a particular frame of measurement. By default, red portions indicate non-zero or high pixel values and blue portions are indicative of zero pixel values.

Also, in the confocal setup (LSM 880), gain master is adjusted to maximize the signal to noise ratio in a particular measurement. Herein, an optimised gain master of value 833 has been used to eliminate the background noise and acquire noise free images.

Thus we have recorded the CLSM image of Zn Cys Au NCs along with background with the range indicator being enabled. Interestingly, the area comprising of the clusters appeared red and the background (where absence of crystalline assembly of clusters was anticipated visually) appeared blue (Fig. 6.23 A-B). It is to be noted here that the red portion is indicative of a luminescent signal and is not a characteristic emission colour of the clusters.

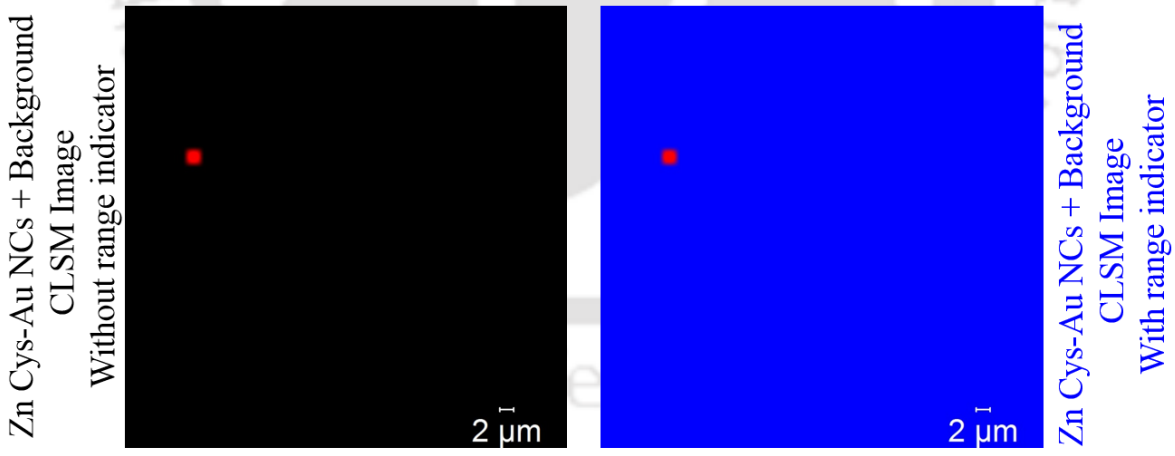

Fig. 6.23 (A) Confocal laser scanning microscopic image of Zn Cys Au NCs in presence of background **(B)** Corresponding image Zn Cys Au NCs in presence of background with range indicator being enabled.

Secondly, in order to establish that the reported images and the blinking profiles are typical signatures of the luminescent crystalline assemblies of clusters, we have acquired the

luminescent spectrum on a typical particle of Zn Cys Au NCs. Similarly, we have acquired the spectrum of the background in the same frame as that of the clusters. It is worthy to be mentioned here that the acquisitions have been done at a gain master value of 833. This value was optimized to completely eliminate the interference of background. Details of the optimization process has been discussed in the earlier section. Interestingly, in case of Zn Au NCs, the spectrum matched exactly with that of the solution phase, exhibiting an emission maximum at 590 nm. On the other hand, the spectrum acquired on the background was devoid of any characteristic peak at ~ 590 nm (Fig. 6.24).

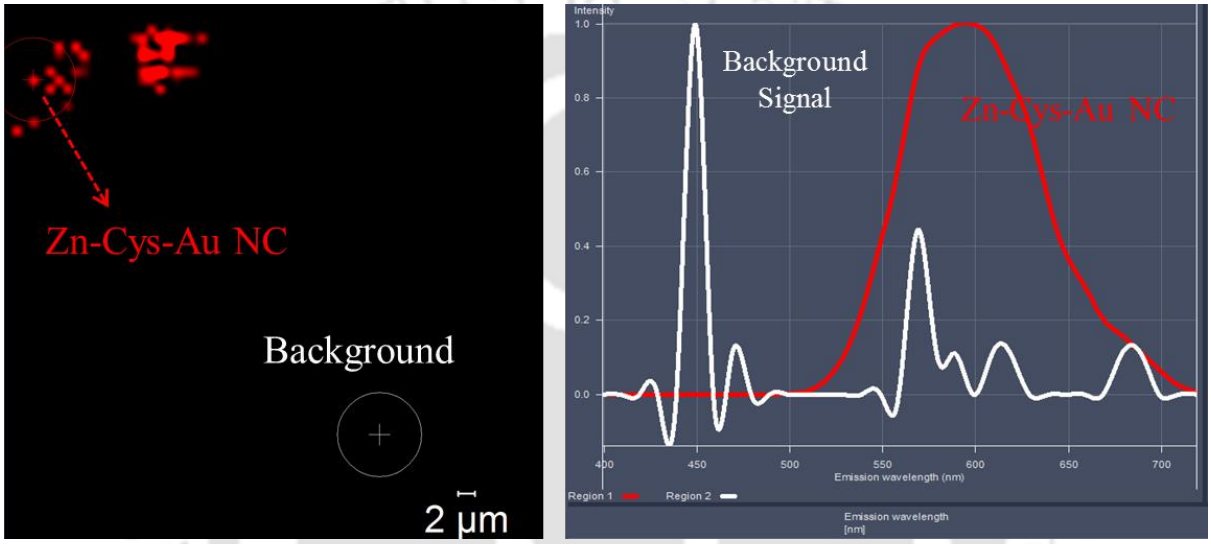

Fig. 6.24 (A) CLSM image of Zn Cys Au NCs **(B)** Corresponding spectra acquired on the regions marked in **(A)**. The instrument displays the emission spectrum in the scale of 1.0 for all measurements.

We have acquired the blinking profiles of Zn Cys Au NCs and the corresponding background in the same frame and have shown herein. It may be noted that the intermittency profile of the position containing Zn Cys Au NCs could be identified unambiguously in presence of the negligible background noise recorded for the corresponding background. The snapshots of the results are shown herein (Fig. 6.25).

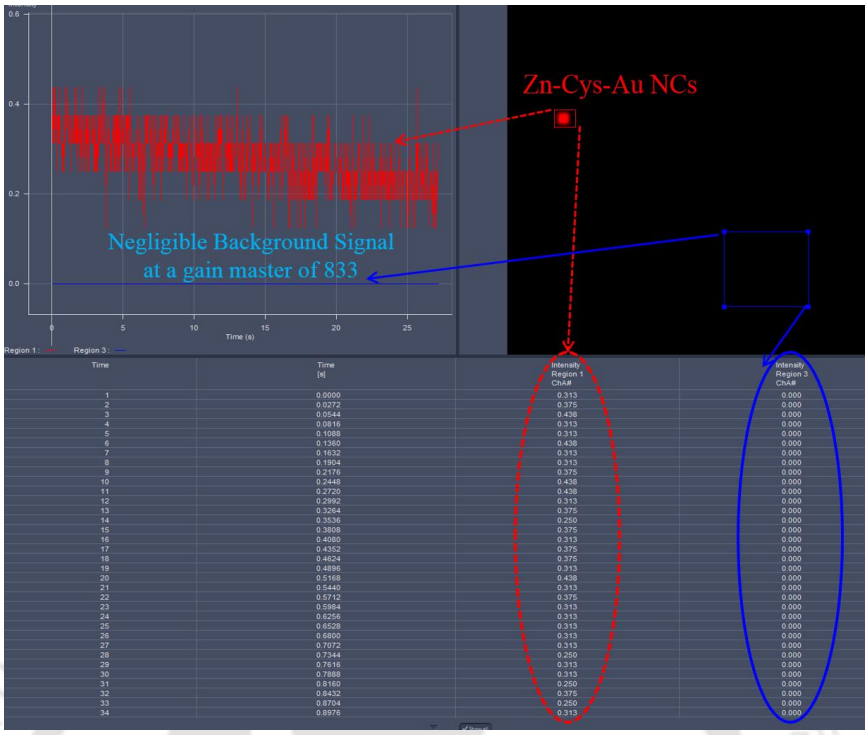

Fig. 6.25 (A) Screenshot of blinking profile of background plus Zn Cys Au NCs and the corresponding image of the area at which the blinking profile has been acquired, and the corresponding table tabulating the intensity profile of blinking. **(B)** Zoomed version of **(A).** Gain master was set at 833. Frame size was measured to be 64 × 64 μm^2

A schematic representation of the formation of a three dimensional crystalline assembly of MPA and Cys stabilized Au_{14}-NCs – followed by complexation with Zn^{2+} ions is shown in Scheme 6.1 A. Scheme 6.1 B represents the energy level diagram of a particles consisting of Au_{14}-NCs before and after complexation with Zn^{2+} ions. As is clear from Scheme 1B, two electronic transitions; (i) radiative (S_1-S_0) and (ii) nonradiative dark and/or surface state transitions (S_1- dark and/or surface states) are possible when relaxation of a photo excited electron of a particle consisting of Au_{14}-NCs occurred and consequently *on* and *off* states for Au_{14}-NC could be observed. Now, given the ease of vibrational and rotational (conformational) relaxation of the ligands attached to the NCs, transition to a non-radiative dark and/or surface state is deemed feasible. Thus, depending upon the extent of intersystem crossing, the occurrence of *off* and *on* times is likely to be observed.[81] However, the *on* time of intermittency was primarily single valued and was devoid of any distribution. This clearly indicated that emissive transition occurred in a fixed pathway unlike the different non-radiative transition pathways. Importantly, upon complexation with Zn^{2+} ions, nonradiative dark and/or surface state transitions of Au_{14}-NC might have been restricted and in turn more number of radiative transitions (S_1-S_0) was feasible. This might have helped to eliminate the

occurrence of *off* state of particles consisting of Au_{14}-NCs following complexation with Zn^{2+} ions. Thus the conformational locking of the ligands and subsequent structural rigidity attained in the crystalline assembly of Au_{14}-NCs may be the reason for their observed non-blinking nature.

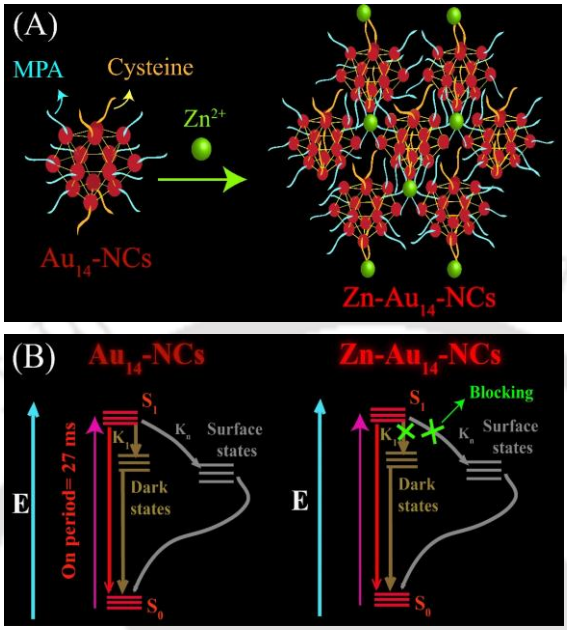

Scheme 6.1 (A) Schematic representation of the formation of three-dimensional crystalline assembly of Cys and MPA stabilized Au_{14} NCs following complexation with Zn^{2+} ions. **(B)** Schematic energy level diagrams representing Au_{14} NCs and Zn-Au_{14}-NCs.

Notably, the reversible adsorption and desorption of CO_2 by the crystalline assembly of Cys-Au_{14}-NCs was tested via monitoring the changes in the blinking profiles of individual crystalline particles using CLSM. Initially crystals of Zn-Cys-Au_{14}-NCs were found to be non-blinking (Fig. 6.26 A). However, when a partial pressure of 2.5% of CO_2 was maintained in the confocal chamber, the same non-blinking particles consisting of Zn-Cys-Au_{14}-NCs became non-luminescent (Fig. 6.26 B). However, following lowering of CO_2 pressure to 1.5 %, the same crystal started to blink again (Fig. 6.26 C). On further lowering the CO_2 pressure to 0.6 % the original non-blinking nature of Zn- Cys-Au_{14}-NC was restored (Fig. 6.26 D). These results clearly indicated the possibility of storage of CO_2 at the level of nanoscale particles supplemented with luminescence change for observation of the phenomenon. On the other hand, investigations also revealed that as-synthesized clusters did not exhibit any of the abovementioned properties (Fig. 6.27). It may be mentioned here that similar observations were made in terms of quenching and restoring of luminescence of Zn-Cys-Au_{14}-NCs in the dispersion phase following adsorption and desorption of CO_2 (Fig. 6.28). Further, the

adsorption and desorption of CO_2 in the Zn-Cys-Au_{14}-NCs was confirmed from the gas adsorption analysis. The CO_2 adsorption capacity of the Zn-Cys-Au_{14}-NCs was determined to be 1.79 mM per gram at 20 bar pressure and 20 ^oC (Fig. 6.26 E). Overall, the results clearly demonstrated the superiority of Zn-Cys-Au_{14}-NCs, compared to only Cys-Au_{14}-NCs, in the storage and detection of CO_2. It is plausible that the interaction of CO_2 might have occurred through the Zn ions present in the crystalline assembly of Cys-Au_{14}-NCs Fig. 6.29). However, the details of the mechanism are yet to be established.

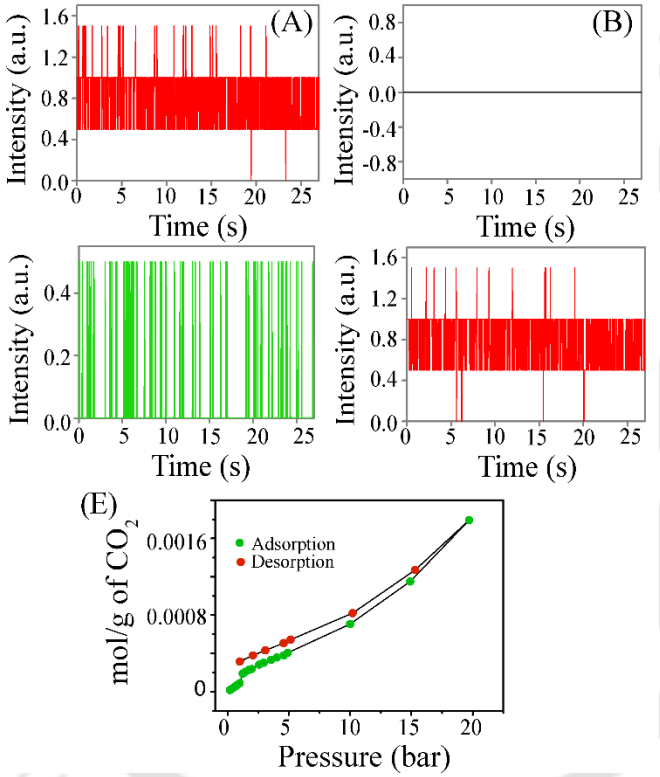

Fig. 6.26 Time-dependent photoluminescence intermittency profile of crystalline assembly of Zn-Cys-Au_{14}-NCs following adsorption of **(A)** 0.0, **(B)** 2.5, **(C)** 1.5, and **(D)** 0.6% of CO_2. **(E)** Adsorption and desorption isotherms of CO_2 on Zn-Cys-Au_{14}-NCs at 20 ^oC.

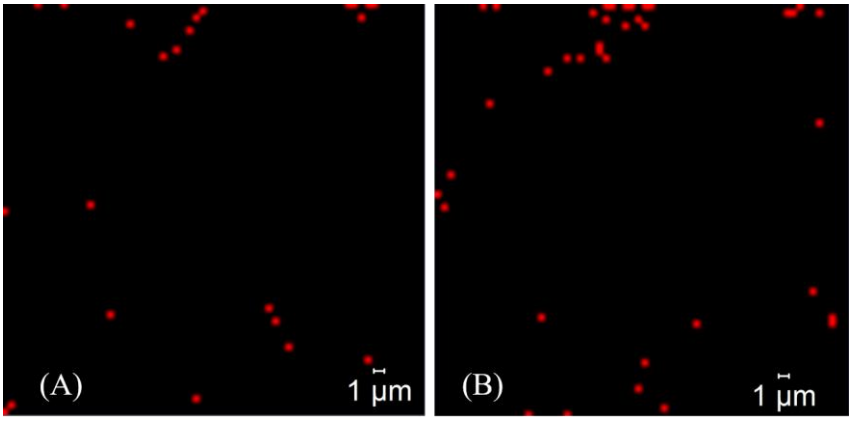

Fig. 6.27 Confocal laser scanning microscopic image of (A) Cys-Au_{14} NCs and the same sample following (B) purging by 2.5% CO_2.

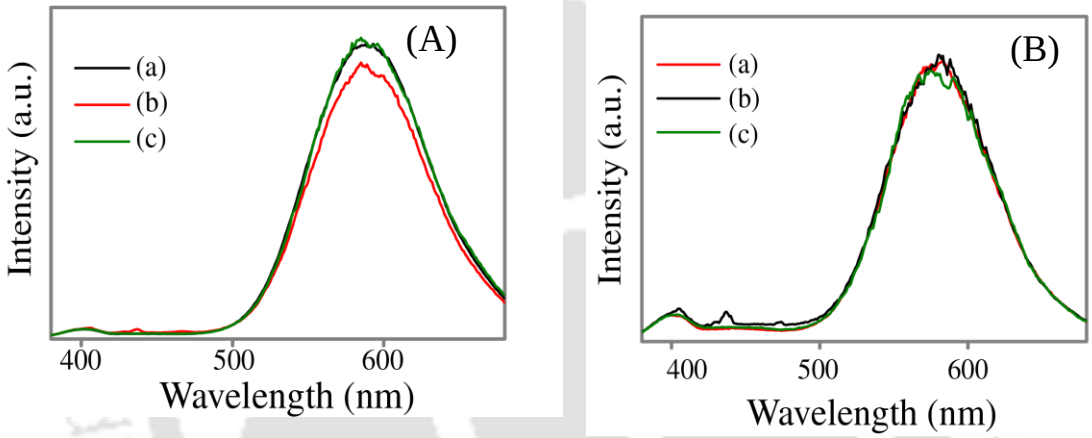

Fig. 6.28 (A) Photoluminescence spectrum of (a) aqueous dispersion of Zn-Cys-Au_{14} NCs and that same sample following (b) purging by CO_2 and then (c) release of CO_2. **(B)** Photoluminescence spectrum of (a) Cys-Au_{14} NCs, and the same sample following (b) purging by CO_2 and then (c) release of CO_2. The excitation wavelength was fixed at 355 nm.

Explanation for proposing zinc as the plausible site Storage of CO_2 in Zn Cys Au NCs

It has been proposed in the manuscript that zinc ions are the potential sites for storage of CO_2. In order to substantiate this, we had provided the results of control experiments - the effect of CO_2 on ligand stabilized Cys-Au NCs (without zinc ions). Interestingly, no significant effect of CO_2 was observed on the luminescence of Cys-Au NCs (Fig. 6.27-6.28). This indicated the critical role of zinc ions in storage of CO_2. But it may be argued here that the properties of non-assembled clusters may be different from that of assembled ones and hence non assembled clusters, in absence of an assembling agent, could not store CO_2. However, to address this issue and to further highlight the crucial role of zinc

ions in storage and sensing of CO_2, we had synthesised ionic assembly of gold clusters mediated by sodium ions. Intriguingly, a typical particle of consisting sodium assisted assembly of Cys Au NCs (Na-Cys Au NCs), analogous to Zn Cys Au NCs, exhibited non blinking behaviour, which affirmed the formation of assembly of the clusters (Fig. 6.29 A). However, upon purging with CO_2, no change in blinking behavior of Na-Cys Au NCs was observed (Fig. 6.29 B). This confirmed that zinc ions played an important role in storage and sensing of CO_2.

It is evident from Fig. 6.18 E, that the ratio of Au:Zn is 1:2. Thus the chemical formula of the assembly could be written as $Au_{14}MPA_{10}Cys_4Zn_2$.

As per the proposed structure, the molecular weight of the crystalline assembly is:

$14\times Au + 10 \times MPA + 4 \times Cys + 2 \times Zn = 4408$

As zinc is proposed to be the active centre for storage of CO_2, $(2 \times Zn) = 130$ g in 4408 gram is effective for storage of CO_2.

Therefore, in 1 g, 0.029 g is effective for storage of CO_2.

0.029 g of zinc corresponds to 0.00045 M = 0.45 mM.

Now, since in per unit cell (containing 2 zinc ions) (Fig. 2 E), one zinc ion is tri coordinated (with MPA), thus can further coordinate to three CO_2, and the other being bi coordinated (with Cys) can further coordinate to 4 CO_2 (in order to achieve maximum coordination of 6), total 7 CO_2 can be incorporated in a unit lattice of Zn Cys Au NCs.

Thus unit equivalence of zinc to CO_2 is 2:7

Therefore, for 0.4 mM of zinc ions present in the lattice, $(0.45 \times 7)/2 = 1.575$ mM of CO_2 can be stored per gram of Zn Cys Au NCs. This closely matches with our observed value of 1.79 mM of CO_2 stored per gram of Zn Cys Au NCs.

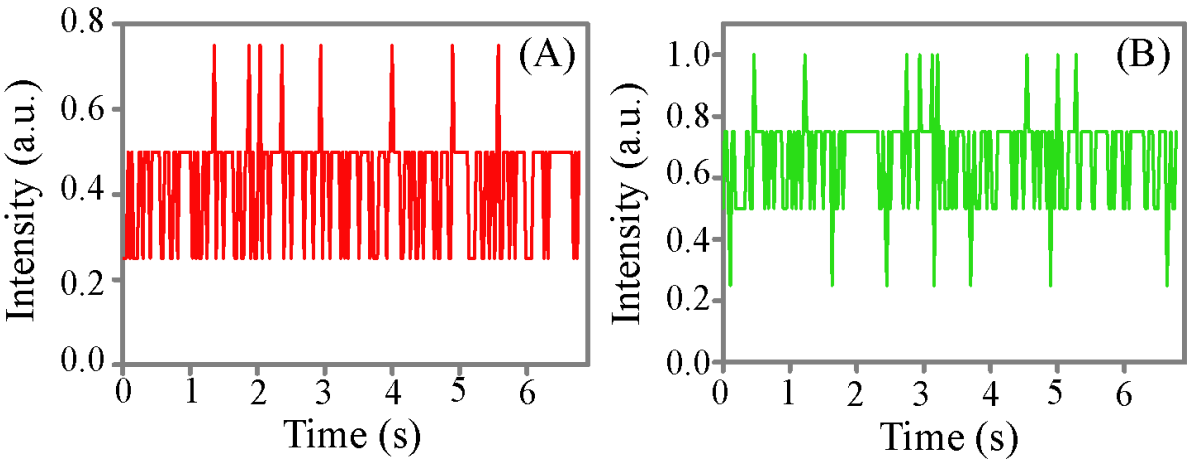

Fig. 6.29 (A) Blinking profile of Na-Cys Au NCs at 0% CO_2. **(B)** Blinking profile of Na-Cys Au NCs at 4.7% CO_2.

6.3 Conclusions

In a nutshell, blinking behavior of three different ligand stabilized Au_{14} NCs was studied, which were observed to have high number of *off* states and a single valued *on* state in their blinking profiles. In addition, the tunability of the exponents of their *off* state probability distributions (fitted with truncated power law) could be achieved depending upon the ligand used during their syntheses. On the other hand, Zn^{2+} mediated three dimensional crystalline assemblies of Au_{14} NCs (Zn-Au_{14}-NCs) exhibited nonblinking characteristics. The analytical studies, supported by computational modelling, was used to establish the rigid three dimensional structure of the crystalline assembly and thus accounted for the observed difference in the blinking profile and emission characteristics in comparison to as such Au_{14} NCs. Intriguingly, based on the changes in the blinking profile of crystalline assembly of Au_{14} NCs, the room temperature storage and recovery of CO_2 were possible. Also, the ability for sensing of CO_2 by nanoscale particles (consisting of Au_{14} NCs) through the measurement of luminescence intermittency provided a new approach in CO_2 storage through simultaneous sensing. Thus, in this report, we present a versatile and general strategy to suppress the intermittency in NCs, which is deemed a significant barrier to their practical utilization.

Chapter 7

Summary and Future Prospects

7.1 Summary

The present thesis work covers several aspects of atomic nanoclusters, ranging from synthesis to applications of nanoclusters followed by complexation reaction assisted formation of crystalline assemblies of nanoclusters and their application potential. In the current thesis, thumb imprint based detection of hyperbilirubinemia has been achieved using luminescent Au NCs. Further, zinc coordinated crystalline assemblies of ligand stabilized Au NCs has been formed using fundamental principles of complexation reactions. Through this method of assembly formation, it could be shown that the assembled nanoclusters exhibited superior optical properties vis-à-vis the constituent NCs. Also, it could be demonstrated that zinc assisted assemblies of NCs were conferred with superior application potential that could not be attined with the constituent NCs. For, example, zinc coordinated assemblies of NCs could be used as a chiral selector and separator for amino acids which could not be achieved with the non-assembled NCs. Further zinc mediated assemblies of Au NCs were found to exhibit superior anti-cancer activity vis-à-vis ligand mediated assemblies of Au NCs. Further, reversible storage and sensing via modulation of photoluminescence intermittency could be possible with zinc mediated assemblies of Au NCs which could not be achieved with non-assembled Au NCs. Also, reversible storage and sensing of hydrogen could be possible with zinc coordinated assemblies of Au NCs. Thus the present thesis provides a new paradigm in the field of "assembly of nanoscale particles" through the virtuosity of principles of inorganic chemistry.

7.2 Future Prospects

The present thesis work is envisioned to open up newer avenues in the field of "assembly of nanoscale particles" with superior application potential. For example, it has been shown in the current thesis that the luminescence life time of Au NCs get significantly enhanced following complexation reaction with zinc ions. Thus, it may be possible that choice of

proper ligands and further tuning of the reaction conditions may lead to ultra-long phosphorescence (with luminescence lifetime in hours) from the crystalline assemblies of the NCs. Also, doping of the crystalline assemblies for further enrichment of the properties of these crystalline assemblies portends to form an attractive direction forward in this field. Moreover, using these crystalline assemblies for catalysis under high pressure may be achievable in near future.

References:

1. R. Jin, C. Zeng, M. Zhou and Y. Chen, *Chem. Rev.*, 2016, **116**, 10346-10413.
2. G. Li and R. Jin, *Acc. Chem. Res.* 2013, **46**, 1749-1758.
3. H. Xu and K. S. Suslick, *ACS Nano*, 2010, **4**, 3209-3214.
4. L. Shang, S. Dong, G. U. Nienhaus, *Nano Today* 2011, **6**, 401– 418.
5. O. Varnavski, G. Ramakrishna, J. Kim, D. Lee and T. Goodson, *J. Am. Chem. Soc*, 2010, **132**, 16-17.
6. Z. Wu and R. Jin, *Nano Lett.*, 2010, **10**, 2568-2573.
7. C.-A. J. Lin, T.-Y. Yang, C.-H. Lee, S. H. Huang, R. A. Sperling, M. Zanella, J. K. Li, J.-L. Shen, H.-H. Wang, H.-I. Yeh, W. J. Parak and W. H. Chang, *ACS Nano*, 2009, **3**, 395-401.
8. L. Polavarapu, M. Manna and Q.-H. Xu, *Nanoscale*, 2011, **3**, 429-434.
9. F. Wen, Y. Dong, L. Feng, S. Wang, S. Zhang and X. Zhang, *Anal. Chem.*, 2011, **83**, 1193-1196.
10. T. D. Fernández, J. R. Pearson, M. P. Leal, M. J. Torres, M. Blanca, C. Mayorga and X. Le Guével, *Biomaterials*, 2015, **43**, 1-12.
11. K. M. Harkness, B. N. Turner, A. C. Agrawal, Y. Zhang, J. A. McLean and D. E. Cliffel, *Nanoscale*, 2012, **4**, 3843-3851.
12. A. Samanta, B. B. Dhar and R. N. Devi, *J. Phys. Chem. C*, 2012, **116**, 1748-1754
13. Y.-S. Chen and P. V. Kamat, *J. Am. Chem. Soc.*, 2014, **136**, 6075-6082.
14. T. Mitsudome, M. Yamamoto, Z. Maeno, T. Mizugaki, K. Jitsukawa and K. Kaneda, *J. Am. Chem. Soc.*, 2015, **137**, 13452-13455.
15. A. Yahia-Ammar, D. Sierra, F. Mérola, N. Hildebrandt and X. Le Guével, *ACS Nano*, 2016, **10**, 2591-2599.
16. L.-Y. Chen, C.-W. Wang, Z. Yuan and H.-T. Chang, *Analytical Chemistry*, 2015, **87**, 216-229.
17. A. Kim, C. Zeng, M. Zhou and R. Jin, *Part Part Syst Charact.*, 2017, **34**, 1600388.

18. Y.-H. Lin, W.-L. Tseng, *Anal. Chem.* 2010, **82**, 9194– 9200

19. H.Wei, Z. Wang, L. Yang, S. Tian, C. Hou,; Y. Lu, *Analyst* 2010, **135**, 1406– 1410

20. M.-L. Cui, J.-M. Liu, X.-X. Wang, L.-P. Lin, L. Jiao, Z.-Y. Zheng, L.-H. Zhang, S.-L. Jiang, *Sens. Actuators, B: Chem.* 2013, **188**, 53– 58

21. C.-C.Huang, C.-K. Chiang, Z.-H.Lin, K.-H. Lee, H.-T. Chang, *Anal. Chem.* 2008, 80, 1497– 1504.

22. X. Xia, Y. Long, J. Wang, *Anal. Chim. Acta* 2013, **772**, 81– 86.

23. W.-Y. Chen,; L.-Y. Chen,; C.-M. Ou,; C.-C. Huang, S.-C. Wei,; H.-T. Chang, *Anal. Chem.* 2013, **85**, 8834– 8840

24. C.-L. Liu, H.-T. Wu, Y.-H. Hsiao, C.-W. Lai, C.-W. Shih, Y.-K. Peng, K.-C. Tang, H.-W. Chang, Y.-C. Chien, J.-K. Hsiao, J.-T. Cheng, P.-T. Chou, *Angew. Chem., Int. Ed.* 2011, **50**, 7056– 7060.

25. X. Le Guével, N. Daum, M. Schneider, *Nanotechnology* 2011, **22**, 275103

26. Y. Chen, G. Li, H. Qian and R. Jin, in *Catalysis by Materials with Well-Defined Structures*, eds. Z. Wu and S. H. Overbury, Elsevier, Amsterdam, 2015, DOI: https://doi.org/10.1016/B978-0-12-801217-8.00008-6, pp. 239-262.

27. Y. Zhu, H. Qian, M. Zhu, R. Jin, *Adv. Mater.* 2010, **22**, 1915

28. G. Li, H. Qian, R. Jin, *Nanoscale* 2012, **4,** 6714.

29. Y. Zhu, H. Qian, B.A. Drake, R. Jin, *Angew. Chem. Int. Ed.* 2010, **49**, 1295.

30. H. Yamamoto, H. Yano, H. Kouchi, Y. Obora, R. Arakawa, H. Kawasaki, *Nanoscale* 2012, **4**, 4148.

31. G . Li, C. Zeng, R. Jin, *J. Am. Chem. Soc.* 2014, **136**, 3673.

32. G . Li, C. Liu, Y. Lei, R. Jin, *Chem. Commun.* 2012, **48**, 12005.

33. U. N. Pan, R. Khandelia, P. Sanpui, S. Das, A. Paul and A. Chattopadhyay, *ACS Appl Mater & Interfaces*, 2017, **9**, 19495-19501.

34. A. K. Sahoo, S. Banerjee, S. S. Ghosh and A. Chattopadhyay, *ACS Appl Mater & Interfaces*, 2014, **6**, 712-724.

35. R. Khandelia, S. Bhandari, N. Pan Uday, S. Ghosh Siddhartha and A. Chattopadhyay, *Small*, 2015, **11**, 4075-4081.

36. R. Ghosh, U. Goswami, S. S. Ghosh, A. Paul and A. Chattopadhyay, *ACS Applied Materials & Interfaces*, 2015, **7**, 209-222.
37. J. Zhang, C. Cai, S. Razzaque, I. Hussain, Q.-W. Lu and B. Tan, *J Mater. Chem. B*, 2017, **5**, 5608-5615.
38. Y.-e. Shi, S. Luo, X. Ji, F. Liu, X. Chen, Y. Huang, L. Dong and L. Wang, *Dalton Trans.*, 2017, **46**, 14251-14255.
39. Y. Wang, T. Chen, Q. Zhuang and Y. Ni, *ACS Appl. Mater. & Interfaces*, 2017, **9**, 32135-32141.
40. X.-K. Wan, J.-Q. Wang, Z.-A. Nan and Q.-M. Wang, *Sci. Adv*, 2017, **3**.
41. S. K. Sailapu, A.K. Sahoo, S. S. Ghosh and A. Chattopadhyay, *Small*, 2014, **10**, 4067-4071.
42. S. Govindaraju, S. R. Ankireddy, B. Viswanath, J. Kim and K. Yun, *Scientific Reports*, 2017, **7**, 40298.
43. C. Zeng, C, H. Qian, T. Li, G. Li, N. L. Rosi, B. Yoon, R. N. Barnett, R. L. Whetten, U. Landman and R. Jin , *Angew. Chem., Int. Ed.* 2012, **51**, 13114– 13118
44. C. Liu, T. Li, G. Li, K. Nobusada, C. Zeng, G. Pang, L. Rosi Nathaniel and R. Jin, *Angew. Chem., Int. Ed.* 2015, **54**, 9826-9829.
45. B. K. Teo, X. Shi and H. Zhang, *J Am Chem Soc*, 1992, **114**, 2743-2745.
46. W. S. Compel, O. A. Wong, X. Chen, C. Yi, R. Geiss, H. Häkkinen, K. L. Knappenberger and C. J. Ackerson, *ACS Nano*, 2015, **9**, 11690-11698.
47. X. Su and J. Liu, *ACS Appl Mater & Interfaces*, 2017, **9**, 3902-3910.
48. Z. Wu, J. Liu, Y. Li, Z. Cheng, T. Li, H. Zhang, Z. Lu and B. Yang, *ACS Nano*, 2015, **9**, 6315-6323.
49. A. Chakraborty, C. Fernandez Ann, A. Som, B. Mondal, G. Natarajan, G. Paramasivam, T. Lahtinen, H. Häkkinen, Nonappa and T. Pradeep, *Angew. Chem., Int. Ed.*, 2018, **57**, 6522-6526.
50. J. Shen, Z. Wang, D. Sun, G. Liu, S. Yuan, M. Kurmoo and X. Xin, *Nanoscale*, 2017, **9**, 19191-19200.
51. S. Adhikari, , R. Joshi, and C. Gopinathan, *Biochimica et Biophysica Acta*. 1998, **1380**, 109–114.

52. R. Stocker and B. N. Ames, *Proc Natl Acad Sci.* 1987, **84**, 8130–8134.

53. A. Knudsen, Early Hum Dev. 1990, **22**, 23–28.

54. A. Knudsen, F. Ebbesen, H. Hansen and R. Brodersen, *Acta Paediatrica Japonica.* 1993, **35**, 418–422.

55. A. Knudsen and R. Brodersen, 1989, **64**, 605–609.

56. M. Y. Berezin and S. Achilefu, *Chem. Rev.*, 2010, **110**, 2641–2684.

57. Q. Yao, Z. Luo, X. Yuan, Y. Yu, C. Zhang, J. Xie and J. Y. Lee, *Sci. Rep.*, 2014, **4**, 3848.

58. M. D. Hanwell, D. E. Curtis, D. C. Lonie, T. Vandermeersch, E. Zurek and G. R. Hutchison, *J. Cheminf.*, 2012, **4**, 17.

59. A. Zanchet, A. Dorta-Urra, O. Roncero, F. Flores, C. Tablero, M. Paniagua and A. Aguado, *Phys. Chem. Chem. Phys.*, 2009, **11**, 10122–10131.

60. Y. Gao, X.Dai, S.-g. Kang,C.A.J&menez-Cruz, M. Xin, Y. Meng, J. Han, Z.Wang, R. Zhou, *Sci. Rep.* 2014, **4,** 5862.

61. S. Roy, S.Bhandari, A. Chattopadhyay, *J. Phys. Chem. C* 2015, **119**, 21191 –21197.

62. Z. Quan, Y. Wang and J. Fang, *Acc. Chem. Res.*, 2013, **46**, 191–202.

63. A. Lechtken, C. Neiss, M. M. Kappesab and D. Schooss, *Phys. Chem. Chem. Phys.*, 2009, **11**, 4344–4350.

64. A. Mallick, P. More, S. Ghosh, R. Chippalkatti, B. A. Chopade, M. Lahiri and S. Basu, *ACS Appl. Mater. Interfaces*, 2015, **7**, 7584–7598.

65. J. Sun, J. Zhanga and Y. Jin, *J. Mater. Chem. C*, 2013, **1**, 138–143.

66. A. Holmgren and J. Lu, Biochem. *Biophys. Res. Commun.*, 2010, **396**, 120-124.

67. B. D. Chithrani and W. C. W. Chan, *Nano Lett.*, 2007, **7**, 1542-1550.

68. H. Gao, W. Shi and L. B. Freund, *Proc Natl Acad Sci U S A*, 2005, **102**, 9469.

69. 8. G. Bao and X. R. Bao, *Proc Natl Acad Sci U S A*, 2005, **102**, 9997.

70. . Rubbiani, I. Kitanovic, H. Alborzinia, S. Can, A. Kitanovic, L. A. Onambele, M. Stefanopoulou, Y. Geldmacher, W. S. Sheldrick, G. Wolber and A. Prokop, *J. Med. Chem.*, 2010, **53**, 8608–8618.

71. G. Ferraro, C. Gabbiani and A. Merlino, *Bioconjugate Chem.*, 2016, **27**, 1584–1587.

72. Z. Luo, X. Yuan, Y. Yu, Q. Zhang, D. Leong, J. Y. Lee and J. Xie, *J. Am. Chem. Soc.*, 2012, **134**, 16662–16670.

73. D. Cassano, S. Pocovı´-Martı´nez and V. Voliani, *Bioconjugate Chem.*, 2018, **29**, 4–16.

74. S. Basu, A. Paul, A. Chattopadhyay, *J. Mater. Chem. A*, 2016, **4**, 1218-1223.

75. S. Basu, A. Paul, A. Chattopadhyay, *Chem Eur J.*, 2017, **23**, 9137-9143.

76. Y. Fu, J. Zhang, J. R. Lakowicz, *Langmuir* 2008, **24**, 3429-3433.

77. B. Li, G. Zhang, Z. Wang, Z. Li, R. Chen, C. Qin, Y. Gao, L. Xiao, S. Jia, Sci Rep.2016, 6, 32662.

78. Y. Kitahama, A. Enogaki, Y. Tanaka, T. Itoh, Y. Ozaki, J. Phys. Chem. C 2013, 117, 9397-9403.

79. M. Kuno, D. P. Fromm, H. F. Hamann, A. Gallagher, D.J. Nesbitt, J. J. Chem. Phys. 2001, 115, 1028.

80. k. T. Shimizu, R.G. Neuhauser, C.A. Leatherdale, S. A. Empedocles, W. K. Woo, M.G. Bawendi, Phys. Rev. B 2001, 63, 205316.

81. E. K. L. Yeow, S. M. Melnikov, T. D. M. Bell, F. C. De Schryver, J. Hofkens, *J. Phys. Chem. A* 2006, **110**, 1726-1734.

List of Publications in Peer reviewed Journals

1. **Basu, S.;** Paul, A.; Chattopadhyay, A. Zinc Mediated Crystalline Assembly of Gold Nanoclusters for Expedient Hydrogen Storage and Sensing. *J. Mater. Chem. A* 2016, **4**, 1218-1223.
2. **Basu, S.**; Sahoo, A. K, Paul, A.; Chattopadhyay, A. Thumb Imprint Based Detection of Hyperbilirubinemia Using Luminescent Gold Nanoclusters. *Sci Rep*, 6, 2016, doi:10.1038/srep39005.
3. **Basu, S.;** Paul, A.; Chattopadhyay, A. Zinc Coordinated Hierarchical Organization of Gold Nanoclusters for Chiral Recognition Supplemented with Separation. *Chem. Eur. J.* 2017, DOI: 10.1002/chem.201701128.
4. Goswami, U.; **Basu, S.**; Paul, A.; Ghosh, S S, Chattopadhyay, A. White Light Emission from Bacteria Embedded with Gold Nanoclusters. *J. Mater. Chem. C*, 2017,**5**, 12360-12364.
5. **Basu, S**.; Goswami, U.; Paul, A.; Chattopadhyay, A. Crystalline assembly of gold nanoclusters for mitochondria targeted cancer theranostics. *J. Mater. Chem. B*, 2018, **6**, 1650-1657
6. **Basu, S**.; Bhandari, S.; Pan, Uday Narayan. Paul, A.; Chattopadhyay, A. Crystalline nanoscale assembly of gold clusters for carbon dioxide storage and sensing via modulation of single particle intermittency, *J. Mater. Chem. C*, 2018, DOI.10.1039/C8TC02225A
7. Gayen, C.; **Basu, S**.; Paul, A. Single particle level chromaticity index based discrimination of biothiols using a dual emitting nanoprobe (communicated).
8. Roy, S.; Bhandari, S.; Pramanik, S.; Pan, Uday.; **Basu, S**; Gogoi, K.; Chattopadhyay, A. Duality in Photoluminescence Intermittency of a Single Quantum Dot Complex. (Manuscript under preparation).

List of Patents

1. Arun Chattopadhyay, Anumita Paul, Srestha Basu, Amaresh Kumar Sahoo, A device for visual detection of bilirubin. International patent no. WO2016193996A1. 2016
2. Arun Chattopadhyay, Anumita Paul, Srestha Basu, Amaresh Kumar Sahoo, A device for visual detection of bilirubin. Indian patent Application no. 631/KOL/2015A. 2015

PERMISSIONS

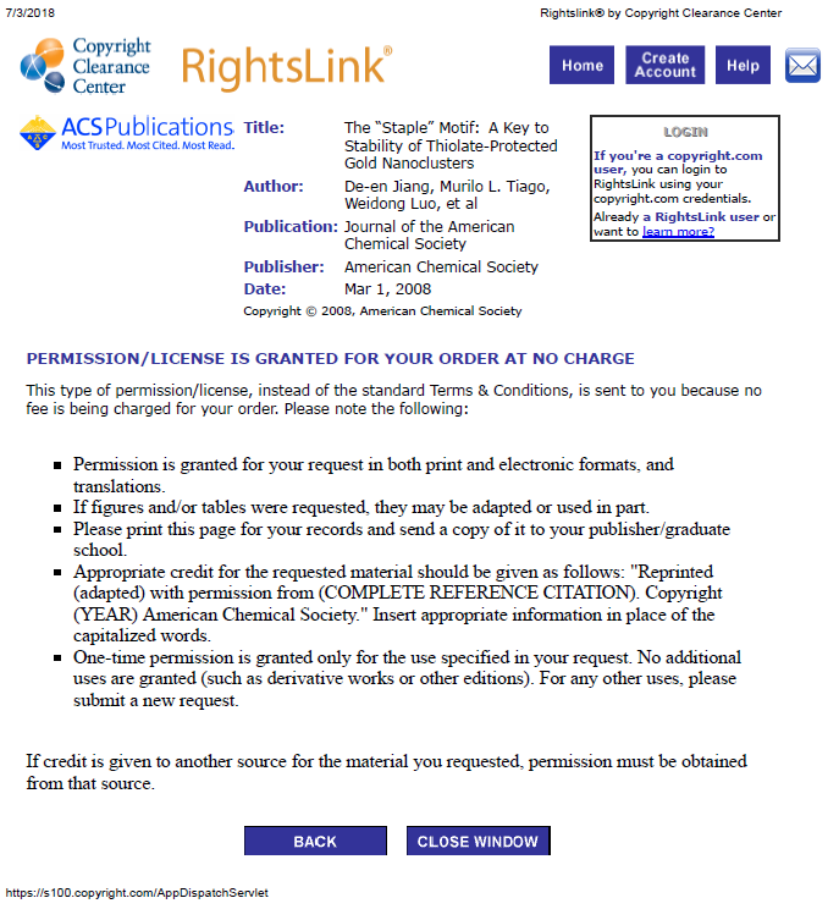

7/3/2018 Rightslink® by Copyright Clearance Center

Copyright Clearance Center RightsLink®

Home | Create Account | Help

ACS Publications Most Trusted. Most Cited. Most Read.

Title: The "Staple" Motif: A Key to Stability of Thiolate-Protected Gold Nanoclusters

Author: De-en Jiang, Murilo L. Tiago, Weidong Luo, et al

Publication: Journal of the American Chemical Society

Publisher: American Chemical Society

Date: Mar 1, 2008

Copyright © 2008, American Chemical Society

LOGIN

If you're a copyright.com user, you can login to RightsLink using your copyright.com credentials.

Already a RightsLink user or want to learn more?

PERMISSION/LICENSE IS GRANTED FOR YOUR ORDER AT NO CHARGE

This type of permission/license, instead of the standard Terms & Conditions, is sent to you because no fee is being charged for your order. Please note the following:

- Permission is granted for your request in both print and electronic formats, and translations.
- If figures and/or tables were requested, they may be adapted or used in part.
- Please print this page for your records and send a copy of it to your publisher/graduate school.
- Appropriate credit for the requested material should be given as follows: "Reprinted (adapted) with permission from (COMPLETE REFERENCE CITATION). Copyright (YEAR) American Chemical Society." Insert appropriate information in place of the capitalized words.
- One-time permission is granted only for the use specified in your request. No additional uses are granted (such as derivative works or other editions). For any other uses, please submit a new request.

If credit is given to another source for the material you requested, permission must be obtained from that source.

BACK | CLOSE WINDOW

https://s100.copyright.com/AppDispatchServlet

Title: Protein-Based Multifunctional Nanocarriers for Imaging, Photothermal Therapy, and Anticancer Drug Delivery

Author: Uday Narayan Pan, Rumi Khandelia, Pallab Sanpui, et al

Publication: Applied Materials

Publisher: American Chemical Society

Date: Jun 1, 2017

PERMISSION/LICENSE IS GRANTED FOR YOUR ORDER AT NO CHARGE

This type of permission/license, instead of the standard Terms & Conditions, is sent to you because no fee is being charged for your order. Please note the following:

- Permission is granted for your request in both print and electronic formats, and translations.
- If figures and/or tables were requested, they may be adapted or used in part.
- Please print this page for your records and send a copy of it to your publisher/graduate school.
- Appropriate credit for the requested material should be given as follows: "Reprinted (adapted) with permission from (COMPLETE REFERENCE CITATION). Copyright (YEAR) American Chemical Society." Insert appropriate information in place of the capitalized words.
- One-time permission is granted only for the use specified in your request. No additional uses are granted (such as derivative works or other editions). For any other uses, please submit a new request.

If credit is given to another source for the material you requested, permission must be obtained from that source.

BACK CLOSE WINDOW

JOHN WILEY AND SONS LICENSE TERMS AND CONDITIONS

Jul 03, 2018

This Agreement between IIT Guwahati -- Srestha BAsu ("You") and John Wiley and Sons ("John Wiley and Sons") consists of your license details and the terms and conditions provided by John Wiley and Sons and Copyright Clearance Center.

License Number	4381471009280
License date	Jul 03, 2018
Licensed Content Publisher	John Wiley and Sons
Licensed Content Publication	Angewandte Chemie International Edition
Licensed Content Title	Observation of Body-Centered Cubic Gold Nanocluster
Licensed Content Author	Chao Liu,Tao Li,Gao Li,Katsuyuki Nobusada,Chenjie Zeng,Guangsheng Pang,Nathaniel L. Rosi,Rongchao Jin
Licensed Content Date	Jul 1, 2015
Licensed Content Pages	4
Type of use	Dissertation/Thesis
Requestor type	University/Academic
Format	Print and electronic
Portion	Figure/table
Number of figures/tables	1
Original Wiley figure/table number(s)	Figure 2
Will you be translating?	No
Title of your thesis / dissertation	Crystalline assembly of gold nanoclusters mediated by complexation reaction
Expected completion date	Jan 2019
Expected size (number of pages)	150
Requestor Location	IIT Guwahati Subansiri Hostel IIT Guwahati

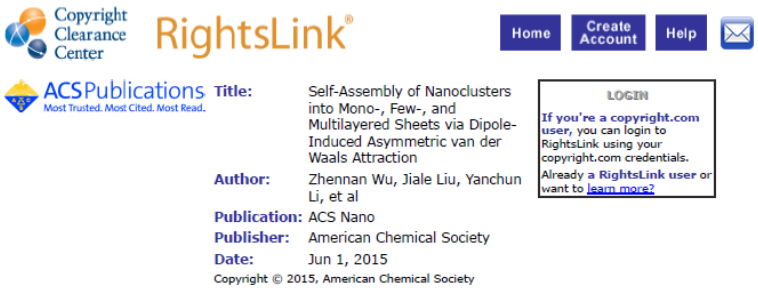

PERMISSION/LICENSE IS GRANTED FOR YOUR ORDER AT NO CHARGE

This type of permission/license, instead of the standard Terms & Conditions, is sent to you because no fee is being charged for your order. Please note the following:

- Permission is granted for your request in both print and electronic formats, and translations.
- If figures and/or tables were requested, they may be adapted or used in part.
- Please print this page for your records and send a copy of it to your publisher/graduate school.
- Appropriate credit for the requested material should be given as follows: "Reprinted (adapted) with permission from (COMPLETE REFERENCE CITATION). Copyright (YEAR) American Chemical Society." Insert appropriate information in place of the capitalized words.
- One-time permission is granted only for the use specified in your request. No additional uses are granted (such as derivative works or other editions). For any other uses, please submit a new request.

If credit is given to another source for the material you requested, permission must be obtained from that source.

BACK CLOSE WINDOW

JOHN WILEY AND SONS LICENSE TERMS AND CONDITIONS

Jul 04, 2018

This Agreement between IIT Guwahati -- Srestha BAsu ("You") and John Wiley and Sons ("John Wiley and Sons") consists of your license details and the terms and conditions provided by John Wiley and Sons and Copyright Clearance Center.

License Number	4382031471071
License date	Jul 04, 2018
Licensed Content Publisher	John Wiley and Sons
Licensed Content Publication	Chemistry - A European Journal
Licensed Content Title	Zinc-Coordinated Hierarchical Organization of Ligand-Stabilized Gold Nanoclusters for Chiral Recognition and Separation
Licensed Content Author	Srestha Basu, Anumita Paul, Arun Chattopadhyay
Licensed Content Date	Jun 20, 2017
Licensed Content Volume	23
Licensed Content Issue	38
Licensed Content Pages	7
Type of use	Dissertation/Thesis
Requestor type	Author of this Wiley article
Format	Print and electronic
Portion	Full article
Will you be translating?	No
Title of your thesis / dissertation	Crystalline assembly of gold nanoclusters mediated by complexation reaction
Expected completion date	Jan 2019
Expected size (number of pages)	150
Requestor Location	IIT Guwahati Subansiri Hostel IIT Guwahati Guwahati, Assam 781039 India Attn: IIT Guwahati
Publisher Tax ID	EU826007151
Total	0.00 USD
Terms and Conditions	

TERMS AND CONDITIONS

This copyrighted material is owned by or exclusively licensed to John Wiley & Sons, Inc. or one of its group companies (each a"Wiley Company") or handled on behalf of a society with which a Wiley Company has exclusive publishing rights in relation to a particular work (collectively "WILEY"). By clicking "accept" in connection with completing this licensing transaction, you agree that the following terms and conditions apply to this transaction (along with the billing and payment terms and conditions established by the Copyright Clearance Center Inc., ("CCC's Billing and Payment terms and conditions"), at the time that you opened your RightsLink account (these are available at any time at